EQUILIBRATION AND STABILITY IN POROUS AND DENSE SOLID OXIDE FUEL CELL MATERIALS: SAMARIUM-DOPED CERIA AND STRONTIUM IRON MOLYBDENUM OXIDE

by

James Wright

A dissertation submitted to the faculty of
The University of Utah
in partial fulfillment of the requirements for the degree of

Doctor of Philosophy

Department of Materials Science and Engineering

The University of Utah

December 2013

The University of Utah Graduate School

STATEMENT OF DISSERTATION APPROVAL

The dissertation of **James Wright**

has been approved by the following supervisory committee members:

Anil V. Virkar	, Chair	**11/04/2013**
		Date Approved
Dinesh K. Shetty	, Member	**10/30/2013**
		Date Approved
Ashutosh Tiwari	, Member	**10/28/2013**
		Date Approved
Feng Liu	, Member	**10/29/2013**
		Date Approved
Michael Free	, Member	**10/28/2013**
		Date Approved

and by **Feng Liu** , Chair of

the Department of **Materials Science and Engineering**

and by David B. Kieda, Dean of The Graduate School.

ABSTRACT

Solid oxide fuel cells (SOFCs) are electrochemical generators: they convert chemical energy into electrical energy using solid-state components. The electrolyte must simultaneously allow the passage of oxygen ions from cathode to anode, while preventing the passage of electrons from anode to cathode.

Porous samples of Sm_2O_3-doped CeO_2 (samaria-doped ceria, SDC) of composition $Sm_{0.15}Ce_{0.85}O_{2-\delta}$ were made. Electrical conductivity was measured using a 4-probe DC method over a wide range of temperatures and oxygen partial pressures. Conductivity rapidly stabilized at any given temperature consistent with the attainment of thermodynamic equilibrium corresponding to the imposed conditions. The ionic transference number of SDC at 400 ^oC in hydrogen was only ~ 0.4, which showed that the electrolytic domain of SDC at and above 400 ^oC was rather narrow. This also suggested that SDC is not a suitable electrolyte without a thin electron blocking layer.

$Sr_2Fe_{1.5}Mo_{0.5}O_{6-\delta}$ (SFMO) powders were synthesized by combustion synthesis. Porous samples were formed and electrical conductivity was measured by a four-point DC technique over a temperature range from 200 ^oC to 800 ^oC in air and in hydrogen. It was observed that $Sr_2Fe_{1.5}Mo_{0.5}O_{6-\delta}$ is stable at 800 ^oC in water-containing atmospheres. However, it reacts with water at low temperatures. Reaction of $Sr_2Fe_{1.5}Mo_{0.5}O_{6-\delta}$ with water at low temperatures is a potential shortcoming of this material.

The previous work demonstrated instability in water-containing atmospheres due to decomposition of SFMO into strontium hydroxides and di-hydroxides. In this work, we demonstrated that SFMO was also unstable in dry atmospheres, such as ultra-high-purity (UHP) hydrogen, and that different decay products result whether the imposed atmospheres are oxidizing or reducing.

Powders with particles that are nanometers in diameter are desirable for creating materials with enhanced electrical, catalytic, and ionic properties. A method based on combustion synthesis for preparing nanocrystalline powder was investigated and samarium-doped ceria (SDC) was synthesized. The resulting products were characterized by XRD, TEM, and BET. The effect of fuel content in the starting mixture on the powder grain size was investigated, and the requirements for nanosized powders were demonstrated. Nanosized SDC powders showed improved performance in a fuel cell compared with conventional SDC powders.

TABLE OF CONTENTS

LIST OF TABLES

LIST OF FIGURES

ACKNOWLEDGEMENTS

I would like to thank Dr. Anil Virkar for his support, patience, and instruction. The work presented in this dissertation could not have occurred without him.

I would also like to thank my thesis advisory committee: Dr. Dinesh Shetty, Dr. Feng Liu, Dr. Ashutosh Tiwari, and Dr. Michael Free. Their time and effort in guiding my research and being a part of my committee is greatly appreciated.

Lei Zhang, another graduate student in the Materials Science and Engineering Department, performed the EIS work in Chapter 4. Dr. F. Zhao did an initial investigation and performed the button cell power evaluation in Chapter 5.

This work was made possible through the financial support from the U.S. Department of Energy under the Grant Number DE-FG02-03ER46086 and DOE EFRC Grant Number DE-SC0001061 as a flow through from the University of South Carolina.

Thanks to all my friends and colleagues in the research lab and at the University of Utah, both past and present, for their support and friendship.

Finally, thanks to my wife Linda, who suffered though many years of efforts and challenges as this work completed. Her dedication and discipline were sorely tried but triumphed. My children Ray and Max are encouraged to surpass my achievements.

CHAPTER 1

INTRODUCTION

Components of solid oxide fuel cells (SOFCs) have multiple functional requirements, and rational and successful design requires knowledge of their electrochemical and mechanical properties. Frequently, investigations of the materials used in SOFCs use methods or approaches that overlook critical aspects of real-world SOFC operation. This dissertation documents four papers written to establish more accurate and reliable measurement of material properties and a material synthesis method for SOFC components. The first deals with the properties of samarium-doped ceria (SDC), an electrolyte material. Two deal with strontium iron molybdenum oxide (SFMO), an electrode material, and its properties. Both materials are investigated in the form of porous bars, to develop the most realistic data possible on such electrochemical properties as four-point DC electrical conductivity (and its subcomponents, ionic and electronic conductivity). Basic justification for the approaches used and the results obtained are given, and the improvements over data from the literature are shown. Finally, a paper on the synthesis of nanosized SDC particles demonstrates a new method to optimize and control the size of combustion-synthesis grown materials.

Solid oxide fuel cells (SOFCs) consist of three working parts: an anode, a cathode, and an electrolyte. The anode layer disassociates hydrogen into electrons and protons. The electrons are available to power an external circuit. The protons remain, waiting for the passage of oxygen ions from the cathode (from supplied air or oxygen atmosphere) through the electrolyte. The cathode dissociates oxygen, by combining it with electrons from the external circuit to create oxygen ions, which pass through the electrolyte. Once the oxygen ions reach the anode surface, they combine with the protons to form water. The water leaves, with any unreacted hydrogen, in the exhaust. To

improve overall energy efficiency, the exhaust is available to burn in a gas turbine. A schematic of a typical solid oxygen fuel cell is shown in Figure 1.1 .

Many researchers investigate materials in dense form; that is, when fabricating samples for experiment, they press powders into compacts and sinter them at a temperature sufficient to render them fully dense, or nearly so. This provides samples of reasonable mechanical strength, uniform structure, and regular shape. However, this may not be an optimal approach when investigating electrochemical properties.

The electrochemical properties such as conductivity, solid-state oxygen and hydrogen ionic diffusivity, and dissociation of hydrogen and oxygen molecules on active surfaces are affected by the structure of the materials themselves. Flat, hard, nonporous surfaces have a smaller surface area than highly fissured and porous surfaces of the same dimensions, often by an order of magnitude or more. Many electrochemical processes proceed faster with higher surface area. Still, experiments are done with flat, dense samples for the reasons cited above. In this research, it is seen that using dense samples can lead to significant inaccuracy in measuring electrochemical properties.

1.1 Samarium-doped Ceria

In Chapter 2, a literature search on SDC shows that electronic conduction was observed in SDC at 400^{o} C below 10^{-32} atm of pO_2. This research shows that a more accurate figure would be 10^{-20} atm of pO_2. The primary reason for the difference is that this research was done on porous, equilibrated samples, which give a more accurate response than the dense samples used in previous works.

When investigating electrochemical properties of materials, it is necessary for the

sample to equilibrate. This involves waiting long enough for the sample to reach the desired temperature, and then to reach equilibrium with the imposed atmosphere as well. Equilibrium with the imposed atmosphere also changes with temperature; that is, the sample does not reach equilibration with the imposed atmosphere immediately, and stay there throughout an experiment while the temperature varies. For a given gas-phase chemical reaction, the energy change is expressed by the following equation:

$$\Delta G = -R\ T \ln K \qquad (1.1)$$

where the change in Gibbs free energy is a function of the ideal gas constant, the absolute temperature, and the logarithm of the equilibrium constant, which itself is a function of the partial pressures of the gases involved (such as hydrogen, oxygen, and water, for a simple SOFC).

For the partial oxygen pressure (pO_2) to reach the same value inside the sample as outside, the oxygen ions must travel from the surface to the interior of the individual sample grains or crystallites. This is much slower in dense samples than porous ones, and requires significant time in dense samples.

However, at low temperatures, even if the oxygen ion conductivity of SDC may be quite high, the chemical diffusion coefficient of neutral oxygen, which is proportional to the product of ionic and electronic conductivities, is rather low. This means the equilibration of a fully dense sample of a typical thickness (2mm) with the imposed atmosphere, whose kinetics is dictated by the chemical diffusion coefficient of oxygen, is very sluggish. Suppose for example the chemical diffusion coefficient of oxygen through

SDC is $\tilde{D}_O$ at a given temperature and in a given atmosphere. For a sample of thickness 2d, the time required for sample equilibration with the imposed atmosphere to occur will be $t \alpha d^2/\tilde{D}_O$. For an assumed $\tilde{D}_O$ of 10^{-7} cm^2 s^{-1} at 500 ◦C, the time required for the equilibration of a 2 mm thick sample is 10^5 s; that is 28 h, or over a day. Rarely are experiments conducted for more than a few h of equilibration. This means often equilibration of the sample with the imposed atmosphere may not occur over the duration of the experiment. The lower the temperature, the lower is the $\tilde{D}_O$, and the longer will be the time required for equilibration. If the kinetics are extremely sluggish, stable values of conductivity may be observed. However, stable values in such cases are representative of metastable conditions and do not correspond to the thermodynamically equilibrated state. Thus, reliable measurements corresponding to thermodynamically equilibrated conditions can only be made on dense bulk samples 2 mm thick at sufficiently high temperatures. For SDC, this temperature is probably about 600 ◦C. The objective of the present work was to explore the use of porous samples instead of dense samples for the measurement of transport properties of SDC. If a porous sample is used for conductivity measurements, gas transport through the sample will generally be very rapid. Suppose the open (contiguous) porosity in a porous sample is 30%. Typical effective gas diffusivity of air through a porous sample, estimated using the binary O_2–N_2 diffusivity [1], porosity, and tortuosity is $0.1 cm^2$ s^{-1}. Thus, in a porous sample of 2 mm thickness, gas phase equilibration will occur in $(0.1)^2/0.1$ or in 0.1 s. Suppose now that the particle size in the porous sample is 2 μm. Equilibration of composition in the solid phase of the porous sample corresponding to the imposed gas phase will occur in $(1\times10{-}4)^2/10^{-7}$ or in 0.1 s. That is, the solid phase in a porous sample of 2 mm thickness will equilibrate a

million times faster than a dense sample of the same external dimensions (2 mm). Since the equilibration of a gas phase in porous interstices of porous samples and compositional equilibration within the particles of the porous sample by solid state diffusion are sequential/concurrent steps, the overall time required for thermodynamic equilibration of a porous material with the imposed atmosphere may only be a fraction of the time required for bulk, dense samples. This orders of magnitude difference between the kinetics of equilibration of dense and porous samples is schematically depicted in Figure 1.2(a) and (b). The preceding shows that the equilibration of a porous sample with the atmosphere can occur in areas in a reasonable time, which is often not possible on a dense sample. Properties of fully dense materials may then be estimated using the measured values on porous samples provided appropriate geometric factors, which can relate the conductivity of the porous sample to the corresponding dense sample, are known. Such geometric or correction factors depend upon volume fraction, porosity, and morphology of the solid phase within the porous body such as the particle size and the interparticle neck size [2]. If the interparticle necks in a porous body are relatively wide, a simple correction factor based solely on the volume fraction porosity may be used [2]. Alternatively, if the morphological features such as the particle size and the interparticle neck size are accurately known, and if the interparticle necks are narrow, the conductivity of the porous sample can be related to that of the corresponding dense sample by the use of a geometric parameter derived using these parameters [2].

The estimation of such correction or geometric factors requires a thorough characterization of the microstructure. It is important to have accurate information on the conductivity of dense samples under thermodynamically equilibrated conditions. This is

because dense membranes typically used in many electrochemical devices may eventually equilibrate with the atmosphere in the actual device application over the long duration in service. For example, solid electrolytes several tens of microns thick may equilibrate with the imposed atmosphere over hundreds or thousands of h of operation. If the design of such devices, however, is based on measurements made on bulk dense samples, which only give the initial values under nonequilibrated conditions, the predictions of long-term performance made using such measurements may likely be inaccurate. Measurements made on porous samples, and corrected using appropriate geometric factors to obtain the corresponding properties of dense samples, on the other hand, provide a way to estimate properties of dense materials necessary for use in actual devices such as an electrolyte in SOFC. Additionally, the measurement of conductivity on porous bodies is important in its own right since electrodes are porous and rapidly equilibrate with the imposed atmosphere. Thus, measurements made on porous samples can be directly used for the design of SOFC electrodes.

Using porous electrodes, it was possible to show that the values found previously in the literature are inaccurate, relating to the electrolytic domain of SDC at 400^{o} C. It also made it possible to measure the four-point DC conductivity down to 250^{o} C, a significant improvement in low-temperature results for this property, and the method is readily applicable to other materials as well.

1.2 Electrical Characterization and Water Sensitivity of SFMO

In Chapter 3, the same methodology was applied to the electrode compound strontium iron molybdenum oxide (SFMO), but with quite different results. The literature advised that SFMO would make a useful electrode compound, both as anode and cathode, at temperatures up to 800 ^{o}C. This is because the experimenters used the dense sample configuration, and during the time of their experiments, the SFMO did not reach equilibrium with the imposed atmosphere. This led to results which were not representative of the true behavior of SFMO under these conditions, especially in longer time frames.

The measured DC 4-probe conductivity of an SFMO sample as a function of temperature decreased on an Arrhenius plot over a temperature range between 200 ^{o}C and 800 ^{o}C. The red and black squares correspond respectively to measurements made during the first and the second run, both in 100% H_2 atmosphere, during cooling from 800 ^{o}C to 200 ^{o}C in 100 degree steps. It was observed that during the second run, the measured conductivity was considerably lower than during the first run, especially at lower temperatures. Triangles and crosses in Figure 1.3 respectively correspond to measurements made during the first and the second run in air. Greater deviation is observed at higher temperatures, although the trends are not so clear in these sets of measurements. The decrease in conductivity is attributable to structural changes in the sample due to decay into other compounds during the test period.

Figure 1.4 shows the measured conductivity as a function of time for the measurements made in hydrogen. Also plotted in the figure is the temperature vs. time trace for the two runs as the temperature was varied between 800 ^{o}C and 200 ^{o}C. Note

that stable conductivity values were recorded during the first run from 800 °C to 200 °C at each temperature. However, when the sample was reheated to 800 °C during the second run, a stable conductivity value was not achieved over the period the sample was maintained at 800 °C (about 8 h). The conductivity increased over the duration of this step. This observation suggests that some instability (reaction) occurred at low temperatures, and some changes in the material continued to occur when the sample was heated to 800 °C.

Stable values of conductivity were not observed during the second run, as seen in Figure 1.4. The corresponding data for the two runs are shown as squares in Figure 1.3. At the end of conductivity measurements, an XRD trace of the sample was obtained. The two XRD traces of the sample, before and after testing, are compared in Figure 1.5. The same XRD peaks are present in both spectra, although some peak broadening seems to have occurred in the sample after testing. The absence of detectable amounts of reaction products in the XRD trace after conductivity tests is attributed to relatively sluggish reaction kinetics when H_2O is present in a vapor form, such as at 200 °C. Under such conditions, any water soluble reaction product (e.g., Sr $(OH)_2$) cannot be removed, thus slowing down kinetics.

Similar conductivity measurements on porous SDC showed very stable and reproducible values during heating and cooling, consistent with the fact the SDC is stable over the range of temperatures and atmospheres tested [3].

1.3 Instability and Degradation of SFMO in Oxidizing and Reducing Atmospheres

It was seen in the previous pages that SFMO is unstable towards water under low temperatures, and that SFMO would in fact decompose or degrade into other compounds when exposed to liquid water at room temperature. This work was extended in Chapter 4 and the products created when SFMO is decomposed in pure hydrogen or air were characterized. The compound is unstable in air or hydrogen over time at elevated temperatures, leading to total decay and breakdown. It suffers from different routes of attack, depending on whether oxygen or hydrogen is present, and water forms as it decays in hydrogen, providing another attack route.

The various decay products have been investigated by XRD, and depending on whether the decay is partial or total, different product compounds will be found. Early and partial decay in hydrogen leads to strontium and iron hydroxyl compounds (partially due to water attack), while decay in air takes higher temperatures and longer times than performed in this study.

1.4 Combustion Synthesis of Nanosized Samaria-doped Ceria

In Chapter 5, the synthesis of samaria-doped ceria with specific surface areas up to 61 cm^2 / g and particle sizes ranging between 4 and 9 nanometers in diameter was demonstrated by the combustion of metal nitrate salts with DGA fuel in a precursor solution. The as-synthesized powder showed high crystallinity as characterized by XRD. Using the thermodynamic analysis based on adiabatic flame temperature, the effect of the ratio between DGA-to-nitrate content on the powder area and crystallite size was studied.

To obtain powder of desired size and phase content, the fuel content must be carefully controlled. Solid oxide fuel cells using as-synthesized SDC powder in composite electrodes and electrolytes show high performance, in excess of 1.6 W / cm^2 at 800 ^oC.

1.5 The Scope of the Dissertation

This dissertation covers six years of research, which resulted in four papers, two of which were published and two nearly completed by the time of defense. The work can generally be described as depicting the usefulness of porous samples in investigating electrochemical properties of SOFC materials, both electrodes and electrolytes.

In Chapter 1, the work demonstrates that the frequent practice of using dense samples to investigate properties runs the danger of failing to equilibrate completely (or even significantly) during the extent of the experiment. The resulting measurements on dense, unequilibrated samples may not yield accurate data for design and fabrication of solid-state electrochemical devices. Samarium-doped Ceria (SDC) and strontium iron molybdenum oxide (SFMO) are the compounds used in the research.

Chapter 2 describes the initial research on samarium-doped ceria, where the use of porous samples allowed a determination that the electrolytic domain of SDC was narrower at temperatures of 400 ^oC and above than previously believed. The use of dense samples in previous research led to an understanding of SDC properties that was inaccurate, and this work explains some of the impediments to the successful use of SDC as an electrolyte in SOFCs. Without a thin-film electron-blocking layer (such as YSZ), the electronic conductivity of SDC at higher temperatures will allow too large a leakage current, defeating the purpose of an electrolyte and preventing higher current densities

and performance.

Chapter 3 describes an investigation into SFMO, a candidate for electrode use in SOFCs. Again, porous samples allowed a more rapid investigation into the degradation of SFMO under conditions encountered during normal SOFC use, particularly during startup and shutdown, when water vapor or even liquid water can be generated and remain on the surfaces of the electrodes. The presence of liquid water at any time in contact with SFMO was shown to attack the composition of SFMO itself, leading to degradation of performance and eventual failure of the electrode.

In Chapter 4, it is seen that SFMO is also vulnerable to an imposed atmosphere of ultra-high-purity hydrogen, which attacks it by removing oxygen from the sublattice and forming water on the surface. No reasonable solution to this problem is seen; a coating that would isolate the SFMO from hydrogen would defeat its use in an SOFC, while operating an SOFC in a hydrogen partial pressure range so dilute as to prevent its degradation would require massive amounts of very-low-purity hydrogen (10^{-9} to 10^{-13} atm) to power a device, and therefore vast surface areas to adsorb it. The degradation is irreversible; that is, once SFMO is decayed under hydrogen, it will not regenerate under air at temperatures normally seen by an SOFC device (up to 800 ^{o}C).

In Chapter 5, there is an investigation of an optimized process to produce nanosized particles of SDC by combustion synthesis. Controlling the ratio of fuel to nitrate in precursor salts is the critical parameter to creating nanosized particles, and the method can presumably be applied to many materials prepared by this method.

Finally in Chapter 6, there is a summary and conclusions to be drawn from the present work, along with suggestions for further work.

1.6 References

1) E. L. Cussler, Diffusion: Mass Transfer in Fluid Systems, Cambridge University Press, Cambridge, UK, 1995.

2) F. Zhao, A.V. Virkar, J. Power Sources 195 (2010) 6268–6279.

3) J. Wright, A. V. Virkar, J. Power Sources 196 (2011) 6118-6124.

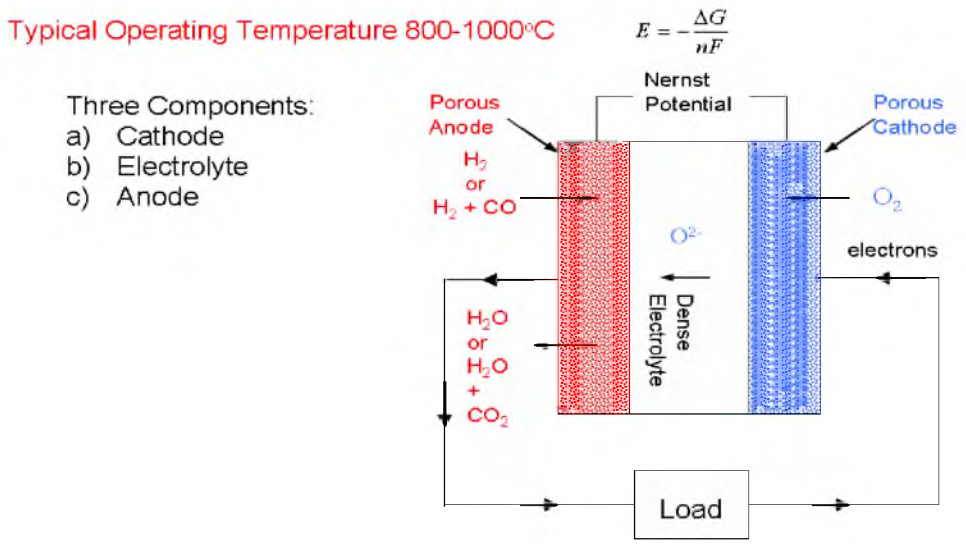

Figure 1.1 Schematic of a solid oxide fuel cell (SOFC)

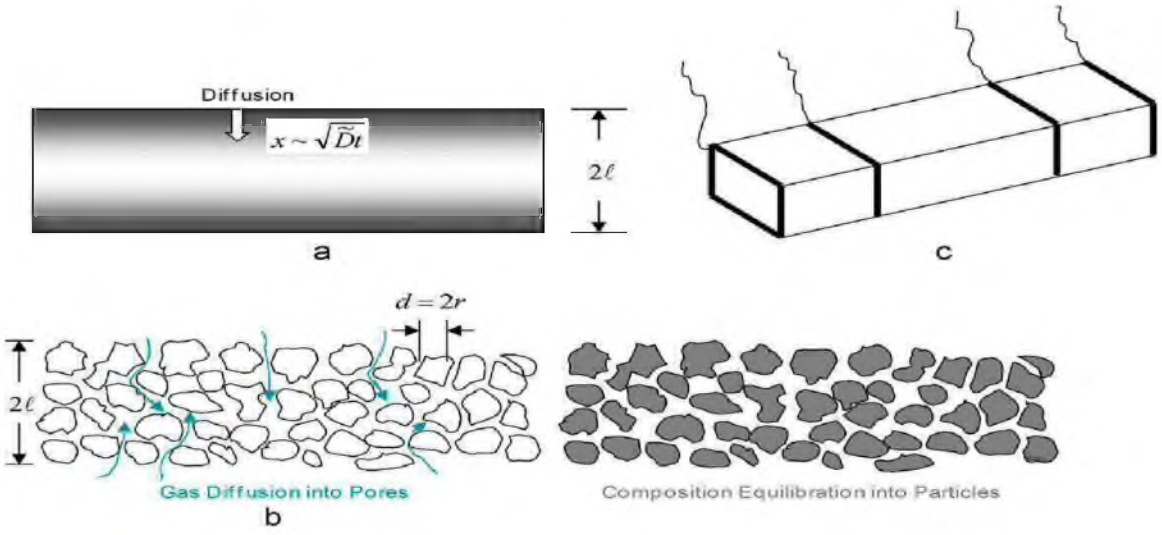

Figure 1.2 Illustration of equilibration inside pores and fissures, and inside particles

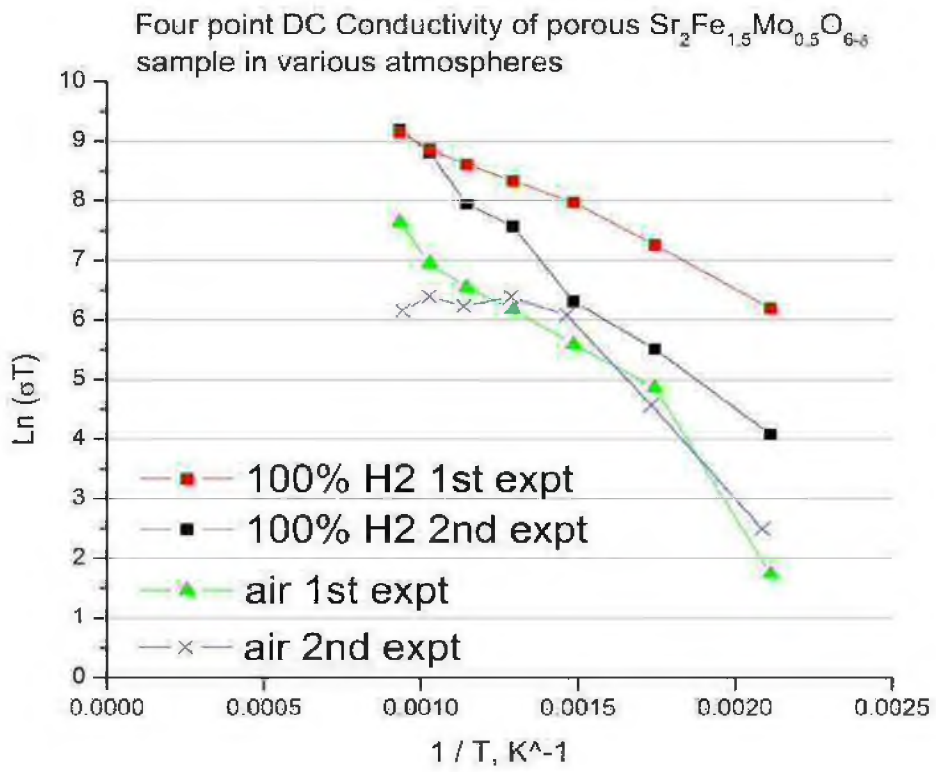

Figure 1.3 Four-point DC conductivity of porous $Sr_2Fe_{1.5}Mo_{0.5}O_{6-\delta}$ sample in various atmospheres

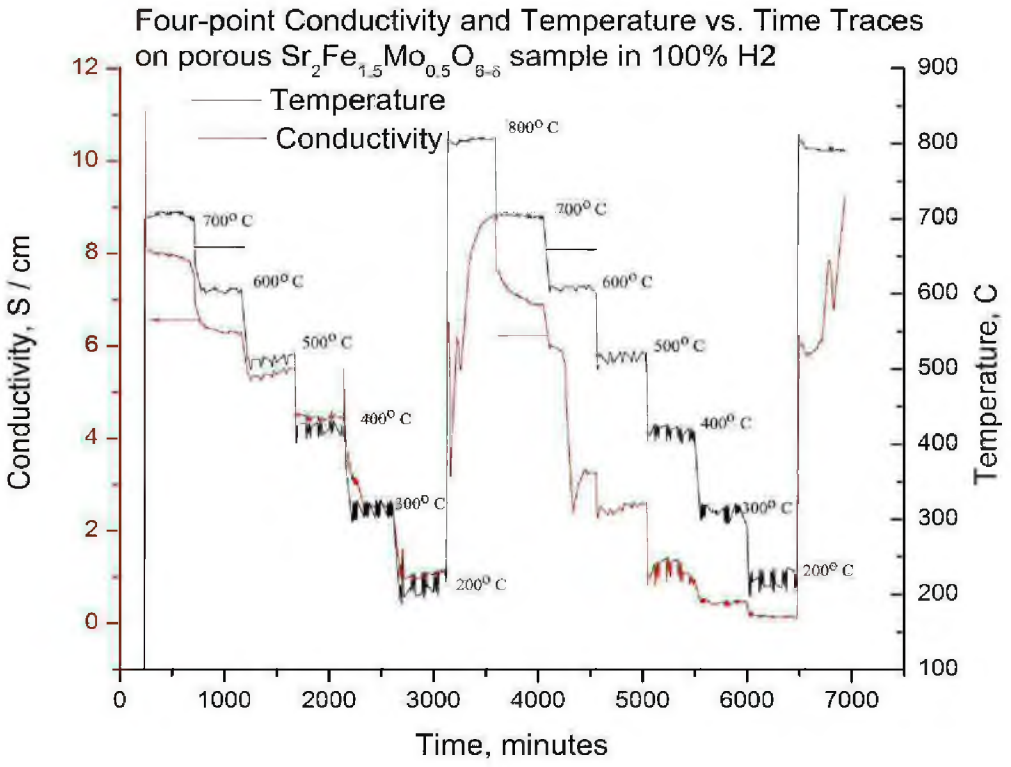

Figure 1.4 Conductivity vs. time for measurements over a range of temperatures between 800 °C and 200 °C during two consecutive experiments. Also plotted in the figure is the corresponding temperature vs. time plot. Note that during the second run, stable values of conductivity were not observed. This is attributed to the reaction of SFMO with moisture at low temperatures.

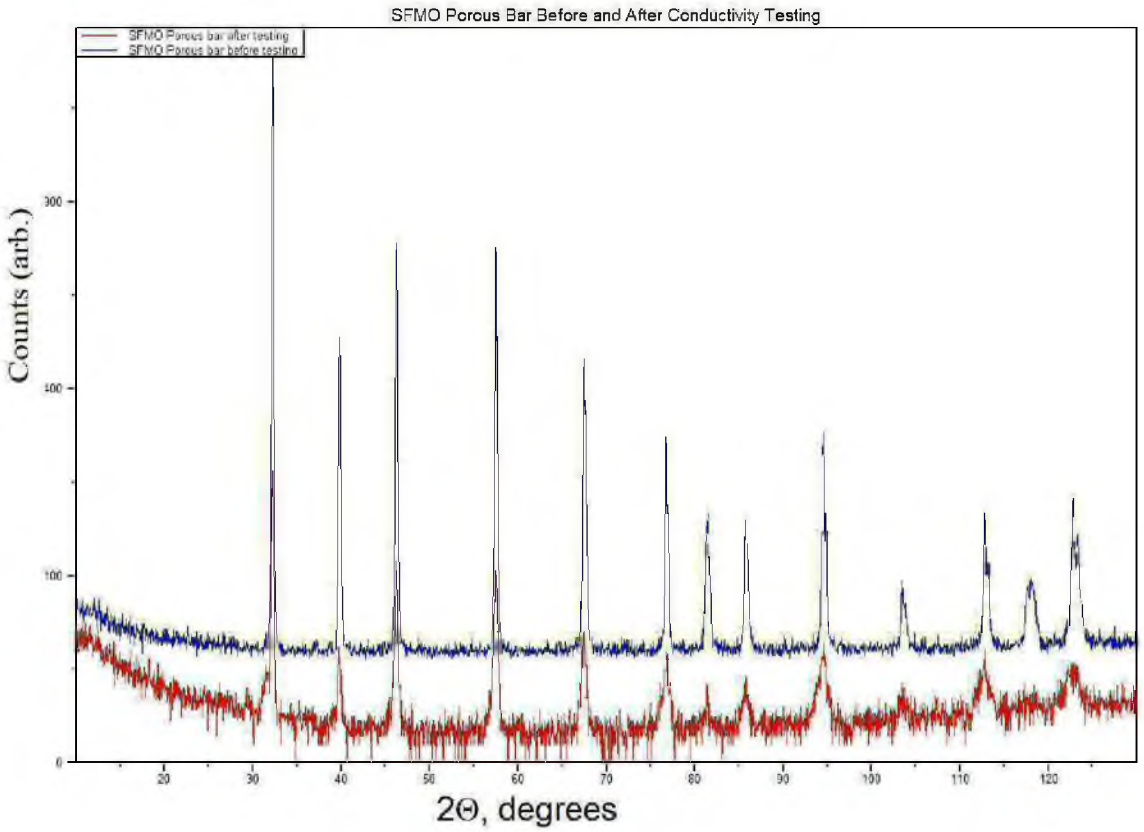

Figure 1.5 XRD traces of the as-fabricated porous SFMO sample after several conductivity measurements. The traces appear to be very similar. Small amounts of reaction products, such as $Sr(OH)_2$, cannot be detected by XRD. However, they do affect the conductivity.

CHAPTER 2

CONDUCTIVITY OF POROUS Sm_2O_3-DOPED CeO_2 AS A FUNCTION OF TEMPERATURE AND OXYGEN PARTIAL PRESSURE

Originally published in Journal of Power Sources 196 (15) (2011) 6118-6124

Reprinted with permission

2.1. Introduction

Much of the current development of solid oxide fuel cells (SOFC) is based on yttria-stabilized zirconia (YSZ) as the electrolyte which exhibits ionic transference number near unity over wide temperature and oxygen partial pressure ranges. Rare earth oxide-doped ceria (RDC) is an excellent oxygen ion conductor. Its ionic conductivity is typically two or three times that of YSZ at a given temperature, and thus is of interest for low to intermediate temperature SOFC (500–700 ◦C) [1–17]. RDC at low oxygen partial pressures and at high temperatures, however, becomes a mixed ionic electronic conductor (MIEC) [1,18–20]. Catalytic and electrocatalytic properties of undoped ceria and RDC have also been extensively investigated. In a porous form, RDC mixed with nickel is a candidate for the anode functional layer of an SOFC. Similarly, RDC mixed with perovskites such as Sr-doped $LaCoO_3$ (LSC), Sr-doped $LaMnO_3$ (LSM), Sr-doped $LaFeO_3$ (LSF), etc. are also known to be candidates for the cathode functional layer. Thus, RDC is a constituent in all three components in low to intermediate temperature SOFCs and it is important to determine its transport properties as a function of temperature and atmosphere. For application as an electrolyte, an ionic number close to one is necessary. For application as a constituent in the electrodes, mixed ionic-electronic conducting properties are beneficial. There is extensive literature on the measurement of transport properties of RDC as a function of temperature and oxygen partial pressure and its potential use as a constituent in SOFC [1,18–22]. Much of the reported work on the measurement of conductivity of RDC is on fully dense samples or on samples sufficiently dense with negligible contiguous porosity [15,17,20–23]. Typical thickness of samples used in such measurements is 2mm. The design of electrolyte and electrodes used in

SOFC is typically based on such measurements made on dense samples. At low temperatures in air, such measurements indicate that RDC is a predominantly oxygen ion conductor with negligible electronic conductivity. However, at low temperatures, even if the oxygen ion conductivity of RDC may be quite high, the chemical diffusion coefficient of neutral oxygen, which is proportional to the product of ionic and electronic conductivities, is rather low. This means the equilibration of a fully dense sample of a typical thickness (2mm) with the imposed atmosphere, whose kinetics is dictated by the chemical diffusion coefficient of oxygen, is very sluggish. Suppose for example the chemical diffusion coefficient of oxygen through RDC is $\tilde{D}_O$ at a given temperature and in a given atmosphere. For a sample of thickness 2d, the time required for sample equilibration with the imposed atmosphere to occur will be t $d^2/\tilde{D}_O$. For an assumed $\tilde{D}_O$ of 10^{-7} cm^2 s^{-1} at 500 ◦C, the time required for the equilibration of a 2 mm thick sample is 10^5 s; that is 28 h, or over a day. Rarely are experiments conducted for more than a few h of equilibration. This means often equilibration of the sample with the imposed atmosphere may not occur over the duration of the experiment. The lower the temperature, the lower is the $\tilde{D}_O$, and the longer will be the time required for equilibration. If the kinetics are extremely sluggish, stable values of conductivity maybe observed. However, stable values in such cases are representative of metastable conditions and do not correspond to the thermodynamically equilibrated state. Thus, reliable measurements corresponding to thermodynamically equilibrated conditions can only be made on dense bulk samples 2 mm thick at sufficiently high temperatures. For RDC, this temperature is probably about 600 ◦C or may be even higher.

The objective of the present work was to explore the use of porous samples

instead of dense samples for the measurement of transport properties of RDC. If a porous sample is used for conductivity measurements, gas transport through the sample will generally be very rapid. Suppose the open (contiguous) porosity in a porous sample is 30%. Typical effective gas diffusivity of air through a porous sample, estimated using the binary O_2–N_2 diffusivity [24], porosity, and tortuosity is $0.1 cm^2\ s^{-1}$. Thus, in a porous sample of 2 mm thickness, gas phase equilibration will occur in $(0.1)^2 / 0.1$ or in 0.1 s. Suppose now that the particle size in the porous sample is 2 μm. Equilibration of composition in the solid phase of the porous sample corresponding to the imposed gas phase will occur in $(1\times10-4)^2 / 10^{-7}$ or in 0.1 s. That is, the solid phase in a porous sample of 2 mm thickness will equilibrate a million times faster than a dense sample of the same external dimensions (2 mm). Since the equilibration of a gas phase in porous interstices of porous samples and compositional equilibration within the particles of the porous sample by solid state diffusion are sequential / concurrent steps, the overall time required for thermodynamic equilibration of a porous material with the imposed atmosphere may only be a fraction of the time required for bulk, dense samples. This orders of magnitude difference between the kinetics of equilibration of dense and porous samples is schematically depicted in Figure 2.1(a) and (b). The preceding shows that the equilibration of a porous sample with the atmosphere can occur in areas in a reasonable time, which is often not possible on a dense sample. Properties of fully dense materials may then be estimated using the measured values on porous samples, provided appropriate geometric factors, which can relate the conductivity of the porous sample to the corresponding dense sample, are known. Such geometric or correction factors depend upon volume fraction porosity and morphology of the solid phase within the porous body

such as the particle size and the interparticle neck size [25]. If the interparticle necks in a porous body are relatively wide, a simple correction factor based solely on the volume fraction porosity may be used [25]. Alternatively, if the morphological features such as the particle size and the interparticle neck size are accurately known, and if the interparticle necks are narrow, the conductivity of the porous sample can be related to that of the corresponding dense sample by the use of a geometric parameter derived using these parameters [25].

The estimation of such correction or geometric factors requires a thorough characterization of the microstructure. It is important to have accurate information on the conductivity of dense samples under thermodynamically equilibrated conditions. This is because dense membranes typically used in many electrochemical devices may eventually equilibrate with the atmosphere in the actual device application over the long duration in service. For example, solid electrolytes several tens of microns thick may equilibrate with the imposed atmosphere over hundreds or thousands of h of operation. If the design of such devices, however, is based on measurements made on bulk dense samples, which only give the initial values under nonequilibrated conditions, the predictions of long-term performance made using such measurements may likely be inaccurate. Measurements made on porous samples, and corrected using appropriate geometric factors to obtain the corresponding properties of dense samples, on the other hand, provide a way to estimate properties of dense materials necessary for use in actual devices such as an electrolyte in SOFC. Additionally, the measurement of conductivity on porous bodies is important in its own right since electrodes are porous and rapidly equilibrate with the imposed atmosphere. Thus, measurements made on porous samples

can be directly used for the design of SOFC electrodes. This was the principal motivation for the present study. The experimental procedure used, the results obtained, and the discussion of results are given in the following paragraphs.

2. 2. Experimental Procedure

Samaria-doped ceria powder of composition $Sm_{0.15}Ce_{0.85}O_{2-\delta}$ (SDC) was obtained from Fuel Cell Materials. The reported surface area of the SDC powder was 40 $m^2\ g^{-1}$. The SDC powder was mixed with carbon powder (HTW, Sigradur K – spherical powder 10–20 μm in diameter) and ethanol with ethylene glycol added as a binder. Zirconia milling media were then added and the mixture was ball milled for 12 h. The milling media were subsequently removed from the jar, the mixture was placed in a beaker, and heated on a hot plate to evaporate away ethanol. The dried powder was then dry milled. Rectangular, bar-shaped samples were formed by uniaxial pressing. Samples were sintered in air at 1400 °C for 2 h. The approximate dimensions of the sintered samples were: 4.5 cm×1 cm×2 mm. The porosity of the samples was measured using a fluid immersion method with water as the fluid. Fracture surfaces of the sintered samples were examined in a scanning electron microscope (SEM). Platinum stripes were painted using platinum paste on the samples in a 4-probe configuration. The distance between the inner stripes was 2 cm, while that between the outer stripes was 4 cm. Platinum wires were connected to the four stripes. Figure 2.1(c) shows a schematic of the samples used for 4-probe DC conductivity measurements. In a typical experiment, a sample with four platinum wires connected was placed inside a tubular furnace equipped with end fixtures and feed-throughs. The wires attached to the outer probes were connected to a Keithley

6517A electrometer (which is also a DC power supply) and the wires attached to the inner probes were connected to a Keithley 2100 multimeter. Data collection was accomplished using a laptop computer and LabView software. Conductivity was measured over a range of oxygen partial pressures achieved using various gas mixtures: (a) ultra-high-purity hydrogen, (b) ultra-high-purity argon, (c) 10% O_2 + 90% N_2, (d) air, and (e) pure O_2. An oxygen sensor (CoorsTek) was used to measure the Nernst voltage of the atmosphere in the furnace referenced to air. The corresponding oxygen partial pressures in the furnace near the sample were estimated. Conductivity measurements were made over a temperature range between 200 ◦C and 800 ◦C in 50 or 100◦ intervals during heating as well as during cooling.

2.3. Results and Discussion

The typical measured porosity of the samples was 45%. Figure 2.2(a) shows an SEM micrograph of a typical sintered sample. Figure 2.2(b) is a higher magnification SEM image of the sample showing the morphological details. The typical particle size within the sample is on the order of 5 μm. Individual particles contained several grains of 1–2 μm in size. The SEM image also shows that interparticle necks are well developed in this sample. If the interparticle necks are sufficiently wide, the relationship between the conductivity of a fully dense sample, σ_{dense}, the conductivity of the porous sample, σ_p, and the volume fraction porosity, V_v, is simply given by

[25] $$\sigma_{dense} \approx \sigma_p / (1 - V_v) \quad (2.1).$$

A more accurate relationship between particle size, neck size, volume fraction porosity, conductivity of particles, and the conductivity of the dense body is given in [25]. If the necks are narrow (poorly sintered materials), it is necessary to use the more accurate equation [25]. In the present work, for the sample whose SEM image is shown in Figure 2.2(b), the simple relation is satisfactory. Thus, the conductivity values of dense samples can be readily estimated from measurements made on most of the porous samples in the present work. In this work, only the conductivity values of porous samples are reported. Figure 2.3 shows the measured conductivity of a porous SDC sample by a 4-probe DC method over the temperature range between 250 and 800 ◦C in humidified hydrogen, plotted vs. time during the experiment. This particular sample did not have well-developed necks. Thus, it is expected that the more accurate correction factor given in [25] will be needed to obtain the corresponding conductivity of a dense sample.

This correction factor is higher than $1/(1 - V_v)$ given in Eq. (2.1) [25]. The profound effect of morphology on conductivity has been discussed in detail in Ref. [25]. The purpose of this experiment is to determine if rapid equilibration can be achieved using a porous sample. In this experiment, the sample was initially heated to 800 ◦C and its conductivity was measured. Measurements thereafter were made at 600 ◦C, 400 ◦C, and 250 ◦C during cool down. For each measurement, the sample was maintained at a given temperature for a sufficient period of time to ensure that stable values of conductivity were recorded. The sample was subsequently heated and measurements were again made during heating to 800 ◦C in 50◦ intervals. These data are also shown in Figure 2.3. Two observations can be made based on this experiment. (a) The conductivity rapidly equilibrated once the sample reached a given temperature. For example, as the

temperature was lowered from 800 ◦C to 600 ◦C, the conductivity decreased from 0.02 Scm^{-1} to 0.004 Scm^{-1}, and then remained constant. The time dependence of the decrease in conductivity coincided with the rate of change of the sample temperature. Once the temperature reached 600 ◦C, no further change in conductivity occurred. This observation indicates that rapid equilibration of the sample conductivity occurred under the imposed atmosphere. The observation that stable values were obtained at the lowest temperature (250 ◦C) at which measurements were made on this sample also indicates that solid state equilibration (by oxygen chemical diffusion) was sufficiently rapid even at such a low temperature due to the small diffusion distance in the sample containing micron size particles. That is, much of the time required for equilibration to occur at a new temperature was the time required for the sample temperature to stabilize to the new value. Approximate time required for equilibration to occur in the sample containing 5 μm size particles at the lowest temperature of 250 ◦C from Figure 2.3 is 10 min. The estimated chemical diffusion coefficient of oxygen thus is $(2.5\times^{10-4})^2/ (10\times60)$ or $\tilde{D}_O \approx 10^{-10}$ cm^2 s^{-1}. No independently measured data on the chemical diffusion coefficient of oxygen in SDC at such a low temperature are available. The present measurements, however, show that even with such low values of the chemical diffusion coefficient, rapid equilibration is expected in porous samples. A dense sample of 2 mm in thickness, on the other hand, would require 3 years to equilibrate. Thus, any stable values observed in short-term experiments (a few h) would be indicative of metastable conditions, and not equilibrated conditions. (b) Measurements at 800 ◦C, 700 ◦C, and 600 ◦C made during both cooling and heating show that identical conductivity values were obtained at any given temperature. This observation also shows that the sample truly equilibrated with

the atmosphere. Thus, the present measurements represent the true values of conductivity of the porous sample under equilibrated conditions. Figure 2.4 shows the estimated oxygen partial pressure in the hydrogen feed gas near the sample in the furnace as a function of temperature obtained from the measured sensor voltage. Depending upon temperature, the oxygen partial pressure measured in pure hydrogen by the oxygen sensor ranged between 10^{-52} and 10^{-25} atm. At any given temperature, the pO_2 was high enough to ensure the thermodynamic stability of YSZ in the sensor. A significant drift in the measured sensor voltage was observed at the lowest measurement temperature of 200 ◦C reflecting drift in the estimated oxygen partial pressure. Thus, the accuracy of the oxygen partial pressure measurement at such a low temperature is probably not good. The horizontal broken lines in Figure 2.4, however, show that at 300 ◦C and above, the estimated oxygen partial pressure at a given temperature is approximately the same during both cooling and heating. Thus, it was assumed that sensor response is accurate above 300 ◦C. The estimated oxygen partial pressures from the sensor voltages should correspond to a certain pH_2/pH_2O ratio. Using the calculated pO_2 from the measured sensor voltages and using the Ellingham diagram [26], the corresponding pH_2 / pH_2O ratios were estimated over the temperature range from 300 ◦C to 800 ◦C. The estimated pH_2 / pH_2O ratio at 300, 600, 700, and 800 ◦C was about 2×10^{3} or pH_2O 5×10^{-4} atm. The estimated value of pH_2O at 400 and 500 ◦C was 5×10^{-3} atm. This variation is believed to be due to some experimental scatter. It is also possible that there may have been leaks in the fixtures allowing some air in, thus raising the H_2O content. It is thus concluded that the pH_2O in the hydrogen gas circulated was approximately in the range 5×10^{-4}–5×10^{-3} atm. Such a low value of pH_2O is consistent with the reasonably dry H_2

used in the experiment. Figure 2.5 shows the plots of log (conductivity) vs. log (oxygen partial pressure) over the temperature range from 200 to 800 ◦C. These data were obtained on another sample. This sample had well-developed interparticle necks. The representative SEM micrograph is given in Figure 2.2. Thus, the correction factor of 1 / (1 − V_v) given in Eq. (2.1) is considered satisfactory. The broken lines show the minimum conductivity values at a given temperature. From Figure 2.5, at 800 ◦C in air, the measured conductivity is 0.024 Scm−1. The volume fraction porosity of this sample was 0.45. Thus, the estimated value of conductivity of a fully dense sample would be 0.043 Scm^{-1}. This value is in reasonably good agreement with many reported data on SDC in air at 800 ◦C. The oxygen partial pressure given on the x-axis is as estimated using the oxygen sensor voltage. The oxygen partial pressures at 200 ◦C are probably not accurate. At any given temperature, the data point corresponding to the lowest pO_2 is that corresponding to the conductivity measured in dry hydrogen.

As stated above, this corresponds to pH_2O approximately between 5×10^{-4} and 5×10^{-3} atm. Since the pH_2O is much higher than pO_2 in the atmosphere, it is assumed that the pH_2O / pH_2 ratio essentially fixes the pO_2 at any given temperature. Thus, the higher the temperature, the higher is the pO_2, which range is between 10^{-52} atm at 200 ◦C and 10^{-25}atm at 800 ◦C [26]. At the lowest measurement temperature of 200 ◦C, the conductivity is essentially independent of pO_2 (actually it somewhat decreases with decreasing pO_2, which may be related to some scatter). At 300 ◦C, the conductivity slightly increases with decreasing pO_2. At 400 ◦C and above, the conductivity clearly increases with decreasing pO_2. Also, the increase in conductivity with decreasing pO_2 occurs at progressively higher pO_2 at higher temperatures, in accord with the

considerable literature on RDC which shows that the electrolytic domain narrows as the temperature increases [1,20]. The increase in conductivity at low pO_2 is thus due to electronic conduction. At any pO_2 at a given temperature, the difference between the broken straight line and the bold curved line in Figure 2.5 is a measure of electronic conduction. At 800 ◦C, significant electronic conduction occurs at values of pO_2 less than about 10^{-10} atm. The typical pO_2 in 'dry' hydrogen as a fuel at 800 ◦C is 10^{-25} atm. At this pO_2 and temperature, the electronic conductivity is about 15 times the ionic conductivity. This is of course well known and thus, RDC is not a suitable electrolyte for SOFC at 800 ◦C (without an electron blocking layer such as YSZ) [4,27]. At 500 ◦C also, significant rise in electronic conduction occurs below about 10^{-16} atm. Matsui et al. [20] have investigated the electrolytic domain of SDC over a temperature range from 400 ◦C to 800 ◦C. These authors also observed significant electronic conduction in hydrogen at a temperature as low as 400 ◦C. The measurements in the work by Matsui et al. [20] were conducted on dense bulk samples. A comparison of their Figure 2 with Figure 2.5 of the present work shows that in the present work, the electrolytic domain is found to be much narrower. For example, Matsui et al. [20] observed electronic conduction at 400 ◦C below a pO_2 of 10^{-32} atm. By contrast, in the present work, electronic conduction is detected below a pO_2 of 10^{-20} atm at 400 ◦C. Similarly, Matsui et al. [20] observed electronic conduction at 800 ◦C below a pO_2 of 10^{-15} atm. In the present work, this transition at 800 ◦C occurs at a pO_2 of 10^{-10} atm. That is, the electrolytic domain measured in the present work is much narrower than reported by Matsui et al. [20]. The principal difference between the two studies is in the use of porous samples in the present work (instead of dense samples in [20]) which allowed rapid equilibration of the sample with the

atmosphere, thereby facilitating accurate determination of the electrolytic domain. Figure 2.6 shows a plot of ln (conductivity × temperature) vs. T^{-1} for the measurements made in pure hydrogen (squares). The data over the temperature range from 300 °C to 800 °C can be reasonably well described by a single activation energy of 101 $kJmol^{-1}$ (the data point at 200 °C is slightly off the line). An additional line shown in the figure is obtained by joining the data points at 200 ◦C and 300 ◦C and extending it over the entire temperature range of the present study. From Figure 2.5, the ionic conductivity at any given temperature regardless of the pO_2 is obtained as the minimum value at the temperature. This is based on the assumption that oxygen vacancy concentration is half the dopant (Sm) concentration in accord with simple defect chemistry. These values are given by the horizontal broken lines in Figure 2.5. These values are also shown in Figure 2.6 (triangles). These points (triangles) lie on the line joining the data points at 200 ◦C and 300 ◦C obtained in hydrogen (squares). As stated earlier, at any temperature, the difference between the two lines (bold and broken) in Figure 2.5 gives the electronic conductivity at the corresponding oxygen partial pressure, pO_2. The data point corresponding to the lowest pO_2 at any temperature is that corresponding to the measurement in hydrogen. For example, at 800 ◦C, the ionic conductivity is 0.024 Scm^{-1} while the measured total conductivity in hydrogen is 0.415 Scm^{-1}. Thus, the electronic conductivity at 800 ◦C in hydrogen is (0.415–0.024) = 0.391Scm^{-1}. At 500 °C, the measured minimum conductivity (ionic) is 1.698×10^{-3} S cm^{-1} while the measured total conductivity in hydrogen is 7.079×10^{-3} Scm^{-1}. Thus, the electronic conductivity at 500 ◦C in hydrogen is $(7.079\times10^{-3}–1.698\times10^{-3}) = 5.381\times10^{-3}$ S cm^{-1}. That is, the ionic transference number of SDC at 500 ◦C in hydrogen is only 0.24. From

Figure 2.6, the estimated ionic transference number of SDC even at 400 ◦C in hydrogen is only 0.4. Triangles in Figure 2.6 correspond to ionic conduction. The corresponding activation energy for oxygen ion conduction is estimated to be 74 kJ mol^{-1}. In the extrinsic regime, the measured activation energy corresponds to that for oxygen vacancy migration. This measurement is in reasonably good agreement with the activation energy of 65 kJ mol^{-1} for oxygen vacancy migration given in a study by Wang et al. [11]. The observation that the electronic conductivity of SDC in hydrogen at 500 ◦C is about 3–4 times that of the ionic conductivity suggests that SDC is not a satisfactory electrolyte even at temperatures as low as 500 ◦C with pure hydrogen as a fuel. That is, the electrolytic domain is rather narrow at 500 ◦C [20]. The same is expected of ceria containing other rare earth oxides as dopants. For application as an electrolyte in SOFC, it would thus be necessary to block off the electronic current through ceria by depositing an electron blocking layer of a predominantly ionically conducting material such as YSZ [4,27]. The preceding conclusions are based on measurements made on samples in hydrogen. In an actual SOFC, the cathode side is exposed to a relatively high pO_2 at which the RDC is a predominantly oxygen ion conductor. The overall transference number of the cell in such a case will be somewhat higher, as previously discussed by Riess [28]. Nevertheless, the general conclusion still is that it may be necessary to block off the electron current by depositing a thin layer of a material such as YSZ on RDC [4,27]. The data in Figure 2.5 at 200 ◦C show that the electronic conductivity of SDC is negligible even at the lowest pO_2 corresponding to pure hydrogen. There is some measurable electronic conductivity at 300 ◦C at the lowest pO_2 at which measurements were made. It is known that electrodes with mixed ionic electronic conduction exhibit

improved electrocatalysis. Any mixed (electronic) conductivity of the composite anode containing RDC as a constituent at low temperatures will be due solely to nickel. In order to introduce MIEC characteristics in single phase RDC at low temperatures (300 ◦C), it may be necessary to dope ceria with an element which exhibits redox characteristics at higher oxygen partial pressures than does cerium.

2.4. Summary

Conductivity of porous samples of Sm_2O_3-doped CeO_2 (SDC) of composition $Sm_{0.15}Ce_{0.85}O_{2-\delta}$ was measured using a 4-probe DC method over a temperature range from 200 ◦C to 800 ◦C in 'pure' oxygen, in 'pure' hydrogen, and in humidified hydrogen. The conductivity rapidly equilibrated even at the lowest measurement temperature of 200 ◦C, which is attributed to fast equilibration of the gas phase in porous interstices and fast compositional (thermodynamic) equilibration in the few micron-sized (5 μm) particles of the porous samples by solid state diffusion. For an assumed oxygen chemical diffusion coefficient, $\tilde{D}_O$ of 10^{-10} cm^2 s^{-1} at a low temperature of 250 ◦C, the required equilibration time in the porous SDC is only about 10 min. A dense sample of 2 mm in thickness, by contrast, would require over a year to equilibrate. The present work thus shows that in order to obtain conductivity values corresponding to thermodynamically equilibrated conditions, measurements should be made on porous samples instead of dense samples. Then the conductivity of dense samples under thermodynamically equilibrated conditions can be obtained using a geometric factor which accounts for porosity and microstructural details [25]. If the interparticle necks are sufficiently wide, the geometric factor is simply related to the volume fraction porosity as given in Eq.

(2.1). A more accurate correction factor will be necessary if the interparticle necks are too narrow [25].

It was observed that SDC became a mixed ionic electronic conductor with increasing temperature and decreasing pO_2.While this result is expected, the present work showed that even at a temperature as low as 500 ◦C, the electronic conductivity of SDC in hydrogen atmosphere is about 4 times the ionic conductivity. The use of porous samples allowed rapid equilibration and facilitated the measurement of true thermodynamically equilibrated properties, which is generally not possible using dense bulk samples due to the long equilibration times required. The present work thus shows that SDC may not be a satisfactory electrolyte for SOFC with pure hydrogen as a fuel without depositing a thin YSZ layer to block off the electronic current [4,27]. At temperatures below about 300 ◦C, however, the electrolytic domain of SDC is wide enough to permit the use of SDC as an electrolyte. The conductivity of SDC at 300 ◦C is, however, rather low and it will be necessary to use it as a thin film to minimize ohmic losses. The observation that SDC exhibits negligible electronic conductivity below 300 ◦C even in a highly reducing environment implies that if used as a constituent in an anode functional layer of a low temperature SOFC, the mixed conductivity will be solely due to the addition of a metallic phase, such as nickel. It may be necessary to dope ceria with elements that exhibit redox properties at higher pO_2 to introduce mixed conductivity in SDC and thereby lower activation polarization. Although the present experiments were conducted only on SDC, it is expected that the conclusions reached here would be broadly applicable to ceria doped with other rare earth oxides. The main conclusion of the work is that the electrolytic domain of RDC appears to be narrower than thought

previously. The use of porous samples facilitated the accurate determination of the electrolytic domain of RDC as a function of temperature and pO_2.

2.5 Acknowledgements

This work was supported in part by the U S Department of Energy under Grant Number DE-FG02-06ER46086 and DOE EFRC Grant Number DE-SC0001061 as a flow through from the University of South Carolina.

2.6 References

1) H. L. Tuller, A. S. Nowick, J. Electrochem. Soc. 122 (2) (1975) 255–259.

2) D.Y. Wang, A. S. Nowick, J. Solid State Chem. 35 (3) (1980) 325–333.

3) D. Braunshtein, D. S. Tannhauser, I. Riess, J. Electrochem. Soc. 128 (1) (1981) 82–89.

4) H. Yahiro, Y. Baba, K. Eguchi, H. Arai, J. Electrochem. Soc. 135 (8) (1988) 2077–2080.

5) T. Inoue, T. Setoguchi, K. Eguchi, H. Arai, Solid State Ionics 35 (34) (1989) 285–291.

6) H. Yahiro, K. Eguchi, H. Arai, Solid State Ionics 36 (12) (1989) 71–75.

7) K. Eguchi, T. Setoguchi, T. Inoue, H. Arai, Solid State Ionics 52 (1–3) (1992) 165–172.

8) K. Yamashita, K. V. Ramanujachary, M. Greenblatt, Solid State Ionics 81 (12) (1995) 53–60.

9) S. J. Hong, K. Mehta, A. V. Virkar, J. Electrochem. Soc. 145 (2) (1998) 638–647.

10) Z. Zhan, T. Wen, H. Tu, Z. Lu, J. Electrochem. Soc. 148 (5) (2001) A427–A432.

11) S. Wang, T. Kobayashi, M. Dokiya, T. Hashimoto, J. Electrochem. Soc. 147 (10) (2000) 3606–3609.

12) F. Wang, S. Chen, S. Cheng, Electrochem. Commun. 6 (8) (2004) 743–746.

13) T. Matsui, T. Kosaka, M. Inaba, A. Mineshige, Z. Ogumi, Solid State Ionics 176 (78) (2005) 663–668.

14) D.A. Andersson, S.I. Simak, N. V. Skorodumova, I. A. Abrikosov, B. Johansson, Proc. Natl. Acad. Sci. U.S.A. (2006) 1–6.

15) G. B. Balazs, R. S. Glass, Solid State Ionics 76 (1995) 155–162.

16) R. T. Dirstine, R. N. Blumenthal, T. F. Kuech, J. Electrochem. Soc. 126 (1979) 264.

17) H. Yahiro, Y. Eguchi, K. Eguchi, H. Arai, J. Appl. Electrochem. 18 (1988) 527–531.

18) K. Eguchi, J. Alloys Compd. 250 (1997) 486–491.

19) V. V. Kharton, F. M. Figueiredo, L. Navarro, E. N. Naumovich, A. V. Kovalevsky, A. A. Yaremchenko, A. P. Viskup , A. Carneiro, F. M. B. Marques, J. R. Frade, J. Mater. Sci. 36 (2001) 1105–1117.

20) T. Matsui, M. Inaba, A. Mineshige, Z. Ogumi, Solid State Ionics 176 (2005) 647–654.

21) H. Inaba, H. Tagawa, Solid State Ionics 83 (1996) 1–16.

22) H. Yahiro, T. Ohuchi, K. Eguchi, H. Arai, J. Mater. Sci. 23 (1988) 1036–1041.

23) Z. Tianshu, P. Hing, H. Huang, J. Kilner, Solid State Ionics 148 (2002) 567–573.

24) E. L. Cussler, Diffusion: Mass Transfer in Fluid Systems, Cambridge University Press, Cambridge, UK, 1995.

25) F. Zhao, A. V. Virkar, J. Power Sources 195 (2010) 6268–6279.

26) D. R. Gaskell, Introduction to the Thermodynamics of Materials, third ed., Taylor & Francis, Washington, DC, 1995.

27) A. V. Virkar, J. Electrochem. Soc. 138 (5) (1991) 1481–1487.

28) I. Riess, J. Electrochem. Soc. 128 (10) (1981) 2077–2081.

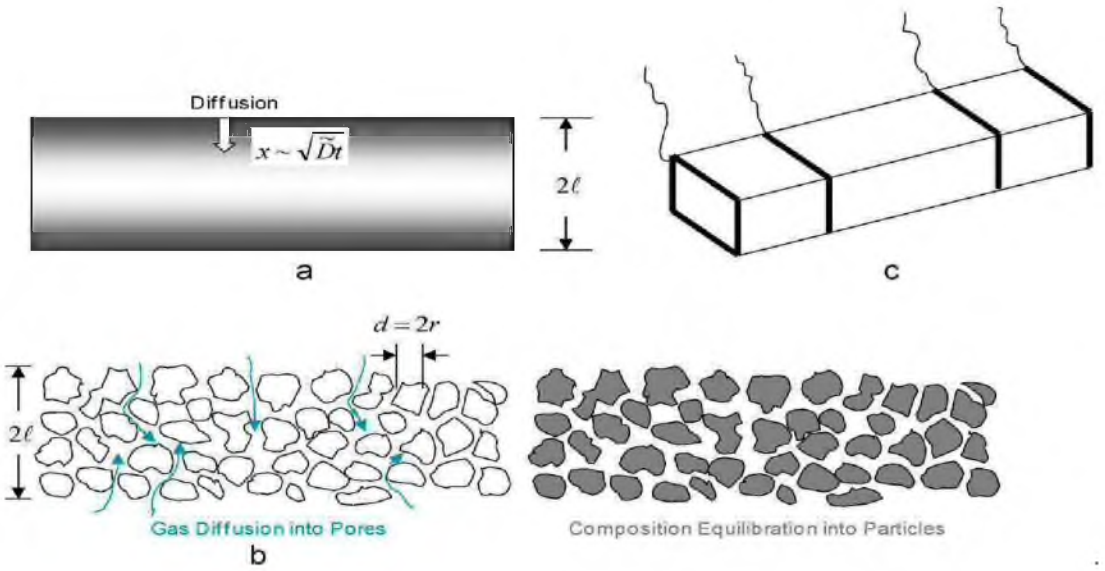

Figure 2.1. (a) A schematic of the equilibration kinetics in a dense sample. The diffusion distance is given by x ~ D*t, where ~D is the chemical diffusion of the diffusing species (e.g., oxygen). (b) A schematic showing the equilibration kinetics in a porous sample of the same external dimensions as the dense sample. The process involves gas phase diffusion within the porous interstices and solid state diffusion within the particles. Gas phase equilibration occurs rapidly due to the high effective gas phase diffusivity (0.1cm^2 s−1). Rapid solid state diffusion occurs due to the small particle size. (c) A schematic of the samples used for the 4-probe DC conductivity measurements

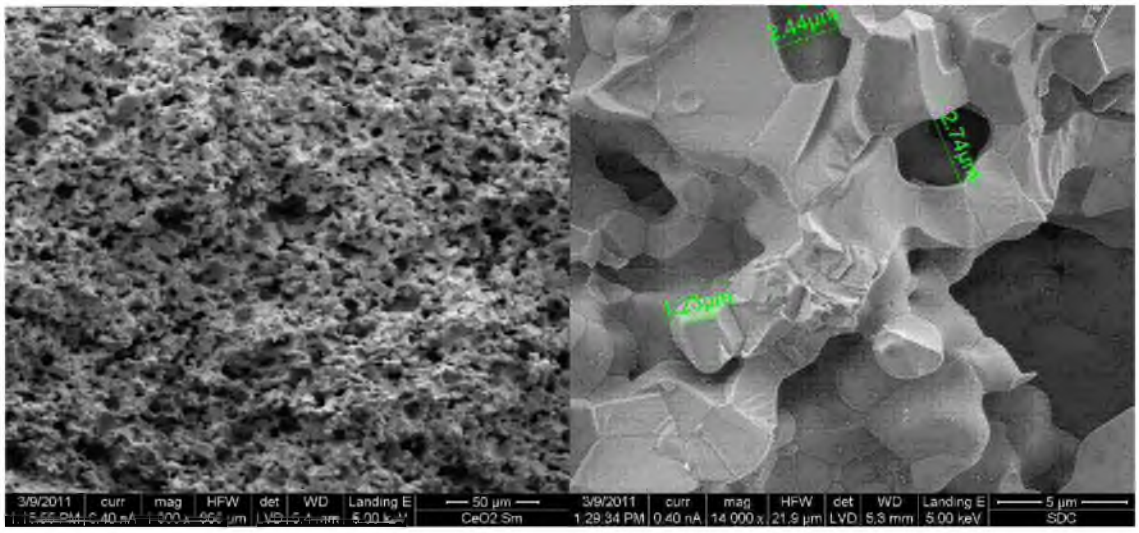

(a) (b)

Figure 2.2. SEM micrographs of a porous SDC sample used in the study
(a) An SEM micrograph of a porous SDC sample. The volume fraction porosity is 0.45. (b) A higher magnification SEM micrograph showing the morphology; the particle size, and the interparticle neck size.

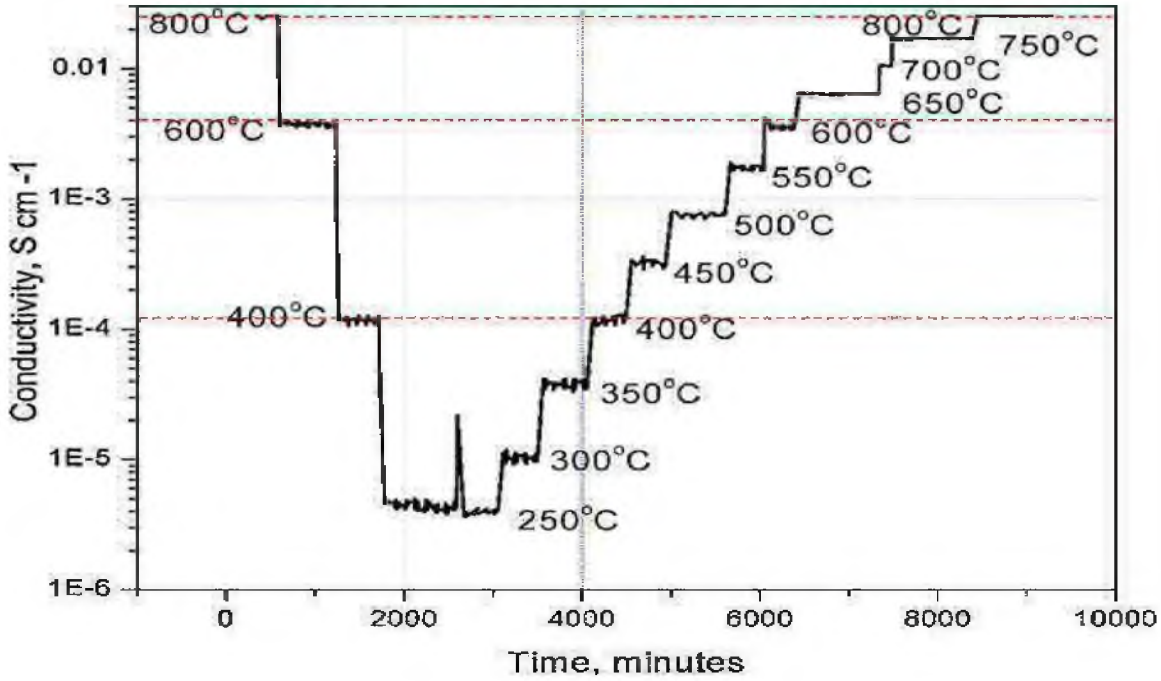

Figure 2.3. Conductivity of a porous SDC sample measured by a 4-probe DC technique in humidified hydrogen over a temperature range from 250 ◦C to 800 ◦C. Measurements were made during cooling and heating. Conductivity rapidly equilibrated even at the lowest temperature of 250 ◦C. Also, conductivity at a given temperature was the same during both cooling and heating. The spike at 250 ◦C is due to temporary malfunction of the recording instrument.

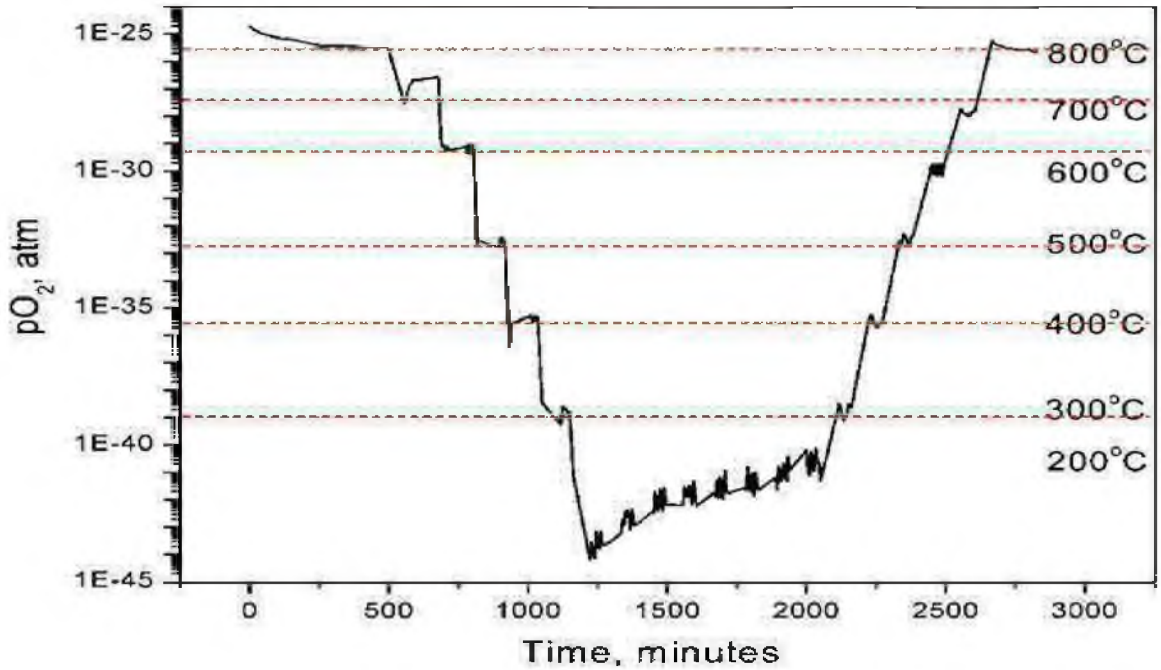

Figure 2.4. Estimated oxygen partial pressure as a function of temperature in hydrogen. Above 300 ◦C, the estimated oxygen partial pressure at a given temperature is about the same during cooling and heating.

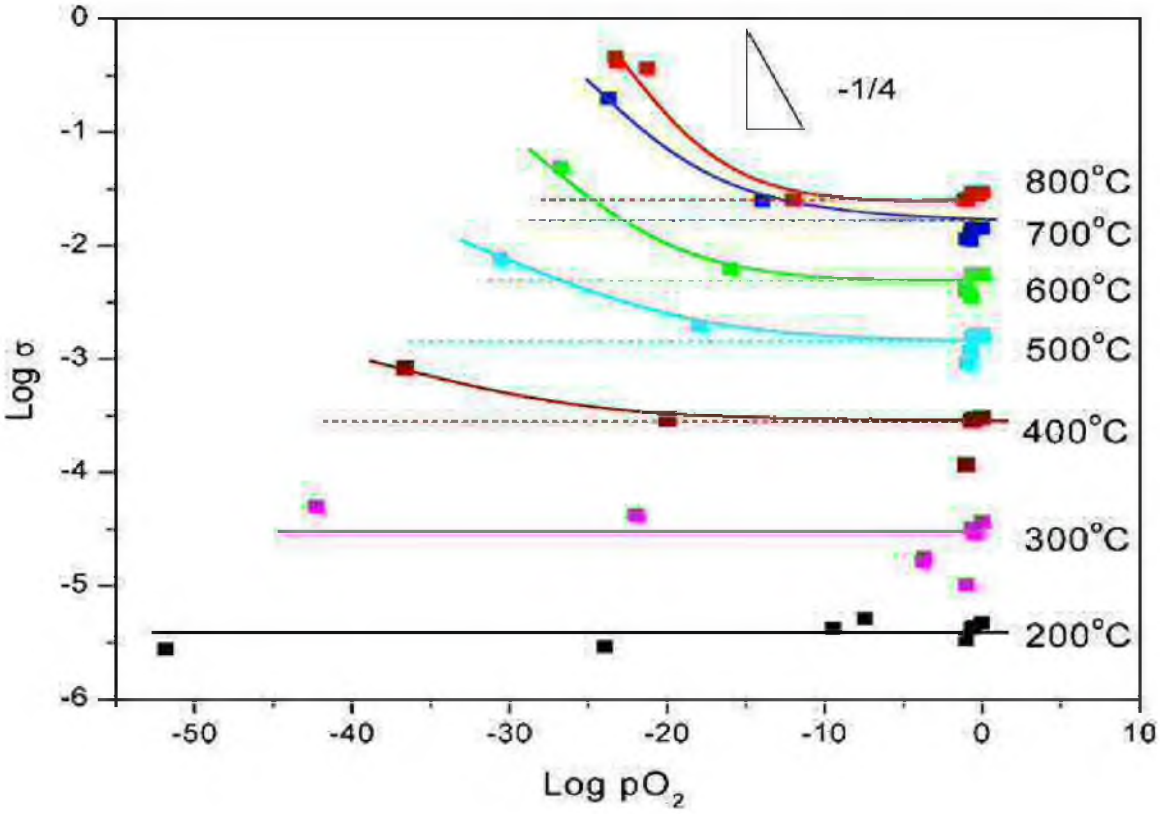

Figure 2.5. Conductivity as a function of oxygen partial pressure over a temperature range from 200 ◦C to 800 ◦C. These data were obtained on another sample. Representative SEM micrographs are given in Figure 1.2. The horizontal broken lines correspond to the ionic conductivity. Higher total conductivity at lower oxygen partial pressures is due to the contribution from electronic conduction. Significant electronic conduction occurs at 400 ◦C (and above) in hydrogen. The oxygen partial pressure dependence of electronic portion of the conductivity is given by $\sigma_{elec} \quad pO_2^{-1/4}$. The inset shows a line with a slope of −1/4

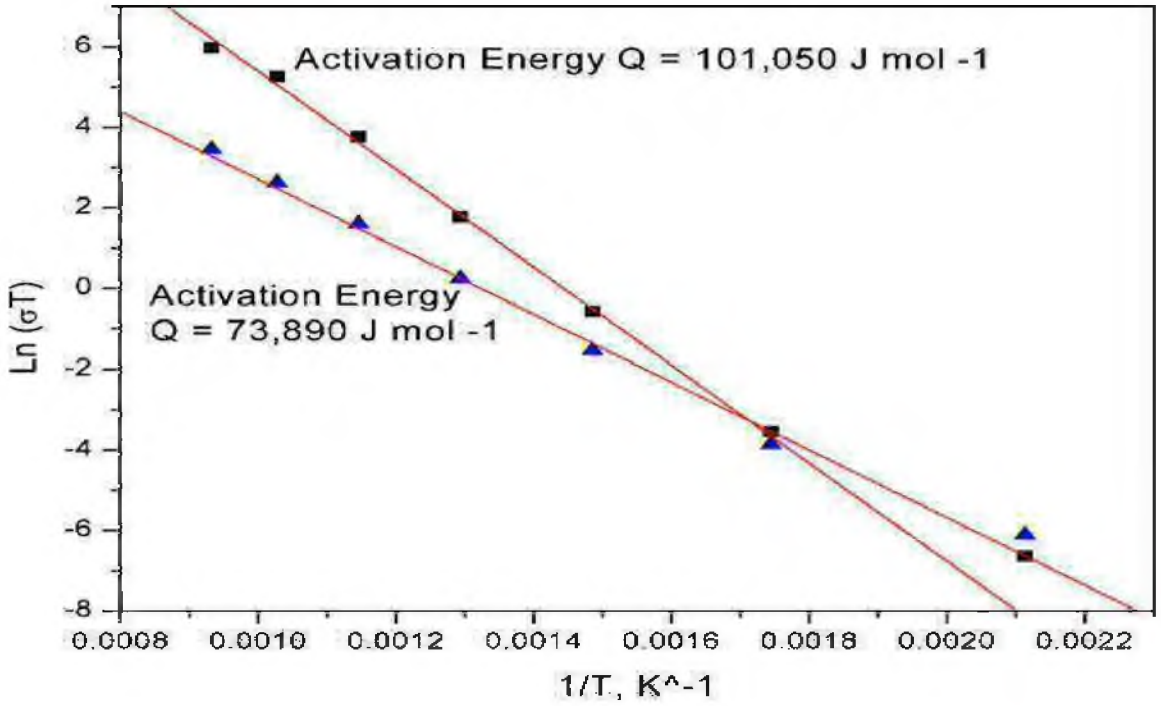

Figure 2.6. Arrhenius plot of (conductivity × temperature) vs.1 / temperature for the sample tested in hydrogen. Fit to data points at 200 ◦C and 300 ◦C extrapolated to higher temperatures corresponds to ionic conductivity. The corresponding activation energy is 74 kJ mol^{-1}. Fit to data points between 300 ◦C and 800 ◦C gives an activation energy of 101 kJ mol^{-1}. Despite a linear plot on the semi-log scale, this does not represent unique activation energy because of the significant electronic conduction at higher temperatures. The triangles are the data corresponding to the minimum values of the measured conductivity as a function of oxygen partial pressure at various temperatures. These correspond to ionic conduction.

CHAPTER 3

ELECTRICAL CHARACTERIZATION AND WATER SENSITIVITY OF $Sr_2Fe_{1.5}Mo_{0.5}O_{6-\delta}$ AS A POSSIBLE SOLID OXIDE FUEL CELL ELECTRODE

Originally published in Journal of Power Sources 237 (2013) 13-18

Reprinted with permission

3.1 Introduction

Many perovskite materials containing transition metal ions are known to be mixed ionic electronic conductors. Examples include Sr-doped $LaFeO_3$ (LSF), Sr-doped $LaCoO_3$ (LSC), Sr-doped La $(Co,Fe)O_3$ (LSCF), and similar compounds [1-3]. Several perovskites also exhibit order disorder transitions when either the A and/or the B site contains ions of different valences. In the ordered state, they may form double or triple perovskites. Some of the examples of materials exhibiting order-disorder phenomena include ferroic materials such as lead scandium tantalite (PST) and lead magnesium niobate [4,5]. One of the perovskite materials that has been extensively studied is Sr_2FeMoO_6 (SFMO), in which Fe and Mo exhibit order leading to a double perovskite unit cell. By virtue of the presence of iron, this material is known to exhibit many interesting electronic and magnetic properties [6]. For example, SFMO exhibits colossal magnetoresistance (CMR), tunneling magnetoresistance across grain boundaries, and a high Curie temperature (~415 K). Recent investigations have focused on applications in spintronics and in plasmonics [7-10].

Similar to many other perovskites, SFMO exists over a considerable range of stoichiometries leading to varied properties. For example, this material can also be fabricated with excess Fe and deficient Mo, such as $Sr_2Fe_{1.5}Mo_{0.5}O_{6-\delta}$. Excess Fe and deficient Mo are compensated for by the creation of electronic defects and oxygen vacancies. As such, it is an ideal candidate as a mixed ionic electronic conductor (MIEC). Recent work has shown that it functions well as both a cathode and an anode in solid oxide fuel cells (SOFC), indicating that it exhibits good electrical transport properties and catalytic activity in oxidizing and reducing atmospheres [11,12]. Electrical conductivity

was also measured in both oxidizing and reducing atmospheres [11,12]. Measurements of electrical conductivity were made on sintered, bulk samples, which is the standard procedure used in most studies.

While SFMO exhibits interesting properties for potential application in SOFCs, there are several references which have reported instability of SFMO under various conditions. It has been reported that SFMO has a narrow pO_2 window of stability, between ($-9.8 > \log pO_2 > -13.5$) at 1200 °C [13]. In another study, similar results were obtained in which a pO_2 stability range between ($-10.2 < \log pO_2 < -13.7$) at 1200 °C was reported [14]. It was also reported that SFMO reacts with water, to the extent that total decomposition occurs when in contact with water [15]. Other investigators determined that SFMO is unstable over time in air at temperatures greater than 400 °C, and that it quickly disintegrates into $SrMoO_4$ and $SrFeO_{3-x}$ [16]. Yet another study found a sign change in the temperature coefficient of resistivity of SFMO. These authors proposed that growth of an insulating layer occurs at the grain boundaries [17]. Finally, SFMO has been reported to be unstable even at room temperature in air, leading to unit cell expansion over time promoting phase decomposition [18].

The objective of the present study was to investigate electrical conductivity on porous samples of SFMO as a function of temperature and in various atmospheres. The reasons for making measurements on porous samples are three fold. First, from a practical standpoint, measurements made on porous samples are directly applicable to the design of SOFC electrodes, which are porous. Second, from a fundamental standpoint, measurements made on porous samples allow the determination of properties under thermodynamically equilibrated conditions [19,20]. This is because thermodynamic

equilibration occurs orders of magnitude faster in porous samples than in sintered, bulk samples due to fast gas phase equilibration in porous interstices and rapid solid state equilibration in micron-sized particles [19,20]. This allows measurements under thermodynamically equilibrated conditions at exceptionally low temperatures. For example, our previous work on Sm-doped CeO_2 (SDC) demonstrated rapid equilibration in porous samples at temperatures as low as 200 °C [20]. The work on porous SDC samples demonstrated that the electrolytic domain of SDC at 400 °C was much narrower than previously believed [20]. Also, any possible reactivity of a material with atmosphere can be investigated in a reasonable period of time on porous samples unlike measurements on dense samples. Such reactivity will most certainly occur in the actual devices because of the use of porous electrodes, but may not become noticeable when measurements are made on dense samples. Third, the presence of alkaline earth (here, Sr) increases the potential for reaction with water-containing atmospheres, especially at low temperatures, which can be studied more conveniently and in a reasonable period of time on porous samples than on dense samples. It is known, for example, that many inorganic oxides containing either alkali (Na, K, etc.) or alkaline earth (Ba, Ca, Sr, etc.) metals react with water at low temperatures to form the corresponding bases. For over two decades, Sr_2FeMoO_6 (SFMO) has been investigated for applications in magnetic storage, read/write heads, and similar devices. The current commercial status, however, has not yet gone beyond prototype devices due in part to the instability of the material. The objective of the present study was to investigate properties of porous SFMO over a wide range of temperatures and assess the implications concerning its water sensitivity for applications in SOFC.

3.2. Experimental Procedure

$Sr_2Fe_{1.5}Mo_{0.5}O_{6-\delta}$ (SFMO) powder was synthesized using the following procedure. Stoichiometric amounts of $Sr(NO_3)_2$ and $(NH_4)_6Mo_7O_{24}\cdot 4H_2O$ were dissolved into distilled water to form an aqueous solution. Glycine (0.5 mol glycine per mol of NO_3) and citric acid (0.05 mol citric acid per mol of NO_3) were subsequently added to the solution as a binder and as a pH adjuster. $Fe(NO_3)_3\cdot 9H_2O$ was then added in the solution and a dark reddish solution was eventually obtained. The solution was then heated in a microwave oven until self-ignition occurred. The ash was collected and calcined at 1000 °C for 5 h. The as-synthesized powder was mixed with 15% Spherodur carbon (by weight). Carbon was added to ensure that the sintered samples exhibit some open porosity. Bars of cross-sections 3 mm x 10 mm and 3 mm x 6 mm were die-pressed.

The bars were heated in air in a furnace to 1200 °C for 2 h, and then cooled to room temperature. Platinum paste (ESL Electroscience, Type 5542 Print GD) was applied in the form of four stripes on the samples to form contacts for 4-probe conductivity measurements. The samples were then heated to 900 °C to bond the platinum contacts to the $Sr_2Fe_{1.5}Mo_{0.5}O_{6-\delta}$ sample surface. Platinum wires were then attached to the 4 contacts. The samples were inserted into a Barnstead Thermolyne 21100 tube furnace. The ends of the tube were fitted with rubber stoppers and all feed-throughs were inserted through the rubber stoppers. Keithley 2000 multimeters were used for voltage and current measurements. A zirconia oxygen sensor (CoorsTek) was used to measure the oxygen partial pressure inside the tube close to the sample. The temperature inside the tube furnace was monitored using Omega Engineering Type K thermocouple (Omega part # CHAL-020). Cylinders of ultra-high-purity hydrogen, 10% Hydrogen – 90% Nitrogen,

and compressed air were used to vary the atmosphere inside the tube furnace.

Constant, regulated current (usually < 15 mA) was supplied to the sample using a Keithley 6220 precision current source, and monitored with another Keithley 2000 multimeter. The four Keithley 2000 multimeters were monitored using LabView software on a PC. For each atmosphere investigated, the temperature was varied between 800 °C and 200 °C in 100 degree steps. Initially, the sample/furnace was heated to 800 °C and the sample conductivity was measured. Thereafter, the temperature was lowered to 200 °C in 100 degree steps. At each temperature, the conductivity was measured after the sample temperature had equilibrated. Prior work has shown that the kinetics of thermodynamic equilibration of porous samples under imposed conditions is very rapid as long as the material is stable under conditions [20]. Thus, as soon as temperature has equilibrated, the sample thermodynamically equilibrates rapidly [20]. After the measurement at 200 °C, the sample was reheated to 800 °C and the procedure was repeated. These two repetitions are labeled "1st expt" and "2nd expt" in the figures. Each step was approximately 8 h long. Only one data point (800 °C) in 10% H_2 could be obtained as the sample failed during testing. It is speculated that reaction products formed on the surfaces of exposed particles of porous SFMO led to volume changes, which resulted in cracking of the sample.

After the testing was complete, the sample was removed from the furnace. It was observed that the sample had fractured into a few pieces. The fragments were examined by XRD and SEM. Another sample was selected for Archimedes density measurement. The sample was weighed dry in air, weighed while submerged in water, and weighed in air after boiling in water and wiping off surface water. The as-synthesized powder was

also submerged in water for 3 days. The powder was then removed, dried in a Lindberg/Blue M oven at 50 °C, and heated to 800 °C in air for 24 h. The powder was weighed after each step.

3.3. Results and Discussion

Figure 3.1 shows an XRD trace of the as-synthesized SFMO powder obtained with CuKα radiation. The trace is consistent with single phase SFMO of the double perovskite structure with a lattice parameter of 0.7826 nm. Figure 3.2 shows the measured DC 4-probe conductivity of a sample as a function of temperature on an Arrhenius plot over a temperature range between 200 °C and 800 °C. The red and black squares correspond respectively to measurements made during the first and the second run, both in 100% H_2 atmosphere, during cooling from 800 °C to 200 °C in 100 degree steps. It was observed that during the second run, the measured conductivity was considerably lower than during the first run, especially at lower temperatures. Triangles and crosses in Figure 3.2 respectively correspond to measurements made during the first and the second run in air. Greater deviation is observed at higher temperatures, although the trends are not so clear in these sets of measurements. Figure 3.3 shows the measured conductivity as a function of time for the measurements made in hydrogen. Also plotted in the figure is the temperature vs. time trace for the two runs as the temperature was varied between 800 °C and 200 °C. Note that stable conductivity values were recorded during the first run from 800 °C to 200 °C at each temperature. However, when the sample was reheated to 800 °C during the second run, stable conductivity value was not achieved over the period the sample was maintained at 800 °C (about 8 h). The conductivity

increased over the duration of this step. This observation suggests that some instability (reaction) occurred at low temperatures, and some changes in the material continued to occur when the sample was heated to 800 °C. Stable values of conductivity were not observed during the second run, as seen in Figure 3.3. The corresponding data for the two runs are shown as squares in Figure 3.2. At the end of conductivity measurements, an XRD trace of the sample was obtained. The two XRD traces of the sample, before and after testing, are compared in Figure 3.4. The same XRD peaks are present in both spectra, although some peak broadening seems to have occurred in the sample after testing. The absence of detectable amounts of reaction products in the XRD trace after conductivity tests is attributed to relatively sluggish reaction kinetics when H_2O is present in a vapor form such as at 200 °C. Under such conditions, any water soluble reaction product (e.g., $Sr(OH)_2$) cannot be removed, thus slowing down kinetics. Similar conductivity measurements on porous SDC showed very stable and reproducible values during heating and cooling, consistent with the fact the SDC is stable over the range of temperatures and atmospheres tested [20].

A sample of porous sintered SFMO was boiled in water for the measurement of density. Figure 3.5 shows photographs of the sample before and after boiling. The pristine sample was black in color. However, after boiling in water, the sample color had changed to brick red. Such a change in color is consistent with Fe^{2+} to Fe^{3+} transition. XRD traces of the sample before and after boiling are shown in Figure 3.6. As clearly seen in the XRD traces, additional XRD peaks were observed in the as-boiled sample. These additional peaks could be identified as belonging to Fe_3O_4, $SrMoO_4$, and SrO_2. No further characterization tests were conducted to determine if indeed SrO_2 was formed. It

is nevertheless clear that SFMO readily reacts with water when boiled for just a few minutes. When boiled in water, soluble reaction products such as $Sr(OH)_2$ can be continuously removed from the reaction sites, thus increasing the kinetics of the reaction. Indeed, similar differences in the kinetics of reaction of H_2O with alkaline earth cerates have been observed between liquid H_2O and vapor H_2O [21,22].

In order to further study reactivity of SFMO with water, a powder sample (0.5001 g) placed in a crucible was immersed in water and maintained for 3 days. After 3 days, the crucible was placed in an oven at 50 °C until the powder was fully dry. The crucible contained dry powder at the bottom and some condensate on the sides of the crucible. The color of the powder had changed from black to red. The crucible with the powder was again weighed. The corresponding weight of the powder + condensate was measured to be 0.6718 g, showing a significant increase in weight. The condensate from the crucible walls was removed and weighed. The weight of the condensate was 0.0608 g. The remaining powder was heated to 800 °C in air, maintained at temperature for 24 h, and then cooled to room temperature. The weight of the powder after this heat treatment was measured to be 0.5613 g, which is still greater than the initial weight of the powder. This experiment showed that a significant increase in weight occurred when treated in water. It also showed that heat treatment at 800 °C was not sufficient for solid state reactions to occur. This is evidenced by the observation that even after treatment at 800 °C, the powder weight (0.5613 g) was greater than the initial weight (0.5001 g), even when the weight of the condensate on crucible walls was excluded. An XRD trace of the condensate deposited on crucible walls is shown in Figure 3.7. The observed XRD peaks could be identified with mixed oxides and hydroxides of Sr, Fe, and Mo. No further

characterization was conducted. However, the instability of SFMO in water-containing atmospheres at low temperatures was clearly documented. Instability of SFMO in water-containing atmospheres is not surprising. It is indeed well known that many oxides containing alkaline earth elements react with water to form highly basic alkaline earth hydroxides. Thus, the observed reactivity of SFMO with water is in accord with expectations.

No thermodynamic data are available for SFMO to the authors' knowledge. However, it is known that Sr_2TiO_4 is unstable in water and readily reacts with H_2O to form $SrTiO_3$ and $Sr(OH)_2$, for which thermodynamic data are available [23]. At 300 K, the standard free energy for the reaction $Sr_2TiO_4 + H_2O \rightarrow SrTiO_3 + Sr(OH)_2$ is $\Delta G_o = -61.2$ kJ.mol^{-1} [23]. The corresponding equilibrium activity of H_2O, namely a_{H2O}, is estimated to be ~2.2 x 10^{-11}. This means even in a relatively dry atmosphere, Sr_2TiO_4 would react with trace amounts of H_2O. This has been experimentally confirmed. In fact, its reactivity with H_2O is put to good use in a patented process for the synthesis of nanosize $SrTiO_3$ [24]. By contrast, at 1000 K the standard free energy change for $Sr_2TiO_4 + H_2O \rightarrow SrTiO_3 + Sr(OH)_2$ is ~ - 8 kJ.mol-1, which is much smaller than at 300 K [23]. Within the uncertainty limits of the available data, it is clear that little thermodynamic force exists at 1000 K for the reaction between Sr_2TiO_4 and H_2O to proceed to form $SrTiO_3$ and $Sr(OH)_2$. Thus, it is expected that Sr_2TiO_4 would be stable in the presence of H_2O at high temperatures but not at low temperatures. The behavior of SFMO is very similar to that of Sr_2TiO_4. By virtue of the somewhat higher concentration of Sr in SFMO, its reactivity with water is not surprising, as observed. One of the products after the reaction with water was observed to be $SrMoO_4$. This shows that $SrMoO_4$, which

contains a lower concentration of Sr than SFMO, is stable in contact with water. Thus, the instability of Sr_2TiO_4 in water at low temperatures is similar to the instability of SFMO in water; and the stability of $SrTiO_3$ in water is similar to the stability of $SrMoO_4$ in water.

The present observations have significant implications concerning potential applications of SFMO in SOFC as an electrode. It is expected that if maintained at the operating temperature, typically 800 °C, the cells containing SFMO would exhibit chemical stability, and possibly reasonable performance as has already been demonstrated [11,12]. However, whenever the cells are cooled to room temperature, it is expected that SFMO will react with moisture in the atmosphere. This will lead to the formation of various hydroxides, principally $Sr(OH)_2$. For short-term exposures to moisture, such as is present in even dry environments, the formation of trace amounts of $Sr(OH)_2$ is expected. This would lead to a decrease in ionic / electronic conductivity and especially decrease in catalytic activity. When heated back to the SOFC operating temperature, which is typically 800 °C, the reaction of $Sr(OH)_2$ with Fe-Mo-oxides is not expected to occur in a reasonable period of time due to sluggish kinetics of solid state reactions. Indeed it was observed that after a few hours at 200 °C, the original electrical conductivity at 800 °C could not be recovered in 8 h, as seen in Figure 3.3. Much higher temperatures, perhaps 1200 °C, would be required for re-forming SFMO. Such a high temperature treatment is not possible with any of the SOFC components currently in use or under development. Thus, damage developed at low temperatures during thermal cycling is expected to be cumulative. For example, based on the present work, it is expected that once the reaction with H_2O vapor occurs on the surfaces of the particles of

a porous body, the products will lead to a local increase in volume. This increase in volume cannot be accommodated by any other means than cracking due to the fact that the material is brittle. The observation that after the conductivity measurements the sample cracked into multiple pieces is in accord with expectations. Similar behavior is expected of an SOFC electrode after repeated thermal cycling. The volume change will likely lead to electrode delamination. The reactivity of SFMO with water at low temperatures appears to be the principal impediment to its possible application as an SOFC component.

3.4. Summary

SFMO powder was synthesized by a combustion process. Bar-shaped porous samples were fabricated by sintering and 4-probe DC electrical conductivity was measured in air and in hydrogen over a range of temperatures between 200 and 800 °C. Reactivity of SFMO with water was investigated at low temperatures. It was observed that SFMO readily reacted with water to form $Sr(OH)_2$. Upon reheating to 800 °C, the formed $Sr(OH)_2$ did not react back to form SFMO. In an SOFC application, it is expected that damage created at low temperatures during cycling will be cumulative. This imposes severe restrictions on any potential applications of SFMO in fuel cells.

3.5 Acknowledgements

This material is based upon work supported as part of the HeteroFoaMCenter, an Energy Frontiers Research Center funded by the U.S. Department of Energy, Office of Science, Office of Basic Energy Sciences under Award Number DE-SC0001061.

3.6 References

1) T. Kenjo, T. Maruyama, T. Yoshida, Y. Kouno, Y. Saito, Report of the Research Laboratory of Engineering Materials, Tokyo Institute of Technology 11 (1986) 17 –26.

2) Y. Ohno, S. Nagata, H. Sato, Solid State Ionics 3–4 (1981) 439–442.

3) Y. Teraoka, H. M. Zhang, K. Okamoto, N. Yamazoe, Mat. Res. Bull. 23 (1) (1988) 51-58.

4) B.I. Birajdar, A. Chopra, M. Alexe, D. Hesse, ActaMaterialia 59 (2011) 4030–4042.

5) C. Stock, G. Xu, P. M. Gehring, H. Luo, X. Zhao, H. Cao, J. F. Li, D. Viehland, G. Shirane, Physical Review B 76 (2007) 064122.

6) D. D. Sarma, S. Ray, Proc. Indian Acad. Sci. (Chem. Sci.) 113 (5 & 6) (2001) 515–525.

7) M. Ziese, Rep. Prog. Phys. 65 (2002) 143–249.

8) K. Dorr, J. Phys. D: Appl. Phys. 39 (2006) R125–R150.

9) D. Serrate, J. M. De Teresa, M. R. Ibarra, J. Phys.: Condens. Matter 19 (2007) 023201

10) N. E. Massa, J. A. Alonso, M. J. Martínez-Lope, M. T. Casais, Physical Review B 72 (2005) 214303

11) Q. Liu, X. Dong, G. Xiao, F. Zhao, F. Chen, Adv. Mater. 22 (2010) 5478–5482.

12) Q. Liu, D. E. Bugaris, G. Xiao, M. Chmara, S. Ma, H. zur Loye, M. D. Amiridis, F. Chen, J. Power Sources 196 (2011) 9148– 9153.

13) T. Nakamura, K. Kunihara, Y. Hirose, Mat. Res. Bull. 16 (1981) 321- 326.

14) R. Kircheisen, J. Topfer, J. Solid State Chem. 185 (2012) 76–81.

15) T. Suominen, Turun Yliopiston Julkaisuja Annales Universitatis Turkuensis, Sarja - SER. A I OSA-TOM. (2009).

16) L. H. Son, N. X. Phuc, P. V. Phuc, N. M. Hong, L. V. Hong, J. Raman Spectrosc. 32 (2001) 817–820.

17) S. Ray, A. Kumar, S. Majumdar, E. V. Sampathkumaran, D. D. Sarma, J. Phys.: Condens. Matter 13 (2001) 607–616.

18) J. Navarro, C. Frontera, D. Rubi, N. Mestres, J. Fontcuberta, Mat. Res. Bull. 38 (2003) 1477–1486.

19) F. Zhao, A. V. Virkar, J. Power Sources 195 (2010) 6268-6279.

20) J. Wright, A. V. Virkar, J. Power Sources 196 (15) (2011) 6118-6124.

21) S. V. Bhide, A. V. Virkar, J. Electrochem. Soc. 146 (6) (1999) 2038-2044.

22) C. W. Tanner, A. V. Virkar, J. Electrochem. Soc. 143 (4) (1996) 386-1389.

23) I. Barin, Thermochemical Data of Pure Substances: Parts I and II, VCH Publication, Weinheim, Germany, 1993.

24) A. V. Virkar, S. V. Bhide, Molecular Decomposition Process for the Synthesis of Nanosize Ceramic and Metallic Powders, US Patent No. US 6,803,027 B1: Date of Issue: October 12, 2004.

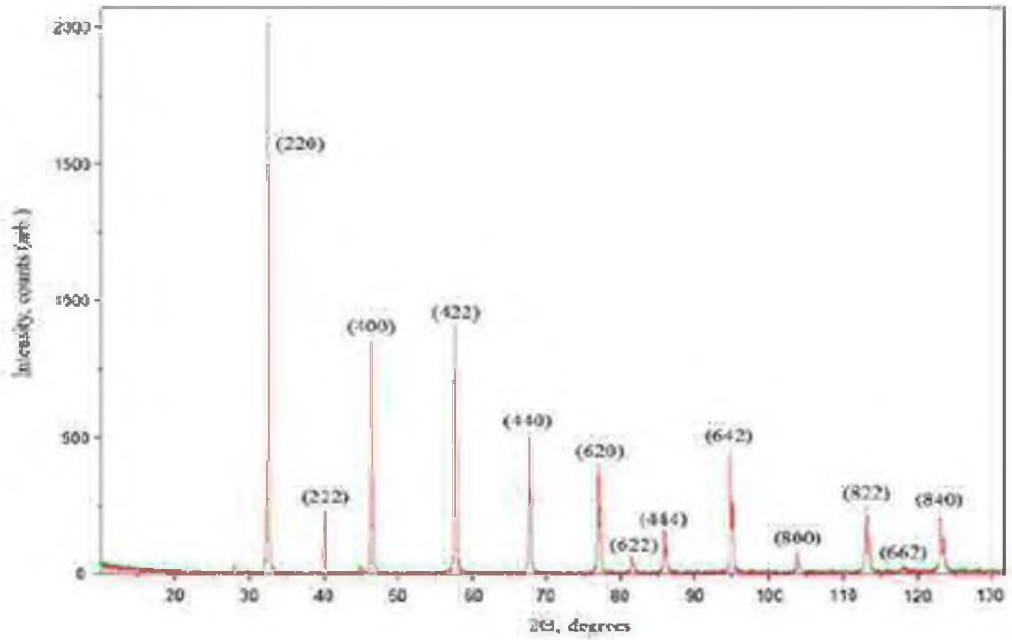

Figure 3.1: An XRD trace of the as-synthesized $Sr_2Fe_{1.5}Mo_{0.5}O_{6-d}$ (SFMO) powder.

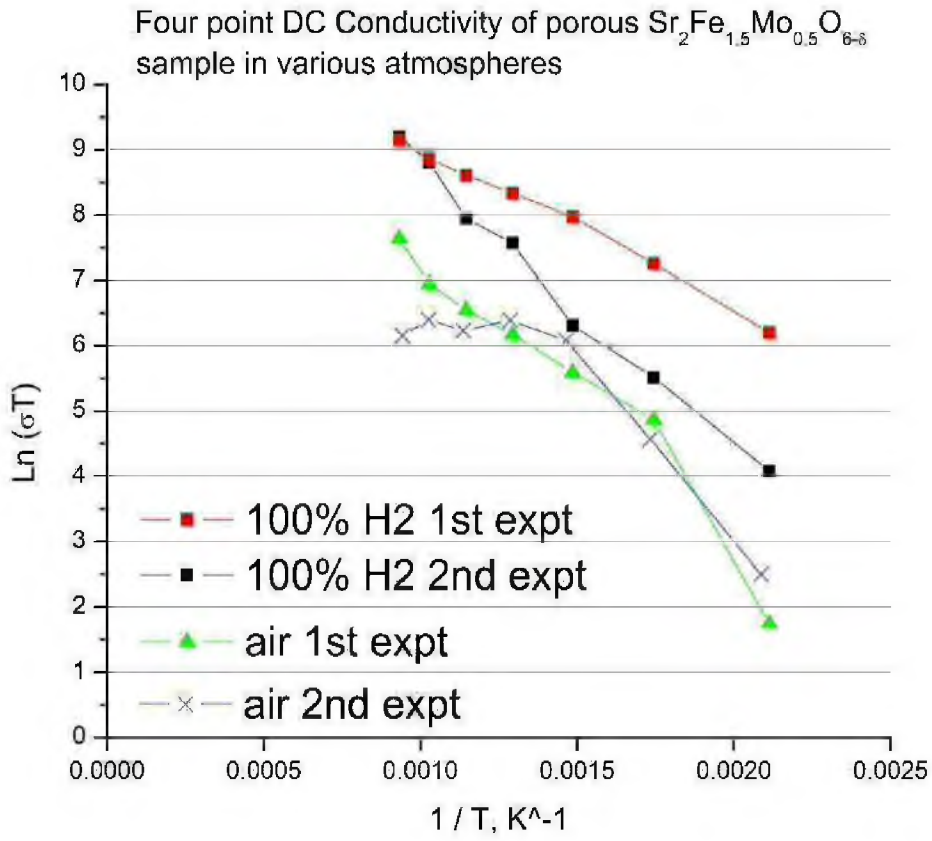

Figure 3.2: An Arrhenius plot of conductivity vs. temperature measured on a porous SFMO sample in hydrogen and in air during two consecutive experiments.

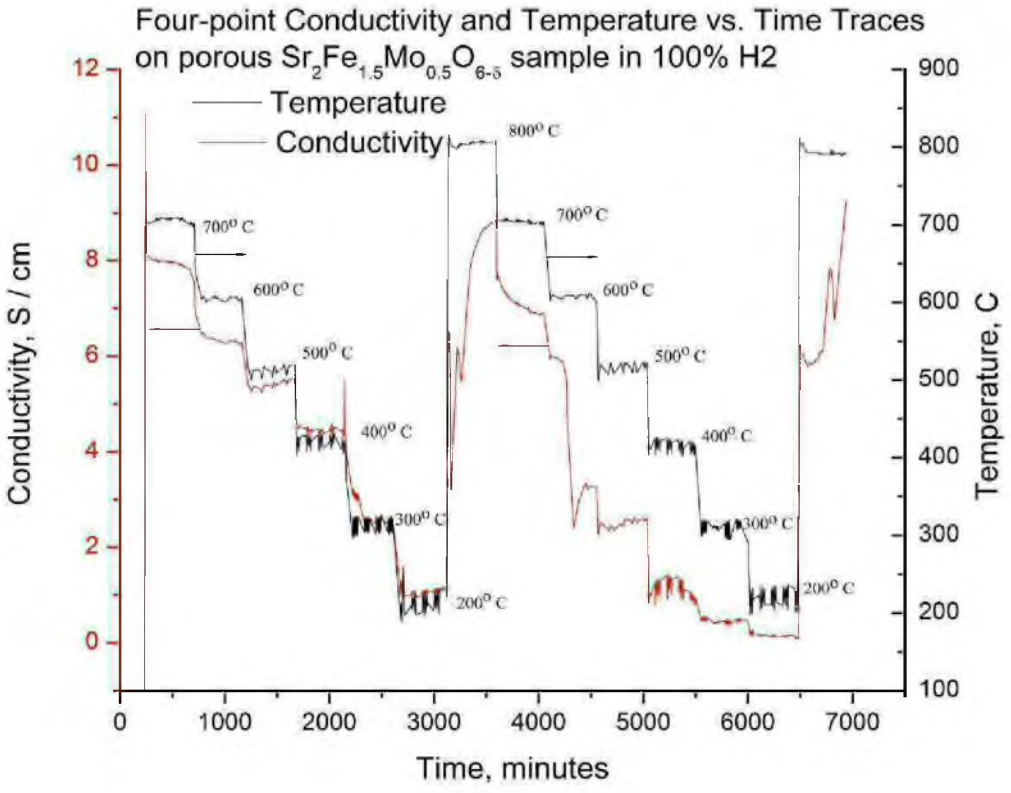

Figure 3.3: Conductivity vs. time for measurements made over a range of temperatures between 800 ◦C and 200 ◦C during two consecutive experiments. Also plotted in the figure is the corresponding temperature vs. time plot. Note that during the second run, stable values of conductivity were not observed. This is attributed to the reaction of SFMO with moisture at low temperatures.

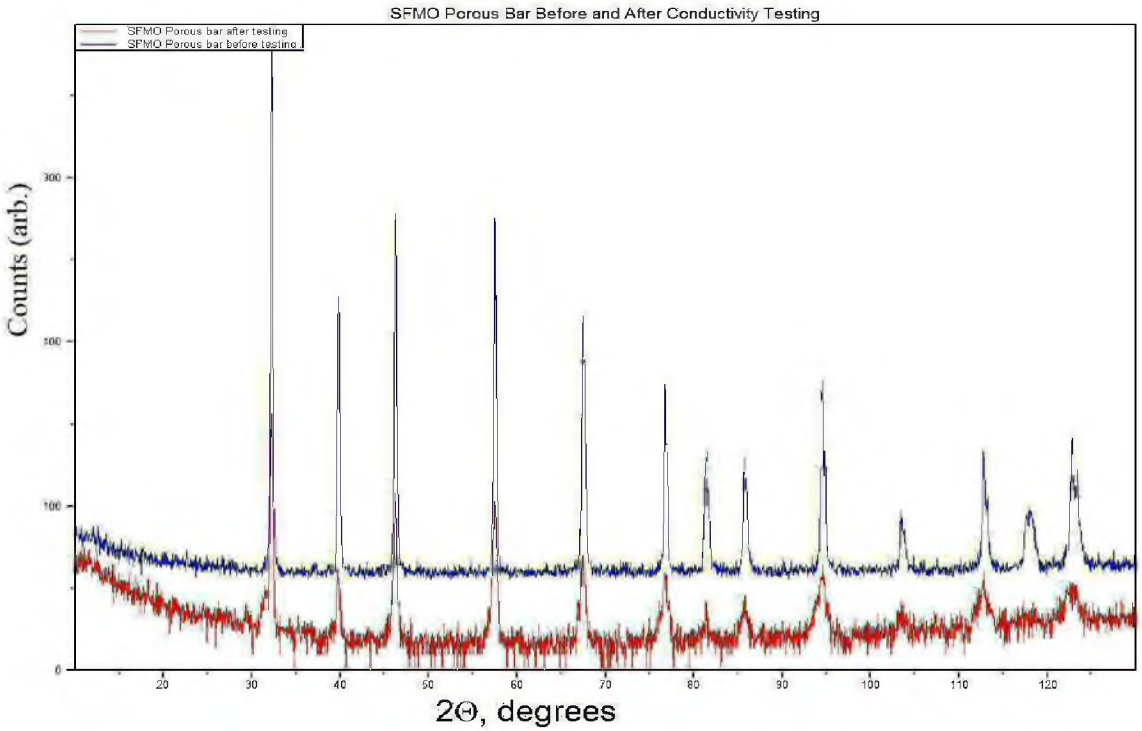

Figure 3.4: XRD traces of the as-fabricated porous SFMO sample after several conductivity measurements. The traces appear to be very similar. Small amounts of reaction products, such as $Sr(OH)_2$, cannot be detected by XRD. However, they do affect the conductivity.

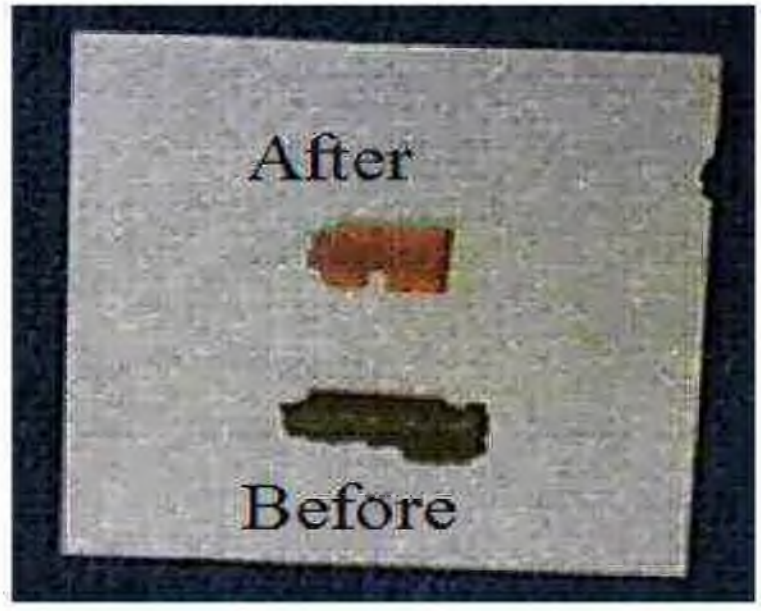

Figure 3.5: A photograph of the two halves of the same sample before and after boiling in water for ~20 minutes. After boiling, the color changed from black to brick red. Sample broke into many pieces during boiling.

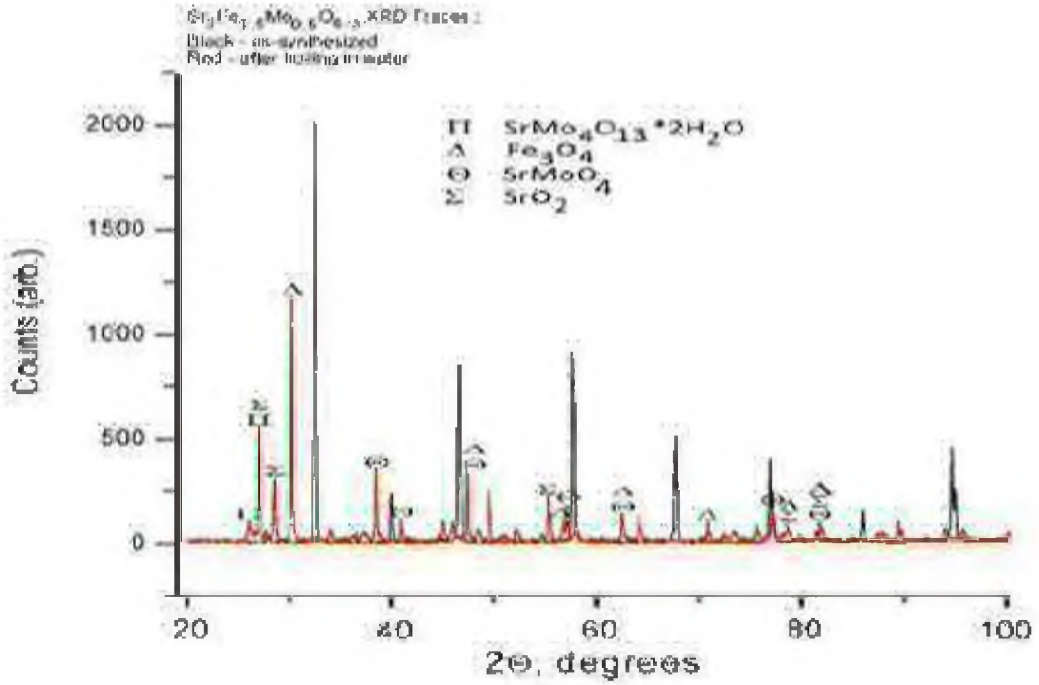

Figure 3.6: XRD traces of the $Sr_2Fe_{1.5}Mo_{0.5}O_6$ (SFMO) sample before and after boiling in distilled water. Note that boiling in water completely destroyed the original structure and led to the formation of $Sr(OH)_2$ and other oxides / hydroxides.

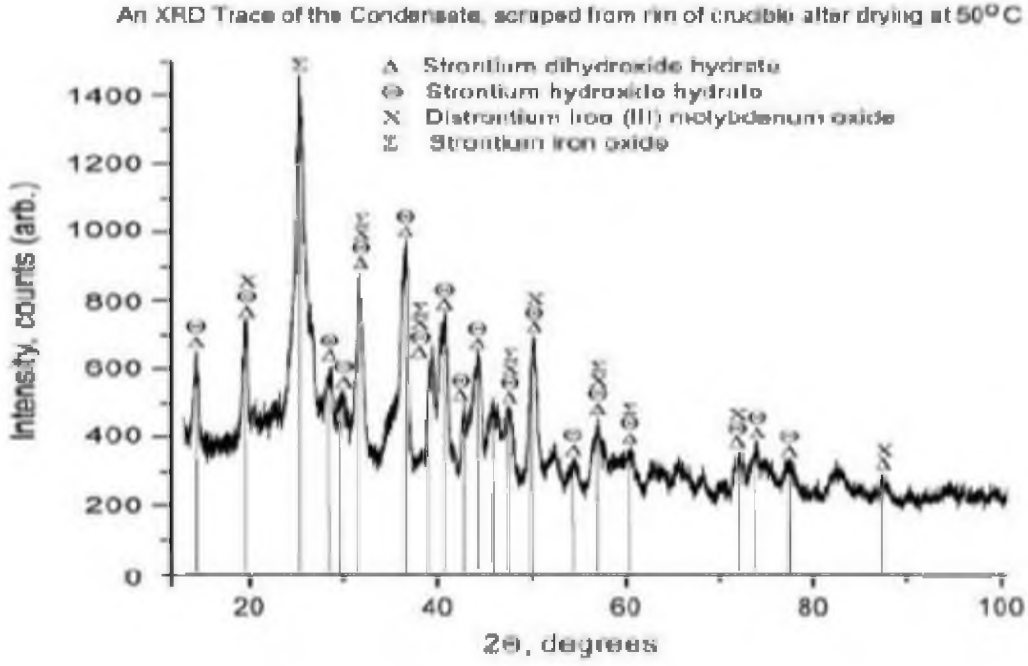

Figure 3.7: An XRD trace of the condensate from the rim of the crucible after drying in air at 50 °C. The trace corresponds to a number of Sr-containing hydroxides.

CHAPTER 4

INSTABILITY AND DEGRADATION OF $Sr_2Fe_{1.5}Mo_{0.5}O_{6-\delta}$ IN OXIDIZING AND REDUCING ATMOSPHERES

4.1. Introduction

$Sr_2Fe_{1.5}Mo_{0.5}O_{6-\delta}$ (SFMO) has a double-perovskite structure with alternating tetrahedra of Fe and Mo oxides, combined with interstitial strontium ions at coordination sites. The presence of the alkaline earth strontium leads to instability in water-containing atmospheres, especially at low temperatures. Long-term instability under water exposure suggests immense challenges in adapting SFMO for SOFC use [1].

In order to investigate whether additions or other substitutions might improve the properties of SFMO sufficiently to allow SOFC use, it is necessary to investigate the nature of degradation that takes place, and into what decay products it decomposes. The composition of the decay products may suggest routes of attack from the imposed atmospheres, and what strategies might be pursued to reduce or eliminate decay of the parent compound SFMO.

Our earlier work focused on water attack and decomposition, so this suggested an approach of beginning with dry atmospheres, gradually increasing the humidity, and analyzing for decay products as the humidity is increased. For a baseline, we began with dry air and dry ultra-high-purity hydrogen, to establish the instability of SFMO in those conditions as suggested by earlier studies [2,3,4].

The literature describes how SFMO is only stable in a narrow pO_2 window, between ($-9.8 \geq \log pO_2 \geq -13.5$) in one study [4]. The authors described the decay compounds formed under hydrogen attack as $SrO + Mo + Fe_3Mo_2$, while the decay under air attack produced $SrMoO_4 + SrFeO_{3-\delta}$ [4]. Another study reports that at 1200 °C in 1% H_2 / Ar, Sr_2FeMoO_6 is not a unique line compound, but rather a composition formed by the solution of Mo in $SrFeO_{3-\delta}$[5]. This means that Sr_2FeMoO_6 is unstable in air (at 1200°

C), because there is insufficient solubility of Mo in $SrFeO_{3-\delta}$ under that atmosphere [5]. Another study examined the decay of SFMO in both reducing atmosphere (5% H_2 – 95% N_2) and air, finding it reduced to Sr_2FeMoO_4, $Sr_3Fe_2O_6$, and elemental Fe in the former, while in air it decayed into $Sr_2Fe_{2-x}Mo_xO_6$, $SrCO_3$, $SrMoO_4$, FeO, and $SrFeO_3$ [6]. In an attempt to create commercial devices using SFMO, another study documented the deterioration of SFMO in air at room temperature, but only mentioned the compound $SrMoO_4$ as a decay product [7]. A further study investigated the phase stability boundaries of SFMO and found that it oxidizes according to

$Sr_2FeMoO_6 + 1/4O_2 = SrMoO_4 + SrFeO_{2.5}$,

while it is reduced, resulting in Sr_3FeMoO_7 and Fe (no equation given) [8].

A comparison of the list of decay products between studies shows that there are some common results, but no general agreement on exact products from decay, either in hydrogen or in air. Even though the lists of decay products from SFMO decay may vary, however, the basic results on instability in both air and in hydrogen atmosphere, decay into other compounds, and subsequent loss of structure and functionality remain consistent between studies.

As a first step towards developing a stabilized form of SFMO for use in SOFCs, we wished to reconcile these varying results, and determine what decay compounds are formed and to what extent does SFMO decay in air and hydrogen. The initial objective was to use XRD to identify the compounds formed and EIS to determine how quickly they were formed.

4.2. Experimental Procedure

SFMO powder was prepared by a combustion synthesis method, as described previously [1]. A series of experiments were performed after the as-received powder was characterized by XRD using CuKα radiation (see Figure 4.1). The as-received powder is an excellent match for the library XRD pattern for $Sr_2Fe_{1.5}Mo_{0.5}O_{6-\delta}$. This powder was subdivided into samples and run through various heat treatments to investigate stability and reactions by XRD.

A sample of SFMO powder was placed in a crucible (Coorstek part no. 60036) and located in a long, closed-end ceramic furnace liner tube, the closed end of which was heated in the furnace and the open end quite distant from heat. The boat-shaped crucible has a tab on one end with a hole in it, which facilitates tying a wire through the hole. The open end of the tube was fitted with a rubber stopper, penetrated with pass-throughs for the atmosphere supply and vent, which also served to feed the end of the wire out to the lab. At temperatures above 800 ^{o}C, the crucible was unsuitable for heat treatments, and a zirconia plate was substituted to hold the powder. See Figure 4.2 for an illustration of the experimental setup.

During experimentation, ultra-high purity hydrogen or air from cylinder supply was passed into the furnace tube and circulated over the sample powder in the crucible boat. The temperature of the furnace was varied, and left to stabilize until the powder could equilibrate. Each temperature step was approximately 1 h in duration, since the powders were finely grained and could equilibrate quickly. When the maximum temperature was reached and equilibrated, the wire was pulled and the sample crucible moved from the hot zone of the furnace to the cold zone near the stopper, in a matter of a

few seconds. The powder then cooled quickly by radiation and convection until it reached the same temperature as the cold zone, about 25 °C. The atmosphere continued flowing until the sample cooled, and was shut off thereafter. The powder in the crucible was removed, placed in a glass vial, and XRD was performed on it. Sequential experiments were performed to evaluate regeneration, and a series of experiments run to evaluate the effect of temperature on the degree and level of decay under a given atmosphere.

A typical experiment involved weighing out 0.50 gram of SFMO powder and placing it in a crucible, tying on the wire, and pushing the crucible to the closed end of the furnace liner tube with a rod. The stopper was fitted tightly into place, and the gas supply connected to the end of the gas supply header (a ceramic tube that passed through the stopper and nearly to the closed end of the furnace liner tube). The gas supply was activated and the liner tube (and sample) were purged with the supplied gas. After the atmosphere was stabilized, the furnace was turned on and gradually raised (at approximately 200 °C per hour) to the target temperature. To ensure equilibration, the powder was left at the target temperature under supplied atmosphere for 1.5 h. Then, the wire was pulled until the crucible moved from the hot furnace zone to the cold end at laboratory temperature protruding far from the furnace, and left there to cool down (typically 0.5 h) under supplied atmosphere. Once the furnace itself cooled to room temperature, the sample was unloaded into a glass vial and taken for XRD analysis.

Another set of experiments involved EIS measurement, carried out as follows: wafers of samarium-doped ceria (SDC, $Sm_{0.2}Ce_{0.8}O_{2-\delta}$, Fuel Cell Materials) were pressed in a uniaxial press using stainless steel dies and sintered at 1600 °C for 3 h to ensure high density. The resulting wafers were approximately 1.25 mm thick and 2.75 cm in

diameter. These dense SDC wafers were coated on each side to create layered SFMO / SOFC / SFMO discs. Since the literature [9] suggests that SFMO serves effectively as both anode and cathode, both sides of the SDC (electrolyte) wafer were coated with SFMO. First, SFMO was sonicated in isopropanol and spin-coated on the SDC disc dropwise before drying at 80 °C and firing at 1100 °C in air in a box furnace to stabilize the SFMO on the SDC surfaces. EIS measurements were made at various temperatures in air and in ultra-high-purity hydrogen using Ag mesh contacts. Later, the discs were coated with silver paste as current collector layers (Hereaus C8728 Ag conductor paste, diluted 1:3 with Fisher α-terpineol, and fired at 600 °C in air in the box furnace), and EIS measurements were made after the silver paste was applied and fired. The SFMO and silver paste electrodes were approximately 1.95 cm in diameter. The SFMO / SDC / SFMO layered discs were placed in a Barnstead Thermolyne 21100 tube furnace and heated under supplied atmosphere while ceramic spacers under (external) spring pressure applied force to hold the silver gauze current collectors tightly against the disc surfaces on either side. The ends of the furnace tube were fitted with rubber stoppers, which were equipped with feed-through tubes for gas supply and venting, electrical wires, and a thermocouple (Omega Engineering Type K, part number CHAL-020). Cylinder gases of ultra-high purity hydrogen and compressed air were used to vary the atmosphere inside the furnace. See Figure 4.3 for a diagram of the EIS experimental setup.

The Solartron 1260 and 1287 apparatus is commonly used and will not be described here; the resulting data files were graphed using OriginLab's Origin 7 software, after converting the data files to the usual Z Real, -Z Imaginary format. The Solartron 1287 / 1260 instruments provided low-voltage alternating current of variable frequency

across the SFMO / SDC / SFMO layered discs, while measuring the impedance of the sample. The temperature inside the furnace was generally changed in 200 degree steps once an h, and EIS measurements were taken at each step.

4.3. Discussion and Results

As mentioned above, Sr_2FeMoO_6 may be considered as a composition formed by the solution of MoO_3 or MoO_4 in $SrFeO_{3-\delta}$. Further, the Sr_2FeMoO_6 compound is unstable in air at room temperature [7]; therefore, unless it is stored under an atmosphere with compatible pO_2 content, Sr_2FeMoO_6 *continually decays towards a different composition* from the time it is made until it reaches equilibrium with the imposed temperature and atmosphere (or is completely destroyed). It will likely decompose less quickly at room temperature with water than at higher temperature, but over time it will certainly deteriorate at 25 ^oC as well [6,7]. To investigate this, the XRD data for the as-received powder were compared with those obtained after various heat treatments under two imposed atmospheres, air and ultra-high purity hydrogen. It is apparent from examination that the spectra are not identical nor closely related, after extended heat treatment in hydrogen atmosphere. This demonstrates that physical and chemical changes occurred in SFMO under the test conditions. Table 4.1 lists the various experiments performed in this study.

Figure 4.4 show the changes observed in XRD spectra when the initial powder was first placed under ultra-high purity hydrogen atmosphere at 800 ^oC for approximately 1.5 h, then quickly pulled from the hot zone in the furnace to the cold end of the furnace liner tube, where it cooled quickly towards room temperature. It is apparent that the

initial SFMO powder has decomposed; the major peak at 32° 2Θ has nearly disappeared, while multiple minor peaks have appeared at 17°, 26°, 28°, 29°, 30°, 33°, 44°, 50 – 53°, and elsewhere. These minor peaks can only be the result of decay of SFMO into other compounds, demonstrating the instability of SFMO under ultra-high-purity hydrogen atmosphere. Software analysis identifies the decay compounds present as Fe, Sr_3 Fe MoO_7, Sr_3 Fe_2 $(OH)_{12}$, and $SrMoO_4$, and the heat-treated powder sample was magnetic. The presence of the compound [$SrMoO_4$] suggests that an early step in decay is removing oxygen from the double perovskite compound, while the presence of the hydroxyl compound suggests that water attack is also occurring. The lack of mention of hydroxyl decay products in the literature is possibly due to complete decay of SFMO in previous studies; in TGA analysis, for instance, completion is attained when weight loss ceases, which would require total decay of SFMO in hydrogen. Since the hydroxyl compounds are either volatile or would decay further in pure hydrogen (Sr_3 Fe_2 $(O H)_{12}$), they would not be seen in analysis after a TGA experiment.

An attempt to regenerate the original SFMO by placing part of this sample under air at 800° C for 1.5 h, followed by another pull to the cold zone, was limitedly successful; some SFMO formed. However, the reaction was incomplete, possibly due to slow kinetics. While many of the peaks generated under ultra-high-purity hydrogen disappeared, new peaks formed under air at 52°, 73°, and 98° 2Θ that were not present in the original SFMO powder XRD spectrum or the initial hydrogen treatment spectrum (see Figure 4.5). It therefore appears that new decay compounds were generated under air that were not present after the original ultra-high-purity hydrogen treatment. XRD software analysis identifies these compounds as $SrMoO_4$ and SrFe $O_{2.80}$.

Another experiment involved taking a sample of the original powder and placing it under ultra-high purity hydrogen at 800 °C for 1.5 h, then slowly cooling it (still inside the furnace) by turning down the temperature while the powder remained under hydrogen. This also created decay compounds, but different ones from those formed by the fast pull to the cold zone. Figure 4.6 documents the XRD results of this experiment, which feature Sr_3FeMoO_7, SrO, $Fe_{9.7}$ $Mo_{0.3}$, Fe_3O_4 and Fe as decay products. To see if regeneration under hydrogen was feasible, part of this sample was placed under ultra-high purity hydrogen at 600° C for 4 h, and analysed by XRD. The results are seen in Figure 4.7, and the new identified products are $Sr(OH)_2*H_2O$, $Sr_2Fe_2O_5$, $Fe_{9.7}Mo_{0.3}$, and $FeMoO_4$.

Figure 4.8 is a comparison between the products in Figure 4.4 and Figure 4.6. This is an 800 °C exposure to ultra-high purity hydrogen for 1.5 h, ending in either a quick pull (Sample SFMOH2HT) or cooling slowly under hydrogen (Sample SFMOH2CS). The results are not the same, although there are several peaks (such as Fe and Sr_3FeMoO_7) that are common between them. However, when examining the peaks between 25° and 30° 2Θ, in the blue ($SFMOH_2HT$), there are three sharp peaks; in the red ($SFMOH_2CS$), there is one broad peak with a shoulder and one small sharp peak. Another such example is between 65° and 70° 2Θ. Comparing the experimental conditions, cooling slowly under ultra-high purity H_2 has resulted in different compounds, in contrast with a quick pull to the cool zone. The SFMO powder has continued to react below 800 °C, as it cooled slowly under ultra-high purity H_2 to room temperature over several h.

In another experiment, the original SFMO powder was heated to 1000 °C under ultra-high purity hydrogen for 1.5 h and then quickly pulled to the cold zone. Fewer

decay products were formed, but these were yet another set of compounds. Figure 4.9 documents the XRD results of this experiment, and the decay products are identified as Fe, SrO, $Sr(OH)_2$, and $FeMoO_4$. Reduced iron (and magnetism) are repeatedly observed (Figures 4.4, 4.6, and 4.9) under the action of ultra-high-purity hydrogen on SFMO. SrO and $Sr(OH)_2$ were not present in the original powder, which almost totally disappeared.

A repeat of that experiment was performed at 1200 ^oC in ultra-high-purity hydrogen for 1 h. Two versions were performed; in one, the powder was pulled to the cold zone after 1 h, quickly cooled and removed. In the next, the powder was left in the furnace to cool slowly under ultra-high-purity H_2 over several h before removal. The results are seen in Figure 4.10. The same approximate decay products are seen in both samples; elemental Fe and $SrMoO_4$ are seen in both. The slowly cooled sample has more $SrMoO_4$, and $SrFeO_{1.8}$ as well. It is possible to see, comparing the traces, that the original SMFO peak at 32^o 2Θ shrinks from the original powder to the sample quickly pulled to the cold zone after 1 h at 1200 ^oC, and disappears completely from the sample cooled slowly under ultra-high-purity H_2 from 1200 ^oC to room temperature. Likewise, the Fe peak at 44.6^o 2Θ is totally absent from the original powder, reaches a middle level in the (blue) quickly pulled sample, and finally a high level in the (green) slowly cooled sample.

The XRD results from air experiments are less informative. The literature mentions decay in air above 400^o C, but does not give firm indications of kinetics; longer timespans than investigated here (above 2 h at 800 ^oC, or above 4 h at 600 ^oC) are required to generate significant degradation in air atmosphere. Figure 4.11 illustrates the results of the experimental runs in air, and there is little difference here between the original powder and the air atmosphere test samples by XRD.

EIS is a technique that is frequently used to examine transient phenomena, such as corrosion, chemical reaction, and oxidation; however, in order to obtain repeatable and mathematically tractable results, the attempt is usually made to attain some form of steady-state operation. A chemical reaction, for example, might be studied using a large reservoir of fluid, so that reactants are not significantly depleted while the experiment progresses. The SFMO films studied by EIS here are only a few microns in thickness, and not of a large area (less than 3 cm^2); it appears that the EIS results change as time and temperature and applied atmosphere decay the SFMO layers.

The EIS results obtained here are also instructive. Figure 4.12 is an EIS trace at 180 ^oC of a new SFMO / SDC / SFMO layered disc in hydrogen; multiple depressed-semicircles are evident, and starting from the left can be assigned to SDC bulk impedance, SDC grain-boundary impedance, and SFMO impedance. It is recognized that SOFCs do not operate at 180 ^oC, but this figure is only intended to establish the pattern expected from such a layered disc; three depressed-semicircular arcs, end to end, stretching from the highest frequencies to the lowest (left to right). Also, separate arcs are easier to see at low temperatures; as the temperature rises, the arcs merge and condense, such that at 800 ^oC only one arc might be seen, with inflexion points.

As evidence of the decay mentioned, these SFMO / SDC / SFMO layered discs were made repeatedly, and examined by EIS. Typically, a sequence would be observed; in air, the three depressed-semicircular arcs would be seen at 200 ^oC, merging towards one as the temperature rose. A typical EIS trace in air at 800 ^oC is shown in Figure 4.13. However, not every disc lasted long enough to give a coherent trace at 800 ^oC; if the sample failed, the smooth arcs in Figure 4.13 would be replaced by jagged, unpredictable

traces, and the experiment ended. In hydrogen, much the same result was produced.

A sample was prepared, and examined initially by EIS. Multiple EIS runs produced the results shown in Figure 4.14. These results were obtained in a period of just over 30 minutes. Note the common shape but wide distribution of resistances seen at 800 ^{o}C in air. There should not be such a difference (several ohms) at the same temperature, pressure, and atmosphere for one sample. One possible explanation is that the various traces document the change in impedance due to decay as it progresses.

SOFCs usually have current collector layers in addition to the required anode, electrolyte, and cathode layers. Since SFMO is used here for both the anode and cathode layers, silver paste was applied for current collector layers and fired to stabilize it on the SFMO surfaces. EIS measurements taken after silver application are considerably different; the EIS traces in air at 800 ^{o}C are nearly perfect duplicates (see Figure 4.15). The reason for this is not that silver stabilizes SFMO; instead, it creates a composite electrode layer consisting of SFMO (an MIEC, with moderate ionic conductivity and reasonable electronic conductivity) and silver (a metal with excellent electronic conductivity). Once the silver paste is applied and fired, EIS measurements no longer reveal the properties of SFMO alone. This highlights a technique issue in EIS measurement: one cannot investigate a porous electrode layer once a conductive (metal) layer has been applied over it. To investigate the response of porous electrode layers, the mesh EIS electrode (silver mesh in Figure 4.3) must be held against the porous electrode layer without additional metal surface layers in use. Similar results were obtained using Pt paste as well (not shown).

Given the multiple decay routes and necessity of exposure to imposed

atmospheres, SFMO is not a good candidate for SOFC service. To be successful, coatings would be required to totally isolate the SFMO from both air and pure hydrogen atmospheres, rendering the SFMO layers unusable. Additives that might stabilize SFMO in service are possible, but would be challenging to determine, likely requiring different additives in anode and cathode service.

One additional possibility would be to control the pO_2 of the imposed atmospheres; if the cathode supply were limited to log $pO_2 < 10^{-9}$, then SFMO could be stable as a cathode. Similarly, if the anode supply gas were limited to log $pO_2 > 10^{-13}$, then the SFMO could be stable as an anode. Whether such an SOFC would deliver sufficient power to make it worthwhile to manufacture is questionable. The need to move oxygen at a low absolute concentration from cathode through the electrolyte to the anode means we would have to process twenty-two million cubic meters of log $pO_2 = 10^{-9}$ gas mixture to transfer ¼ mole of oxygen and move 1 Faraday of charge through the external circuit.

4.4. Summary

The compound SFMO is a highly complex double-perovskite of varying composition depending on the stoichiometric ratio of the starting materials. Various compositions can be accommodated by disorder in the alternating Fe and Mo oxide tetrahedrons, oxygen vacancies, and similar defects. The compound is unstable in air or hydrogen over time at elevated temperatures, leading to total decay and breakdown. It suffers from different routes of attack, depending on whether oxygen or hydrogen is present, and water forms as it decays in hydrogen, providing another attack route.

The various decay decay products have been investigated by XRD, and depending on whether the decay is partial or total, different decay products will be found. Early and partial decay in hydrogen leads to strontium and iron hydroxyl compounds (partially due to water attack), while decay in air takes higher temperatures and longer times than performed in this study.

EIS studies found irregular results, due to the changing composition of the SFMO samples as they decay over time.

Given that SFMO experiences multiple attacks from oxygen, hydrogen, and water (all of which are present in SOFC service), it is doubtful that a single coating could protect SFMO in both anode and cathode service.

4.5 Acknowledgements

This material is based upon work supported as part of the HeteroFoaMCenter, an Energy Frontiers Research Center funded by the U.S. Department of Energy, Office of Science, Office of Basic Energy Sciences under Award Number DE-SC0001061

4.6 References

1) J. H. Wright, A. V. Virkar, Q. Liu, F. Chen, "Electrical characterization and water sensitivity of $Sr_2Fe_{1.5}Mo_{0.5}O_{6-d}$ as a possible solid oxide fuel cell electrode," J. Power Sources 237 (2013) 13-18

2) J. Navarro, C. Frontera, D. Rubi, N. Mestres, J. Fontcuberta, "Aging of Sr_2FeMoO_6 and related oxides," Mat. Res. Bull. 38 (2003) 1477–1486

3) L. H. Son, N. X. Phuc, P. V. Phuc, N. M. Hong, L. V. Hong, "Observation of phase decomposition of $Sr2FeMoO_6$ by Raman spectroscopy," J. Raman Spectrosc. 32 (2001) 817–820

4) T. Nakamura, K. Kunihara, Y. Hirose, "Stable pO_2-region of ordered perovskites Ca_2FeMoO_6 and Sr_2FeMoO_6 at 1200° C," Mat. Res. Bull. 16 (1981) 321- 326.

5) J. Rager, M. Zipperle, A. Sharma, J. L. MacManus-Driscoll, "Oxygen stoichiometry in Sr_2FeMoO_6, the determination of Fe and Mo valence states, and the chemical phase diagram of SrO-Fe_3O_4-MoO_3," J. Am. Ceram. Soc. 87 (7) (2004) 1330-1335

6) T. Fan, T. Ko, "Factors affecting the preparation of $Sr_2Fe_{2-x}Mo_xO_6$," J. Am. Ceram. Soc, 86 (9) (2003) 1453–55

7) J. Fontcuberta, L. Balcells, J. Navarro, D. Rubi, B. Martínez, C. Frontera, J. L. García-Muñoz, M. Lacaba, A. M. González, C. Forniés, A. Calleja, L. L. Aragonès, "Magnetoresistive ceramics: Recent progress from basic understanding to applications," Bol. Soc. Esp. Ceram. V., 43 (3) (2004) 627-633

8) R. Kircheisen, J.Topfer, "Nonstoichiometry, point defects and magnetic properties in Sr_2FeMoO_{6-d} double perovskites," J. Solid State Chemistry 185 (2012) 76–81

9) Q. Liu, X. Dong, G. Xiao, F. Zhao, F. Chen, "A novel electrode material for symmetrical SOFCs," Adv. Mater. 22 (2010) 5478–5482

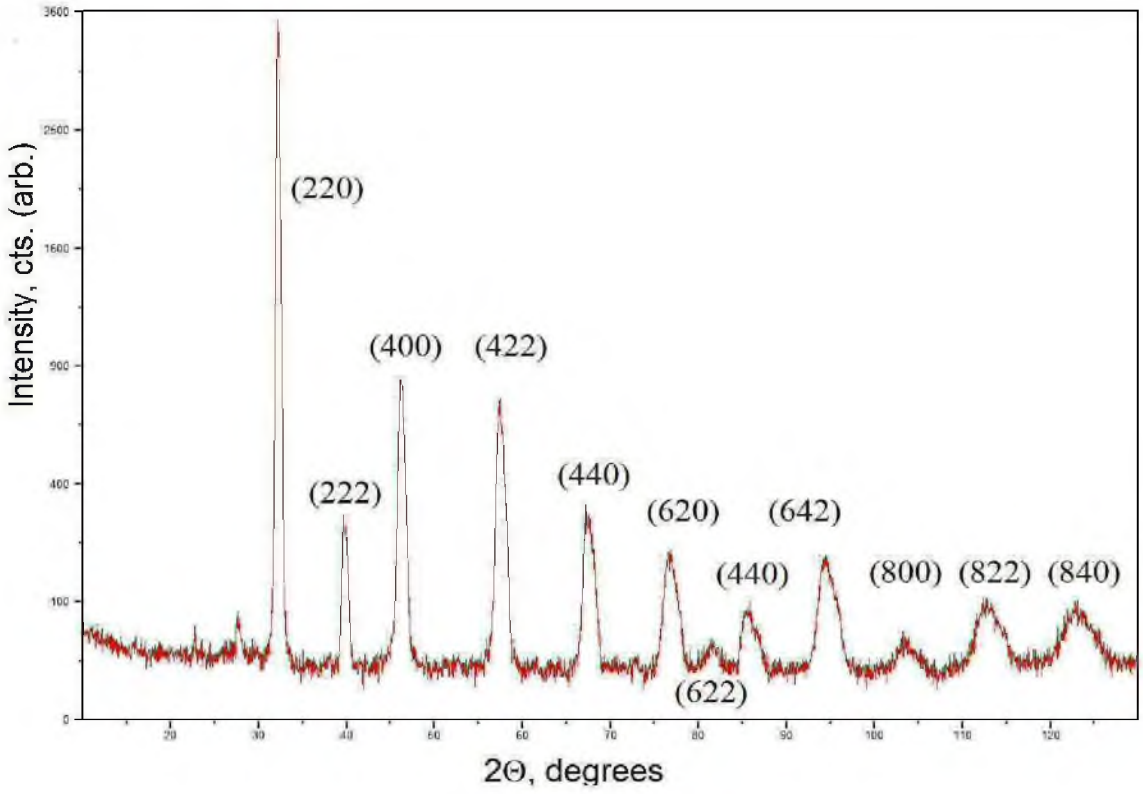

Figure 4.1. XRD trace of original powder, $Sr_2Fe_{1.5}Mo_{0.5}O_{6-\delta}$

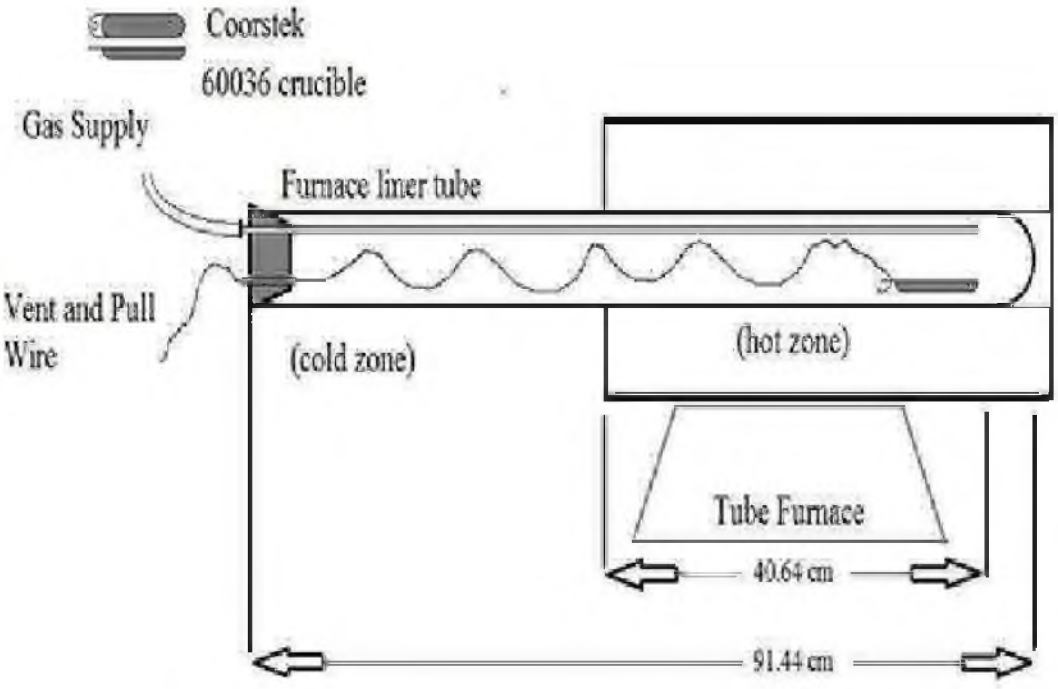

Figure 4.2 Experimental setup for powder heat treatments

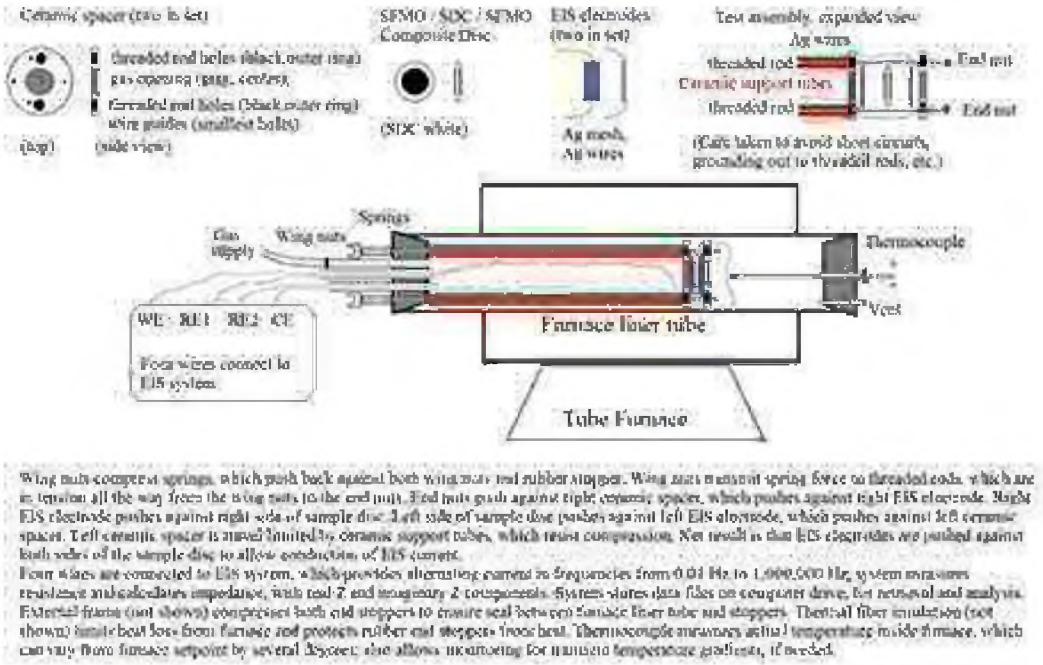

Wing nuts compress springs, which push back against both wing nuts and rubber stopper. Wing nuts transmit spring force to threaded rods, which are in tension all the way from the wing nuts to the end nuts. End nuts push against right ceramic spacer, which pushes against right EIS electrode. Right EIS electrode pushes against right side of sample disc. Left side of sample disc pushes against left EIS electrode, which pushes against left ceramic spacer. Left ceramic spacer is stopped by ceramic support tubes, which resist compression. Net result is that EIS electrodes are pushed against both sides of the sample disc to allow conduction of EIS current.
Four wires are connected to EIS system, which provides alternating current in frequencies from 0.01 Hz to 1,000,000 Hz, system measures resistance and calculates impedance, with real Z and imaginary Z components. System stores data files on computer drive, for retrieval and analysis. External frame (not shown) compresses both end stoppers to ensure seal between furnace liner tube and stoppers. Thermal fiber insulation (not shown) limits heat loss from furnace and protects rubber end stoppers from heat. Thermocouple measures actual temperature inside furnace, which can vary from furnace setpoint by several degrees; also allows monitoring for transient temperature gradients, if needed.

Figure 4.3 Test apparatus for EIS measurements on disc samples

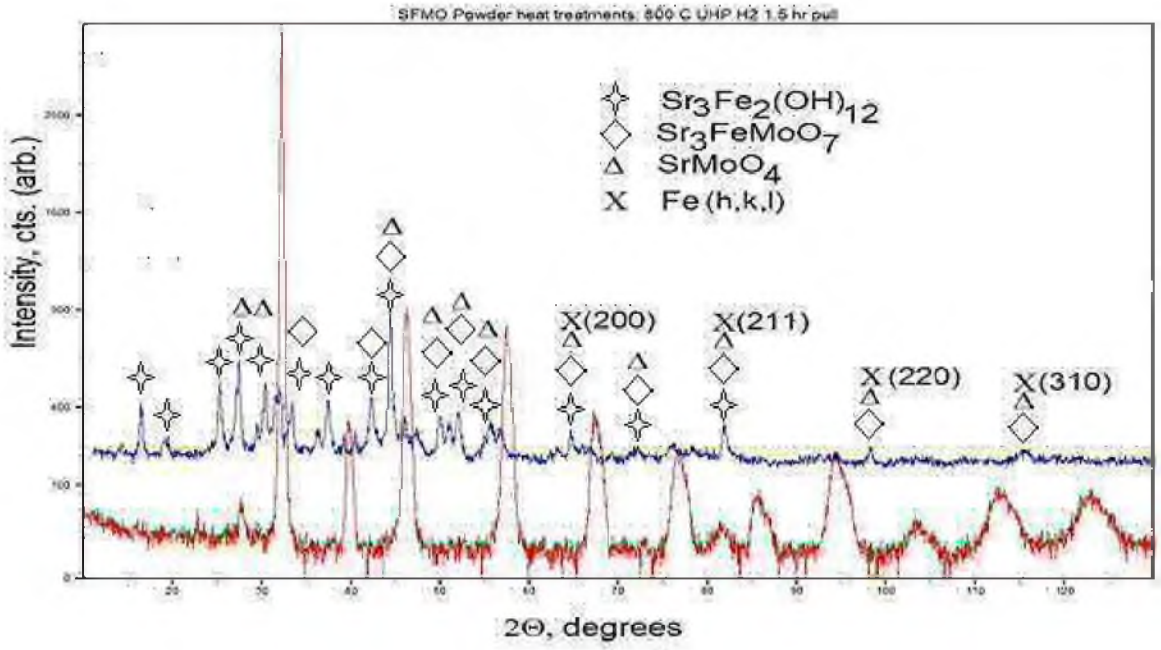

Figure 4.4 XRD trace of SFMO powder before and after heat treatment at 800° C in ultra-high-purity H_2 and quickly pulled into the cold zone (red trace is before treatment, blue is Sample SFMOH2HT, symbols apply to blue peaks)

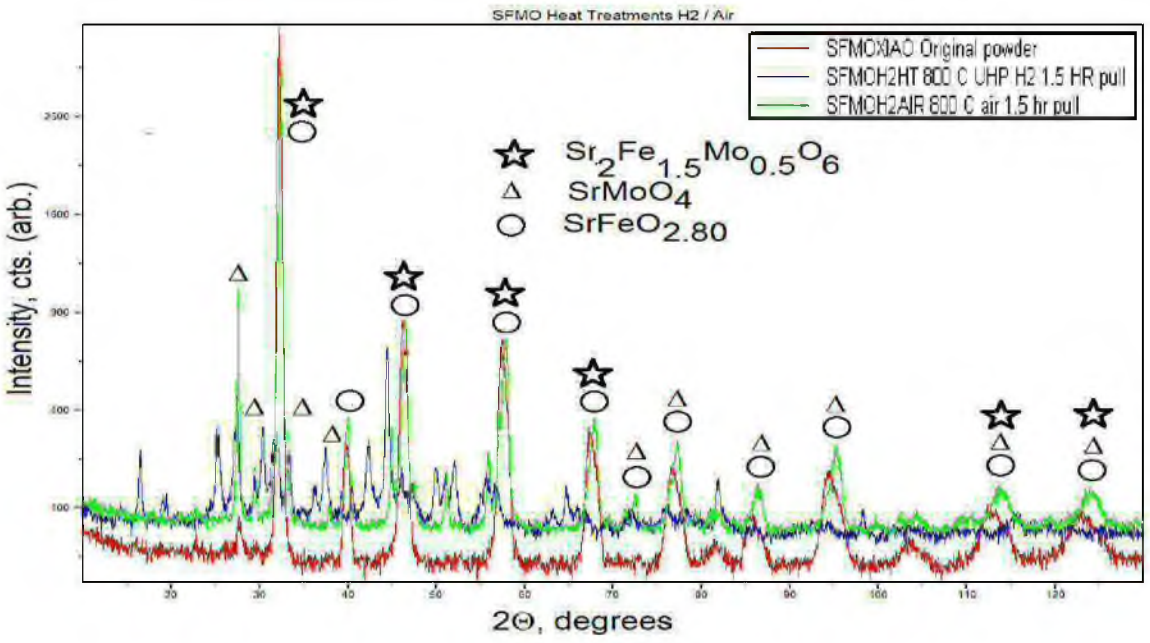

Figure 4.5. SFMO powder heat treatments: (red) original powder, then (blue) 800° C ultra-high-purity H_2 1.5 h pull to cold zone, then (green) 800° C air 1.5 h pull to cold zone (Adding Sample SFMOH2Air, symbols apply to green peaks)

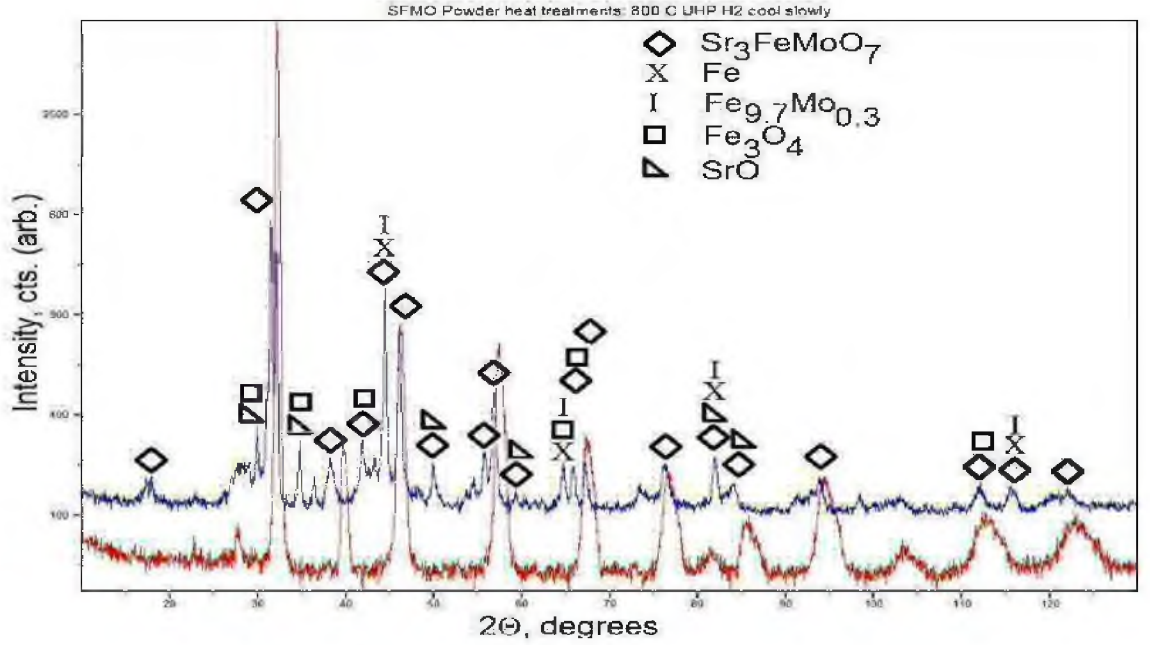

Figure 4.6. SFMO powder heat treatments: original powder, then 800° C ultra-high-purity H_2 1.5 h, then cool slowly under ultra-high-purity H_2 (Sample SFMOH2CS, symbols apply to blue peaks)

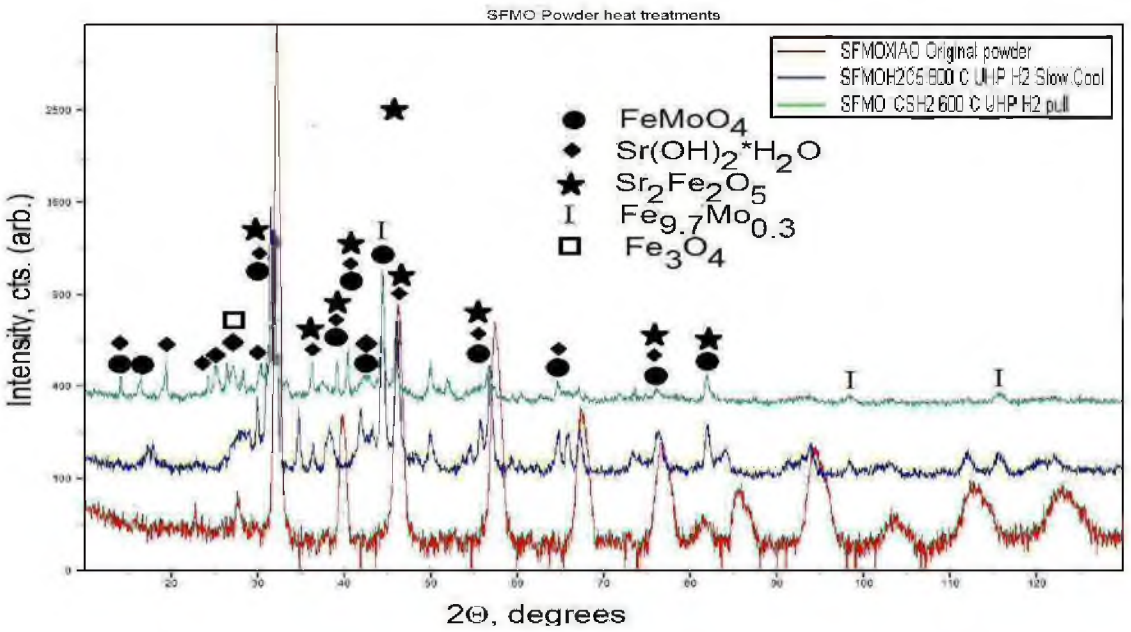

Figure 4.7. SFMO powder heat treatments: (red) original powder, then 800° C ultra-high-purity H_2 1.5 h cooled slowly under ultra-high-purity H_2 (blue), then 600° C ultra-high-purity H_2 4 h, pull to cold zone (green) (Adding Sample SFMOCSH2, symbols apply to green peaks)

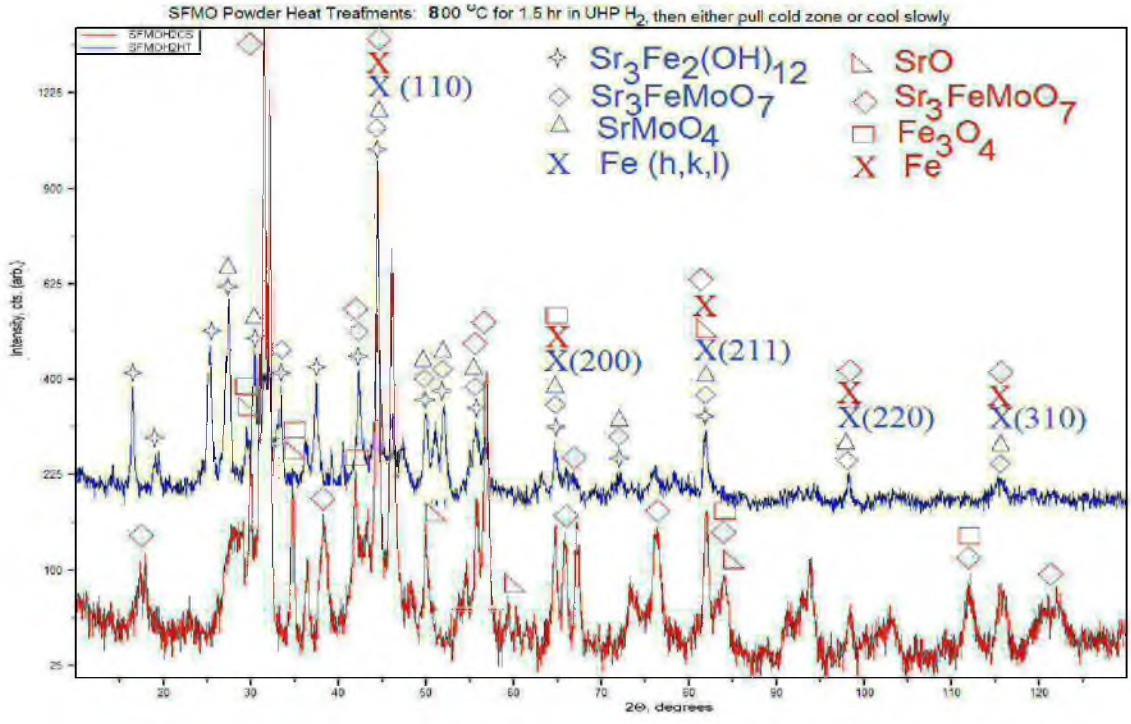

Figure 4.8. SFMO powder heat treatments: 800 °C under ultra-high-purity H_2 for 1.5 h, then either (blue) quick pull to cold zone, or (red) slow cooling under hydrogen. (Sample SFMOH2HT [blue] or SFMOH2CS [red])

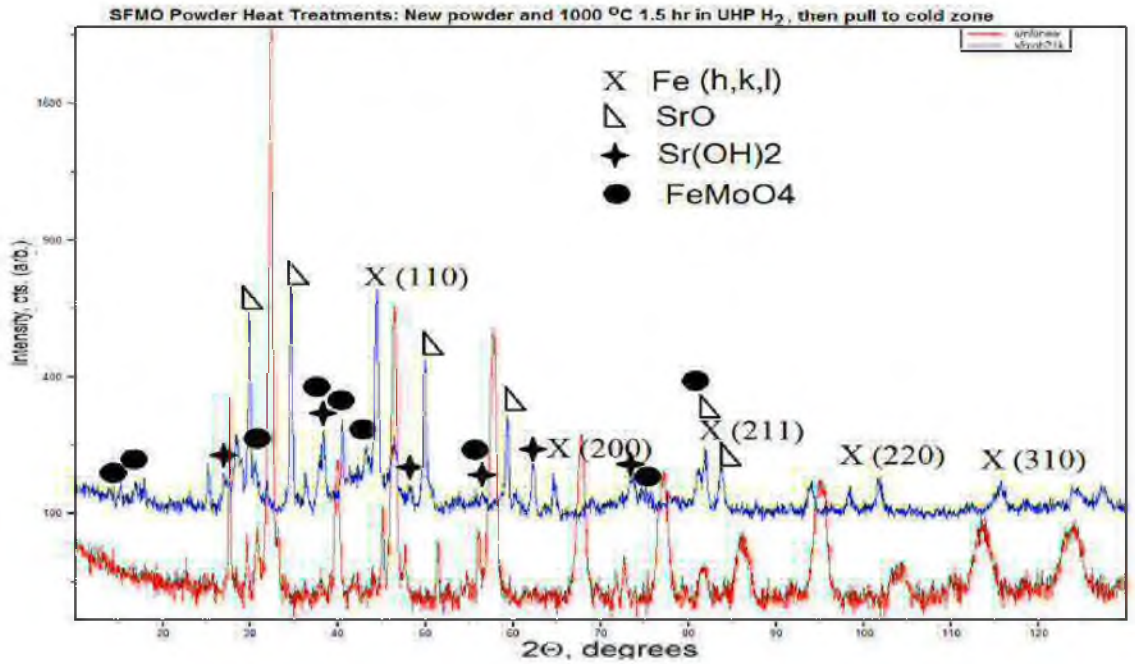

Figure 4.9. SFMO powder heat treatments: (red) original powder, then 1000 °C in ultra-high-purity H_2 for 1.5 h, then pull to cold zone (Sample SFMOH21K, symbols apply to blue peaks)

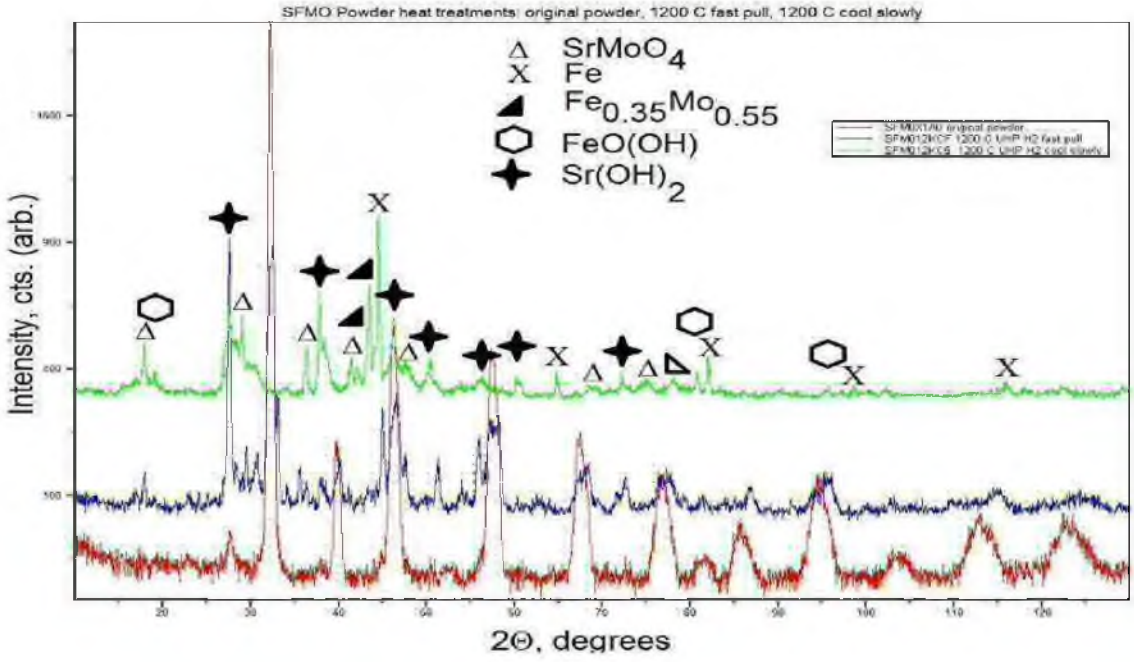

Figure 4.10. SFMO powder heat treatments: original (red), then 1200° C under ultra-high-purity H_2 for 1 h and quick pull to cold zone (blue). On another sample, 1200° C under ultra-high-purity H_2 for 1 h, then cool slowly under ultra-high-purity H_2 (green). (Samples SFMO12KCF, SFMO12KCS, symbols apply to green peaks)

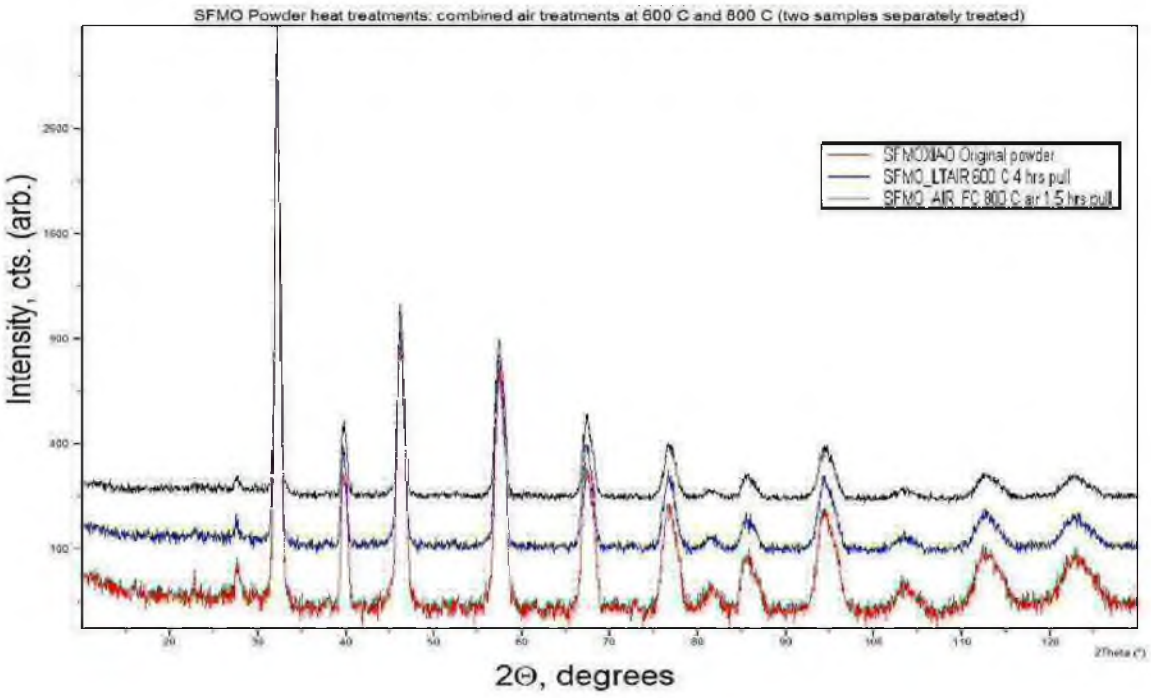

Figure 4.11. SFMO powder heat treatments: original powder, then 800° C in air 2 h, then pull to cold zone; on another sample, 600° C in air 4 h, then pull to cold zone (Samples SFMOLTAIR, SFMOAIRFC)

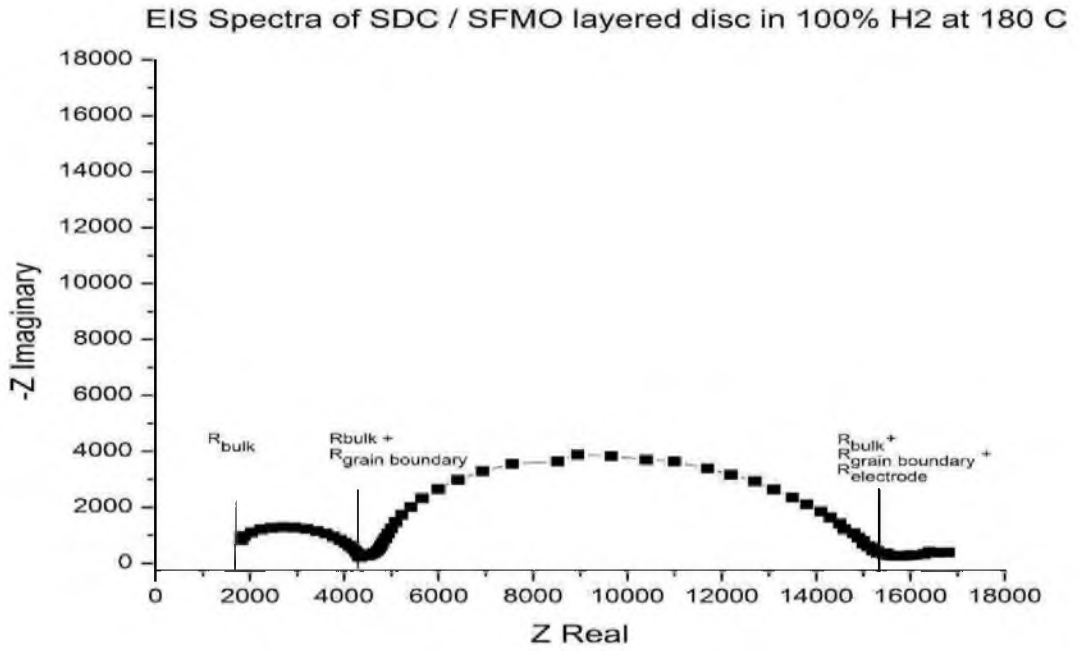

Figure 4.12. EIS trace of SFMO / SDC / SFMO layered disc in ultra-high-purity H_2 at 180° C ; angular frequency range 0.1 Hz to 1,000,000 Hz

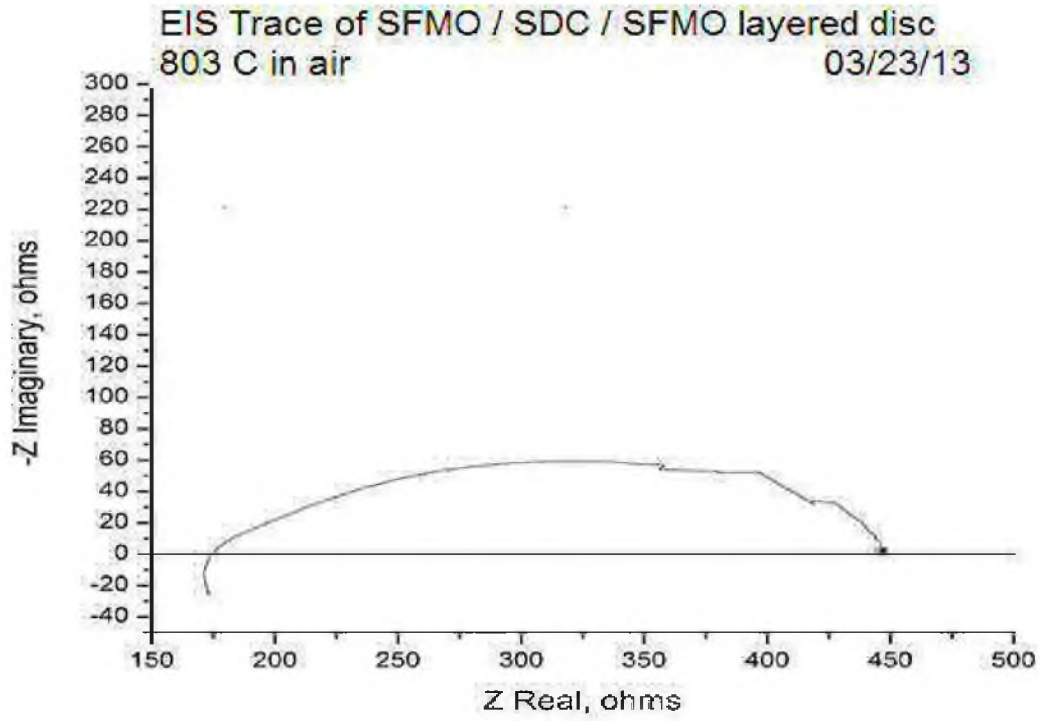

Figure 4.13. EIS trace of SFMO / SDC / SFMO layered disc in air at 800° C

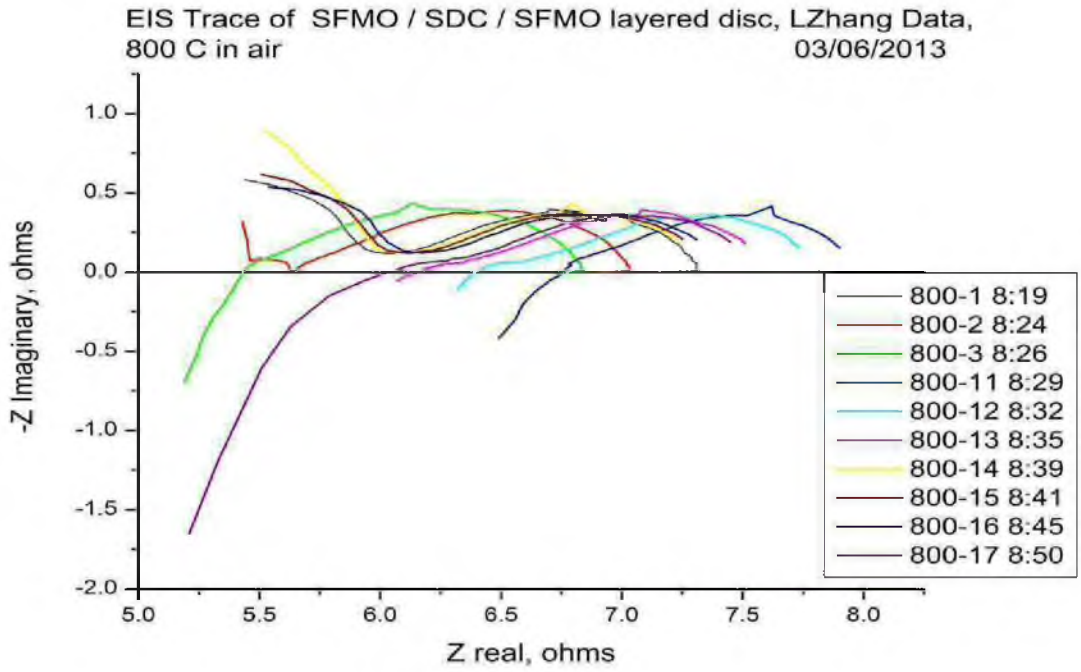

Figure 4.14. EIS traces of SFMO / SDC / SFMO layered discs in air at 800° C (one sample)

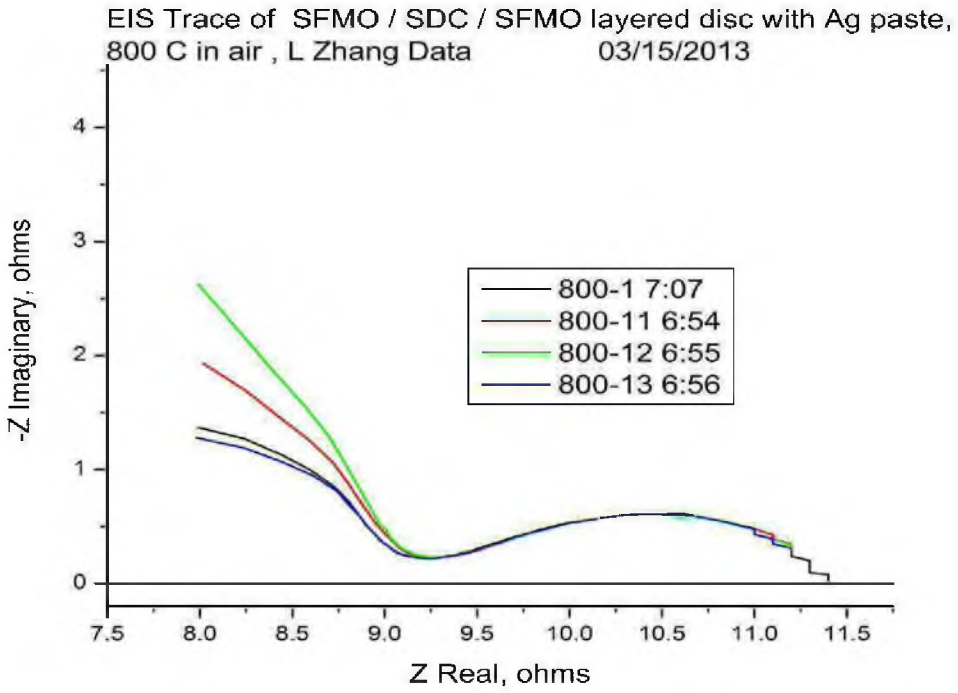

Figure 4.15. EIS traces of Ag / SFMO / SDC / SFMO / Ag layered discs in air at 800° C (one sample)

Table 4.1

Heat treatment experiments on SFMO powder
Sample SFMOX1A0
Original Source Powder
Made at 1000° C 5 hrs under air
Not magnetic
SUBSEQUENT HEAT TREATMENTS:

SFMOH21K 1000° C UHP H2 1.5 hr Pull to cold zone Magnetic	SFMOH$_2$CS 800° C UHP H_2 1.5 hr Cool slowly in H_2 Magnetic THEN: SMFOCSH$_2$ 600° C UHP H_2 4 hr Pull to cold zone Magnetic	SFMOH2HT 800° C UHP H_2 1.5 hr Pull to cold zone Magnetic THEN: SFMOH2Air 800° C air 1.5 hr Pull to cold zone Not Magnetic	SFMOAirFC 800° C air 2 hr Pull to cold zone Not magnetic	SFMOLtAir 600° C air 4 hr Pull to cold zone Not magnetic	SFMO12KCF 1200° C UHP H_2 1 hr Pull to cold zone Magnetic	SFMO12KCS 1200° C UHP H_2 1 hr Cool slowly under H_2 Magnetic

CHAPTER 5

COMBUSTION SYNTHESIS OF NANOSIZED SAMARIUM-DOPED CERIA

5.1 Introduction

When fabricating improved solid oxide fuel cells, materials with nanocrystalline features are used to develop improved or unique properties. Properties such as higher catalytic activity, better sinterability, and improved ionic and electronic conductivity are expected from the use of materials with smaller grain sizes, larger surface area, and higher surface energies.

CeO_2 is being investigated in various applications, such as catalysts, gas sensors, and oxygen purification [1]. Samarium-doped ceria (SDC) is considered for electrolyte service in solid oxide fuel cells, since it provides higher oxygen ionic conductivity at intermediate temperatures (500^o C – 800^o C). C. Nanosized powders have been synthesized by different techniques, such as molecular decomposition [2], hydrothermal methods [3], precipitation [4], and combustion [5]. The power characteristics, such as crystallite size, surface area, and phase content, were found to depend strongly on the fuel content in the starting mixture [5]. Basu [6] surveyed and found ceria powders prepared by hydrothermal synthesis, mimic alkoxide method, microemulsion method, sol-gel technique, precipitation method, glycine-nitrate combustion technique, hydrazine method, and spray hydrolysis, before going on to prepare 20-40 nm powder using a citrate-nitrate combustion method. For comparison, Litzelman [7] prepared dense ceria films by pulsed-laser deposition, and found grain sizes of 25 – 40 nm. The combustion synthesis methods can create powders of much smaller grain size (<10 nm).

D-gluconic acid (DGA) has a carboxylic acid group at one end and can effectively complex metal ions of varying ionic sizes, which helps to achieve homogeneous composition in solution. At the same time, DGA serves as fuel in combustion synthesis

reactions.

A method based on combustion synthesis for preparing nanocrystalline powders was investigated in this study. The route consisted of the gelling of metal nitrate solutions by the addition of DGA, followed by an intense combustion process due to an exothermic redox reaction between metal nitrate D-gluconic ions. An earlier-described combustion method using glycine as fuel to synthesize ceria compounds [5] was modified in the present study by replacing glycine with more-controllable and less-expensive fuels like DGA.

The effect of starting fuel / nitrate precursor ratio was investigated. The resulting crystallite size and powder surface area were determined, with smaller crystallites and higher surface areas being desirable. The powders were pressed into disc shaped samples, which were investigated in fuel cell service as a performance measure.

5.2 Experimental Procedures

The precursor metal salts were cerium nitrate ($Ce(NO_3)_3*6H_2O$, Alfa Aesar) and samarium nitrate ($Sm(NO_3)_3*6H_2O$, Aldrich). An organic fuel, DGA [$C_6H_{12}O_{17}$] was added in amounts to correspond to a desired ratio on the weight basis of fuel to nitrate salts. Typically, 250 ml of deionized water was used to dissolve the combined nitrate salts and fuel into a transparent aqueous solution. These were mixed and stirred in a stainless steel beaker which was wrapped in thermal insulation; Figure 5.1 shows the overall arrangement. The solutions were evaporated to dryness; the liquid mixture becomes viscous, puffs up with liberated gases (mostly water and nitric oxide / nitric acid), and autonomously ignites. The temperature is monitored with a thermocouple, and

the reaction observed through a mirror. The beaker is transferred to a box furnace, where the temperature is gradually raised to 250 ^{o}C for 4 h (to burn off any residual fuel and byproducts) and ground with a mortar and pestle. The product powder is then ready for characterization or use.

5.2.1 Characterization

The as-synthesized powders were characterized by X-ray diffraction (XRD), BET specific surface area measurement, and TEM. The crystallite size was determined by means of the X-ray line broadening method using the Scherrer equation [8];

$$D = 0.9\lambda / B \cos \Theta \qquad (5.1)$$

where D is the crystallite size, λ is the wavelength of the radiation (1.4518 A for Cu-Kα radiation), B is the corrected peak width at half-maximum intensity, and Θ is the peak position.

The specific surface area of the as-synthesized powder was measured using a MicroMeritics Gemini V Surface Area and Pore Size Analyser. By flowing nitrogen gas across the sample and observing a monomolecular layer adsorbed, a value (assuming spherical particles) can be assigned to the average particle size, using the equation

$$D = 6 / \rho A \qquad (5.2)$$

where d is the particle size, ρ is the theoretical density of the material, and A is the

specific surface area of the sample.

The size of the primary crystallites was also determined by HRTEM using a Phillips CM30 / Super Twin electron microscope.

5.2.2 Cell Fabrication and Testing

Requisite proportions of NiO and YSZ were mixed in ethanol and ball-milled for 24 h using zirconia milling media. The milled power was dried. Discs ~32 mm in diameter were uniaxially die-pressed. The disks were presintered at 1000 ^{o}C for 1 h. The discs were then coated with a slurry of anode interlayer of NiO + YSZ on one face and fired again at the same temperature to form a NiO + YSZ interlayer of about 20 μm thickness. The electrolyte was YSZ-SDC bilayer electrolyte thin film with a total thickness ~15 μm. The thin SDC layer as a part of the electrolyte served as a barrier to prevent chemical reaction between YSZ and strontium-doped lanthanum cobalt oxide ($La_{1-x}Sr_xCoO_{3-\delta}$(LSC), x = 0.3) used as cathode to form a barrier layer during high temperature firing.

The YSZ and SDC layers were applied upon the anode interlayer surface consecutively using, respectively, YSZ and SDC suspensions made from YSZ and SDC, dispersed ultrasonically in appropriate amounts of solvents. The surface of the anode disc was coated with the YSZ suspension. On top of the YSZ layer, a thin layer of SDC suspension was applied. Then the sample was fired in air at a temperature between 1400 ^{o}C and 1500 ^{o}C. The porous cathode interlayer was a composite of LSC and SDC, which was fired onto the bilayer electrolyte thin film at a temperature between 1200 ^{o}C and 1300 ^{o}C for 1 h.

5.3 Results and Discussion

5.3.1 Thermodynamic Analysis

According to the chemistry [9], for a stoichiometric redox reaction between a fuel and an oxidizer, the ratio of the net oxidizing valence of the metal nitrate to the net reducing valence of the fuel should be unity. In this work, carbon and hydrogen are considered as reducing elements with the corresponding valences 4+ and 1+, while oxygen is considered as an oxidizing element with a valence of 2-, and nitrogen is assumed to have a valence of zero. Cerium is considered as a reducing element with a valence of 3+ or 4+ in its nitrate and oxide, respectively. Samarium has a 3+ reducing valence. Using the valences of individual elements, total oxidizing valence (for example) of 0.8 $Ce(NO_3)_3$* $6H_2O$) + 0.2 $Sm(NO_3)_3$*$6H_2O$ works out to be 15+, while total reducing valance of DGA ($C_6H_{12}O_7$) is 22+. Therefore, the ideal stoichiometric ratio of DGA-to-nitrate needed to obtain $Ce_{O.8}Sm_{0.2}O_2$ is 22:15. Since very high flame temperatures, found with stoichiometric and fuel-rich precursor solutions, can affect the power characteristics adversely [10], (resulting in increased crystallite size, premature local partial sintering among primary active particles produced during combustion thereby reducing the final surface area, and similar effects) only fuel-deficient precursor solutions are used here. An example of calculations for determining fuel-to-nitrate ratio using elemental valences is presented in the Appendix.

To evaluate the effect of fuel-to-oxidant ratio on the final product properties, DGA-to-nitrate ratio was varied from 0.35 to 1. To observe the effect on adiabatic flame temperature with DGA-to-nitrate molar ratio, adiabatic flame temperatures were calculated for the ratio varying from 0.35 to 1. The combustion reactions can be

calculated for the ratio varying from 0.35 to 1. The combustion reactions can be presented as follows:

$0.35\ C_6H_{12}O_7 + (0.8\ Ce(NO_3)_3{*}6H_2O + 0.2\ Sm(NO_3)_3{*}6H_2O) \rightarrow$

$Ce_{0.8}Sm_{0.2}O_2 + 2.1\ CO_2(g) + 8.1\ H_2O\ (g) + 1.575\ O_2(g) + 1.5N_2(g)$ (5.3)

$\Delta H^0 = -91.21$ kcal

$0.55\ C_6H_{12}O_7 + (0.8\ Ce(NO_3)_3{*}6H_2O + 0.2\ Sm(NO_3)_3{*}6H_2O) \rightarrow$

$Ce_{0.8}Sm_{0.2}O_2 + 3.3\ CO_2(g) + 9.3\ H_2O\ (g) + 0.475\ O_2(g) + 1.5N_2(g)$ (5.4)

$\Delta H^0 = -213.141$ kcal

$0.7\ C_6H_{12}O_7 + (0.8\ Ce(NO_3)_3{*}6H_2O + 0.2\ Sm(NO_3)_3{*}6H_2O) + 0.35\ O_2(g) \rightarrow$

$Ce_{0.8}Sm_{0.2}O_2 + 4.2\ CO_2(g) + 10.2\ H_2O\ (g) + 1.5N_2(g)$ (5.5)

$\Delta H^0 = -304.58$ kcal

$0.85\ C_6H_{12}O_7 + (0.8\ Ce(NO_3)_3{*}6H_2O + 0.2 Sm(NO_3)_3{*}6H_2O) + 1.175\ O_2(g) \rightarrow$

$Ce_{0.8}Sm_{0.2}O_2 + 5.1\ CO_2(g) + 11.1\ H_2O\ (g) + 1.5N_2(g)$ (5.6)

$\Delta H^0 = -396.036$ kcal

$C_6H_{12}O_7 + (0.8\ Ce(NO_3)_3{*}6H_2O + 0.2\ Sm(NO_3)_3{*}6H_2O) + 2\ O_2(g) \rightarrow$

$Ce_{0.8}Sm_{0.2}O_2 + 6\ CO_2(g) + 12\ H_2O(g) + 1.5N_2(g)$ (5.7)

$\Delta H^0 = -487.483$ kcal

Available thermodynamic data in literature [11, 12] for various reactants and products are presented in Table 5.1. It is known that the enthalpy of combustion can be expressed as:

$$(\Sigma n\Delta H^0_f)_{\text{products}} - (\Sigma n\Delta H^0_f)_{\text{reactants}} = \int_{298}^{T} (\Sigma n C_p)_{\text{products}} dT \quad (5.8)$$

where n is the molar number and T is the adiabatic flame temperature.

Then we can write a general equation for the reaction:

$$\Delta H = \int^{T} [14.73n_1 + n_2(10.34+0.00274\ T) + n_3(7.2+0.0036\ T) + n_4(5.92+0.00367\ T) + n_5(6.5+0.001\ T)\ ]\ dT \quad (5.9)$$

where:

$N_1 = Ce_{0.8}Sm_{0.2}O_2$
$N_2 = CO_2$
$N_3 = H_2O$
$N_4 = O_2$ and
$N_5 = N_2$

are the stoichiometric coefficients in the reaction

Using the thermodynamic data for the various reactants and products listed in Table 5.1, the theoretical flame temperatures can be calculated. The relation of theorical adiabatic flame temperatures as a function of DGA-to-nitrate molar ratio is plotted as Figure 5.2. As expected, it increases substantially with the amount of fuel used during the combustion.

The measured temperature and theoretical adiabatic flame temperatures are presented in Table 5.2. It is seen that the actual flame temperatures were much lower than the theoretically calculated values, likely due to radiation losses and heating of air above the reaction mixture.

Figure 5.3 shows the measured temperature change with reaction time. The temperature remained stable during the evaporation of water. When the solution becomes a gel, the temperature increases quickly and eventually, ignition occurs. The gel-like material in the beaker starts to oxidize and swells to a yellow, fluffy mass. A flame flash immediately precedes runaway oxidation, and it continues in a self-sustaining manner until most of the fuel is used up, and the remaining fuel is sufficiently dispersed within

product mass so that ignition ceases. After that, the remaining mass containing products, unburnt, highly dispersed fuel, and any trace unreacted materials begins to cool down; the maximum temperature reached depends significantly on the starting fuel content. Also, the vigor of the reaction is influenced by the starting fuel content; a precursor mixture with the ratio of fuel-to-nitrate 0.35 reacted over 4 to 6 minutes, while a precursor mixture with a ratio of 0.55 or above reacted instantaneously.

5.3.2 Particle Size Estimation

5.3.2.1 XRD Peak Broadening

Figure 5.4 shows the X-ray diffraction studies on the powders obtained by combustion synthesis of SDC. From the figure, we can see that a homogeneous powder of high crystallinity was formed. The phase content (crystallite size) of the as-synthesized powder was also strongly dependent on the fuel content of the precursor solutions. With the ratio change from 0.35 to 1.0, the X-ray diffraction peaks increase in height (intensity) and the peak width decreases, which indicate the occurrence of particle growth from 4 to 9 nm (larger particles in the product powder).

In order to determine the peak broadening attributable only to the particle size effect, a commercial $Sm_{0.15}Ce_{0.85}O_2$ powder was sintered at 1500° C for 5 h to obtain a strain-free, coarse-grained (a few microns in particulate diameter) sample. An XRD trace of the sample was obtained. The corrected half-peak width, $B = \sqrt{B_m^2 - B_s^2}$, for a given (h,k,l), here (1,1,1), can be calculated from the peak width of the as-synthesized powder samples, B_m, and the corresponding peak width of the standard sample, B_s. Thus, line broadening attributable to the instrument, as well as the presence of both $K\alpha_1$ and $K\alpha_2$,

could be corrected for. Figure 5.5 shows the variation in X-ray broadening of the (1,1,1) peak with the DGA-to-nitrate molar ratio. The corrected peak width was measured to be approximately 0.85°, 0.92° and 1.72° for the as-synthesized samples. Using Equation 5.1 the particle sizes were 9, 8, and 4 nanometers (see Table 5.3).

5.3.2.2 BET Measurement

An alternative confirmation of the particulate diameter of the powders is to use the specific surface area measured from the BET adsorption isotherm method. The specific surface area of the as-synthesized nanosize powders were 21, 31, and 59 m^2 /g. Assuming particles to be spherical in size for simplicity, the diameter of the particle can be estimated from Equation 5.2, where the density of cubic ceria, ρ, is 7.2 g/cm^3. The results are listed in Table 5.4. It is seen that the average particle size is larger than the values estimated from XRD peak broadening measurement. This is because the as-synthesized powder presented large aggregates with a foamy aspect, as can be observed in Figure 5.6. These aggregates were voluminous and easy to break into individual small particles (as shown in Figure 5.7).

5.3.2.3 TEM Measurement

The particle sizes shown in the micrographs were confirmed to be nanometers in diameter, using the lattice fringes found in the micrographs. Most of the particles occurred in clumps or aggregates, although a few isolated particles were found. Figure 5.8 shows an electron diffraction pattern of the sample powder. The continuous and diffuse rings indicate that crystals are randomly oriented and crystal size is much smaller

than the beam diameter. It is also seen that the XRD line broadening diameters are averages, as particles of 5 nm diameter and below are found in each batch (Figures 5.9, 5.10, and 5.11).

5.3.2.4 Solid Oxide Fuel Cells Performance Test

The as-synthesized SDC powder was used in solid oxide fuel cells as an oxygen ion conductor in a composite electrode (the other phase is Sr-doped $LaCoO_3$ (LSC)) and as the barrier layer electrolyte on the top of a YSZ layer. Figure 5.12 shows the single-cell performance with active cathode area of 2 cm^2. At 800 ^oC, the maximum power density in excess of 1.6 W/cm^2 can be obtained.

5.4. Summary

Synthesis of samarium-doped ceria with specific surface areas up to 61 cm^2/g was demonstrated by the combustion of metal nitrate salts with DGA fuel in a precursor solution. The as-synthesized powder showed high crystallinity as characterized by XRD. Using the thermodynamic analysis based on adiabatic flame temperature, the effect of the ratio between DGA-to-nitrate content on the powder area and crystallite size was studied. To obtain powder of desired size and phase content, the fuel content must be carefully controlled. Solid oxide fuel cells using as-synthesized SDC powder in composite electrodes and electrolytes show high performance, in excess of 1.6 W / cm^2.

5.5 References

1) R. E. Kirk, D. F. Othmer, Encyclopedia of Chemistry and Technology, 3rd ed., vol. 5, Wiley, New York, 1979, 315

2) Y. Jiang, S. V. Bhide, A. V. Virkar, J. Solid State Chemistry 157 (2001) 149-159

3) Y. C. Zhou, M. N. Rahman, J. Mater. Res. 8 (1993) 1680

4) P. Lin, I. Chen, J. Am. Ceram. Soc. 76 (1993) 1577

5) M. M. A. Sekar, S. S. Manoharan, K. C. Patil, J. Mater. Sci. Lett. 9 (1990) 1205.

6) S. Basu, P. Sujatha Devi, H.S. Maiti, J. Mater. Res. 19 (11) (2004)

7) S. Litzelman, R. A. DeSouza, B. Butz, H. L. Tuller, M. Martin, D. Gerthsen, J. Electroceram 22 (2009) 405-415.

8) H. Toraya, M. Yoshimura, S. Somiya, "Calibration curve for quantitative analysis of the monoclinic-tetragonal ZrO_2 system by X-ray diffraction," J. Am. Ceram. Soc. 67 (1984) C119-121.

9) S. R. Jain, K. C. Adiga, V. R. P. Verneker, Combus. Flame 40 (1987) 7

10) R. D. Purohit, B. P. Sharma, K. T. Pillai, A. K.Tyagi, Mater. Res. Bull. 36 (2001) 2711-2721

11) R. H. Perry, C. H. Chilton, Chemical Engineer's Handbook, 5th ed., McGraw-Hill, New York 1975.

12) J. A. Dean (ed.), Lange's Handbook of Chemistry, 12th ed., McGraw-Hill, New York 1979.

Table 5.1. Relevant thermodynamic data

Compound	ΔH^o (kcal / mol)	C_p (cal / mol K)
$Ce(NO_3)_3*6H_2O$ (c)	-729.14	-
$Sm(NO_3)_3*6H_2O$ (c)	-730.4	-
$C_6H_{12}O_7$ (c)	-301.435	-
$Sm_{0.2}Ce_{0.8}O_2$ (c)	-260.2	14.73
O_2 (g)	0	5.92+0.00367T
H_2O (g)	-57.796	7.2+0.0036T
CO_2 (g)	-94.051	10.034+0.00274T
N_2 (g)	0	6.5+0.001T

Table 5.2. Adiabatic flame temperatures and measured maximum temperatures at various fuel-to-nitrate molar ratios

Fuel-to-nitrate molar ratio	Adiabatic Flame Temperature (^{o}C)	Measured maximum Temperature (^{o}C)
0.35	921	110
0.55	1460	113
0.70	1728	102
0.85	1907	105
1.0	2045	113

Table 5.3. Average particle size calculated from peak broadening

Fuel-to-nitrate ratio	Average particle size, nm
0.35	4.5
0.70	8.4
1.0	9.0

Table 5.4. Surface areas of as-synthesized powder and average particle size

Fuel-to-nitrate ratio	Surface area, m^2/g	Average particle size, nm
0.35	61.72	13.5
0.70	55.54	15.0
1.0	26.39	31.6

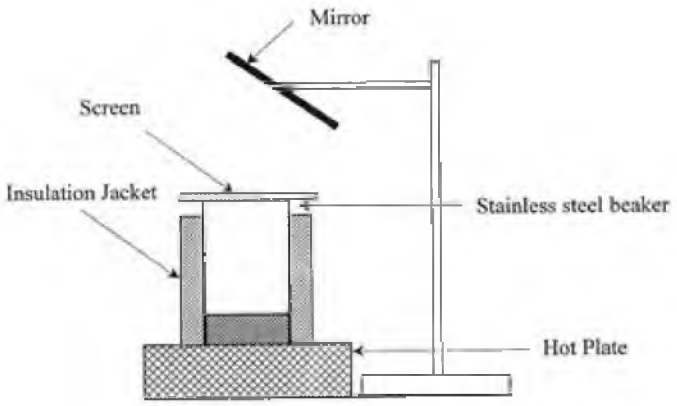

Figure 5.1: Experimental set-up for combustion synthesis of SDC

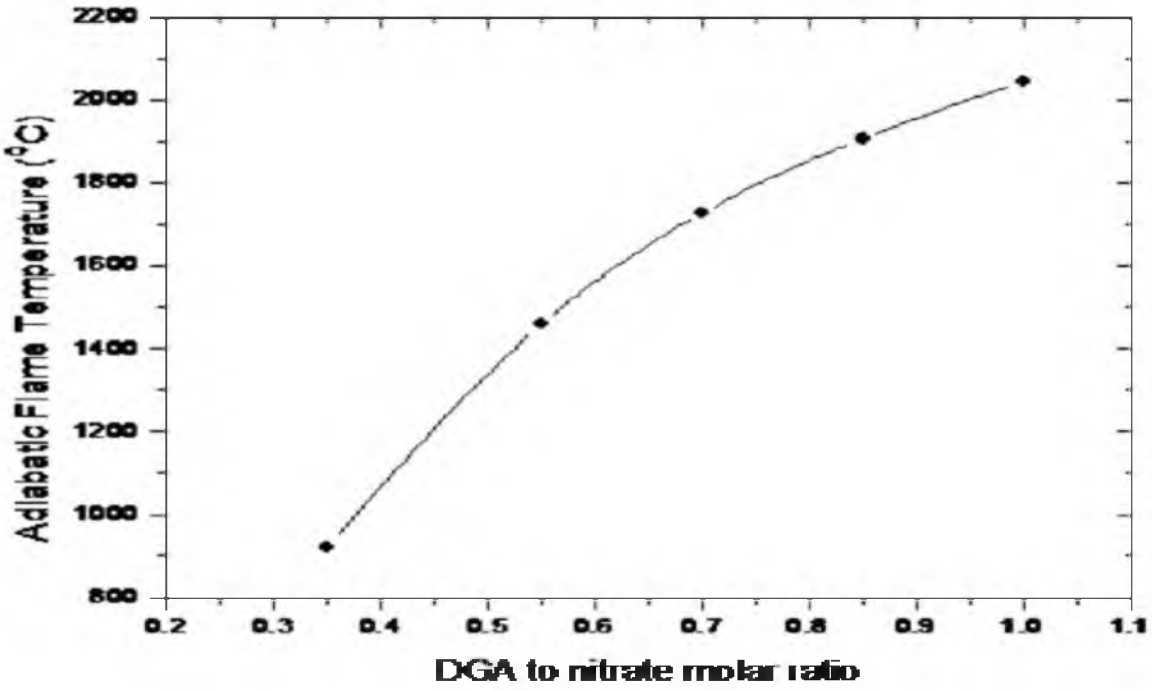

Figure 5.2 The calculated adiabatic flame temperature vs. the molar ratio of DGA to metal nitrate.

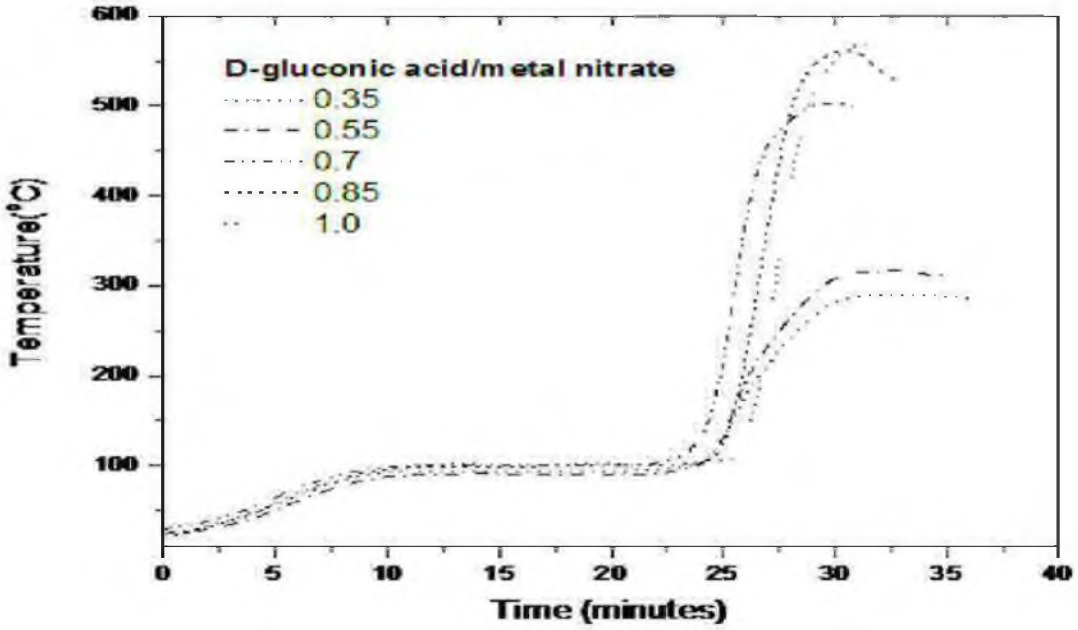

Figure 5.3 The temperature vs. time data during combustion synthesis

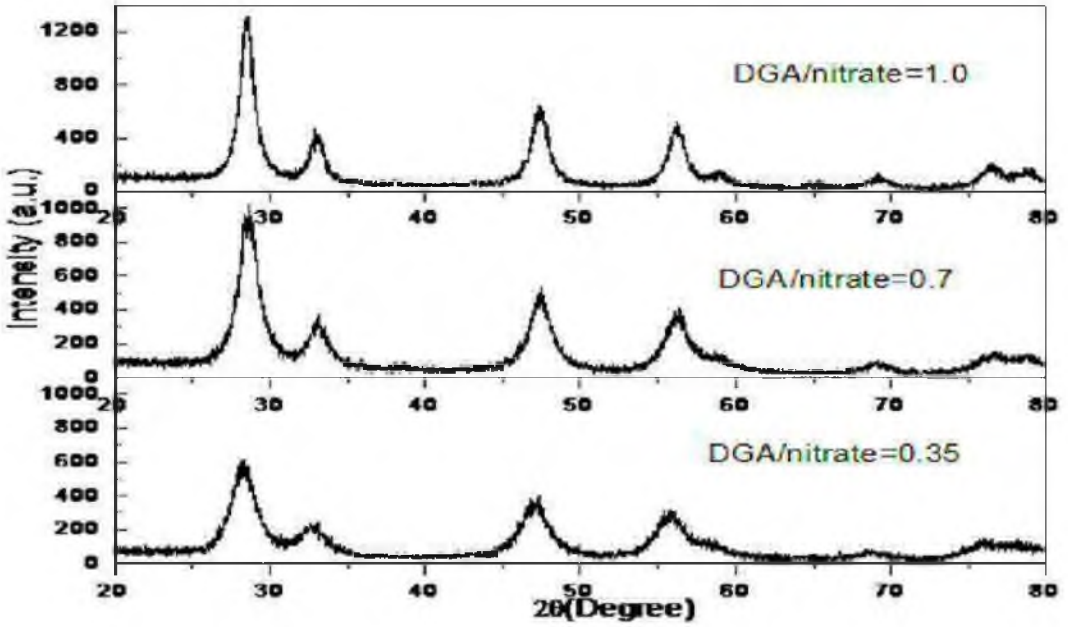

Figure 5.4 XRD spectra of SDC powders using various molar ratios of DGA to metal nitrate.

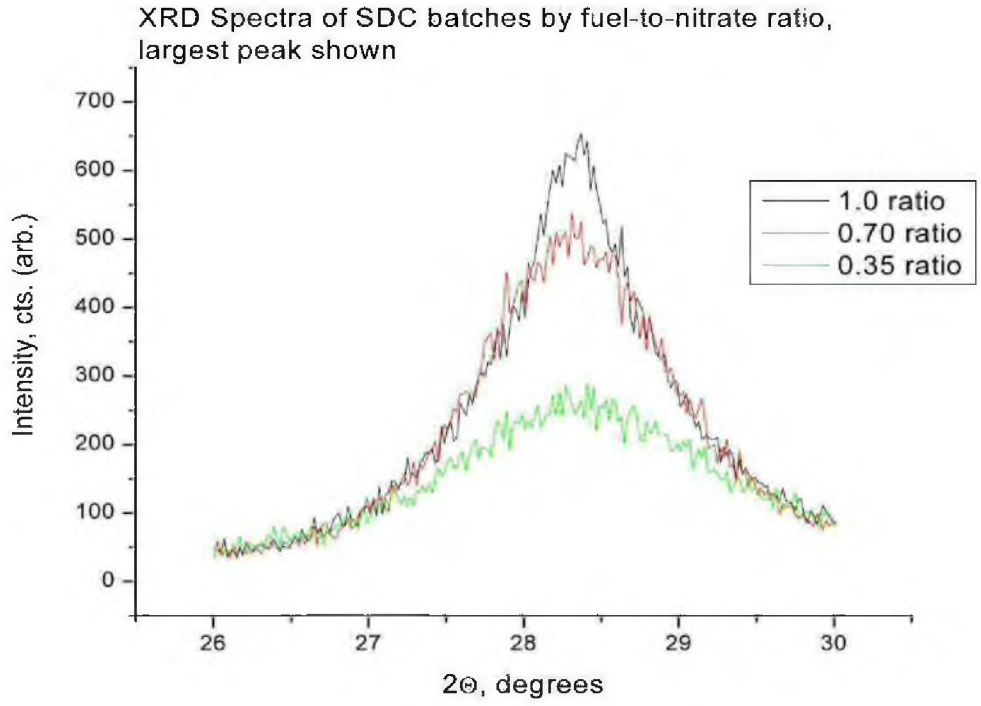

Figure 5.5 XRD line broadening for SDC powder obtained using various molar ratios of DGA to metal nitrate

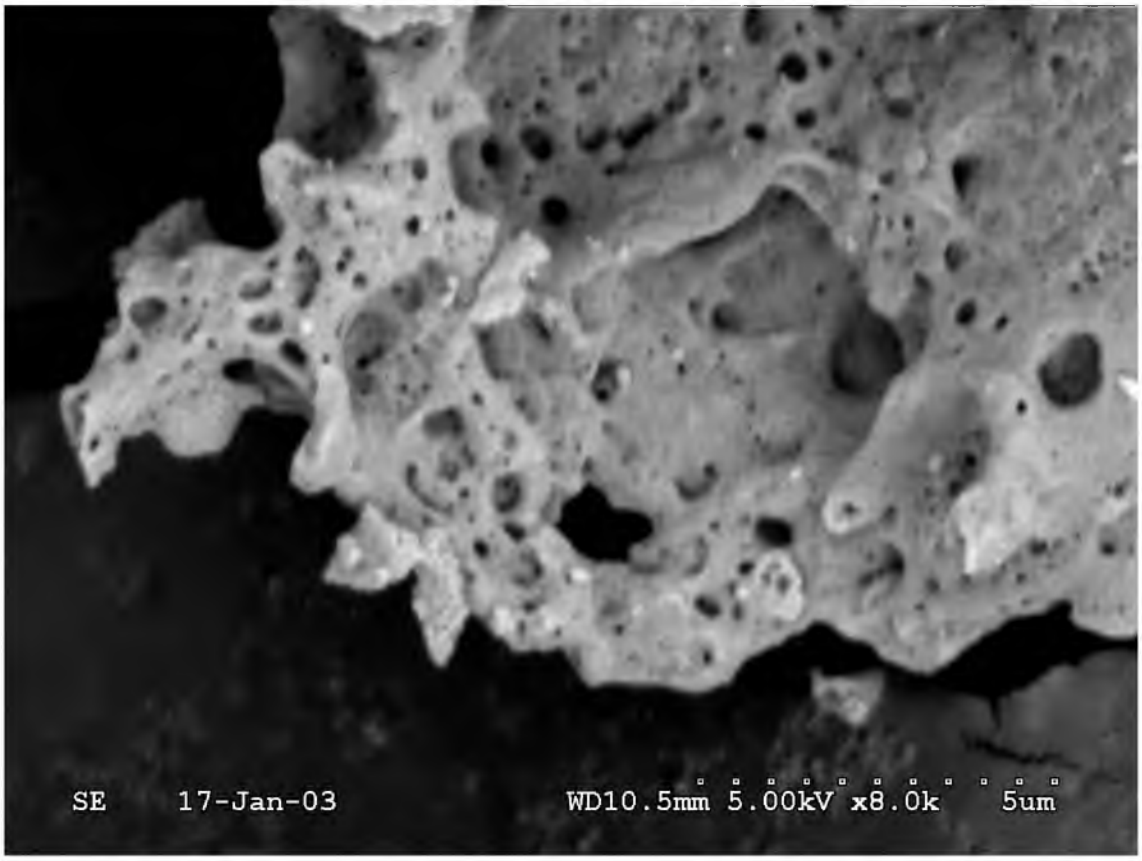

Figure 5.6 SEM micrograph showing the presence of large agglomerates in as-synthesized powders.

Figure 5.7: Electron diffraction pattern.

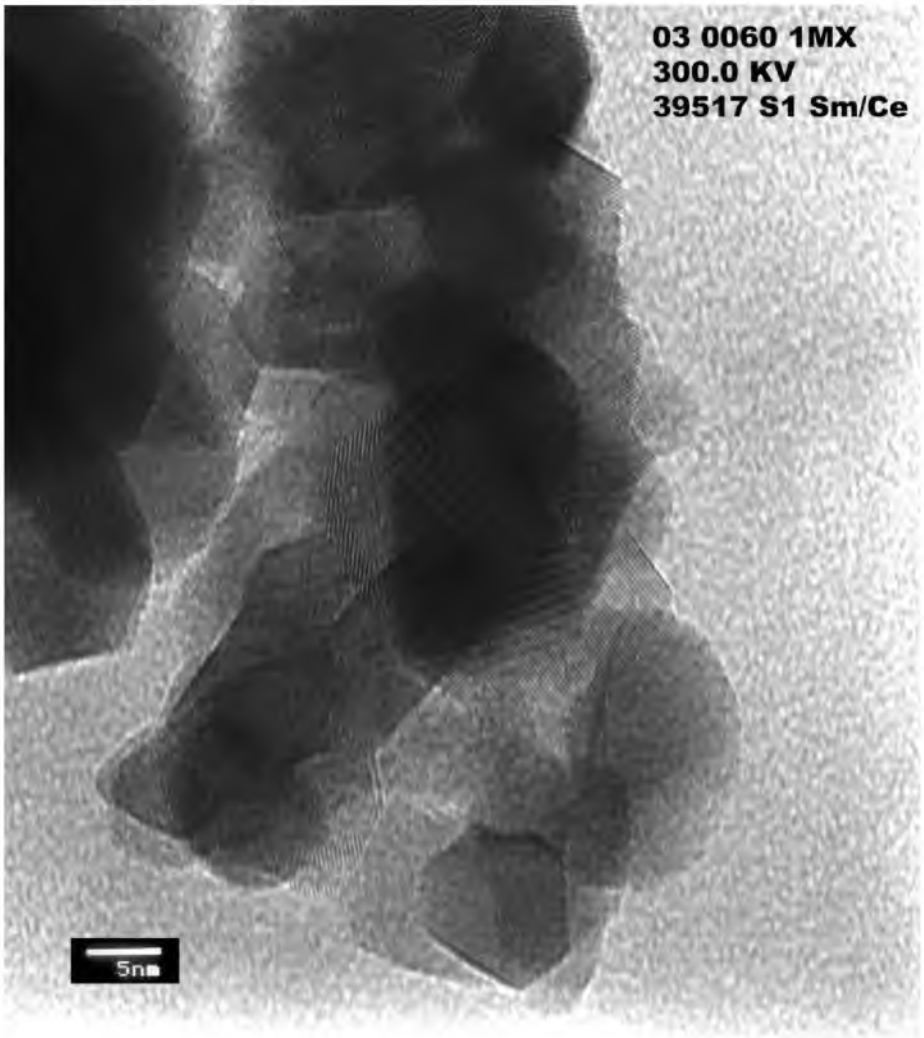

Figure 5.8 TEM (Transmission Electron Microscopy) micrographs (DGA/Nitrate = 0.35).

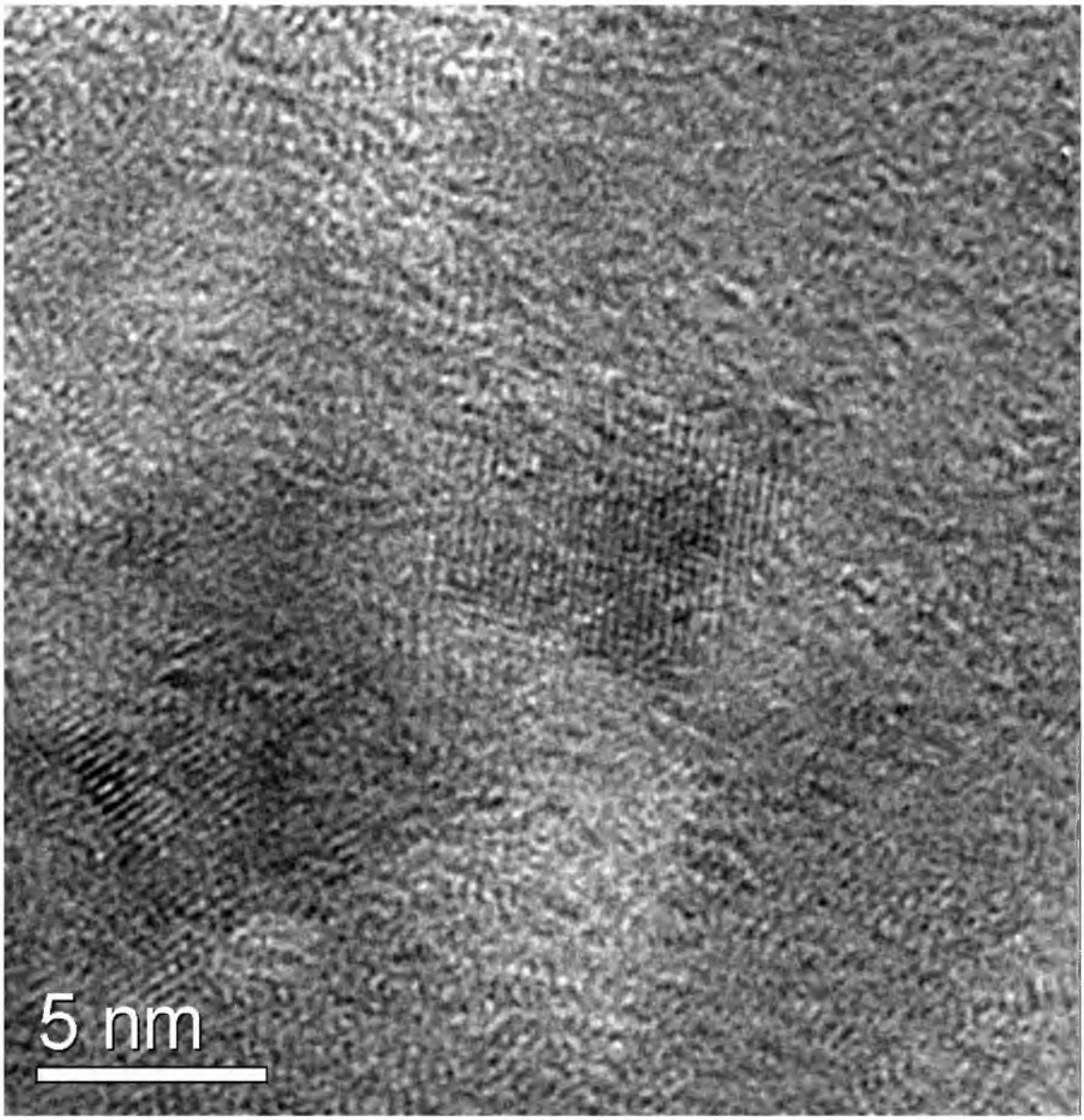

Figure 5.9. TEM micrograph of SDC powder cluster, fuel-to-nitrate ratio 1.0

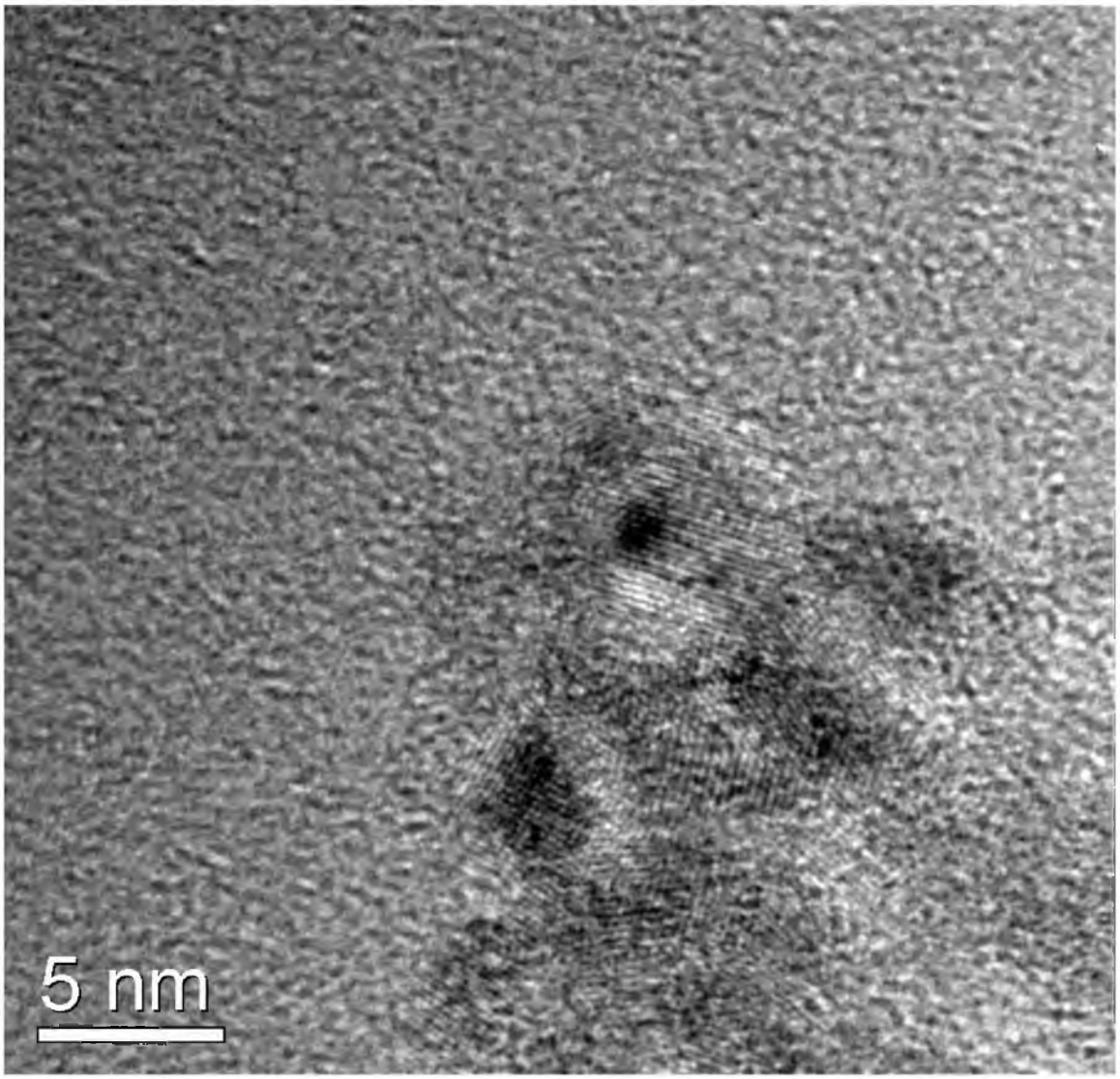

Figure 5.10. TEM micrograph of SDC powder cluster, fuel-to-nitrate ratio 0.70

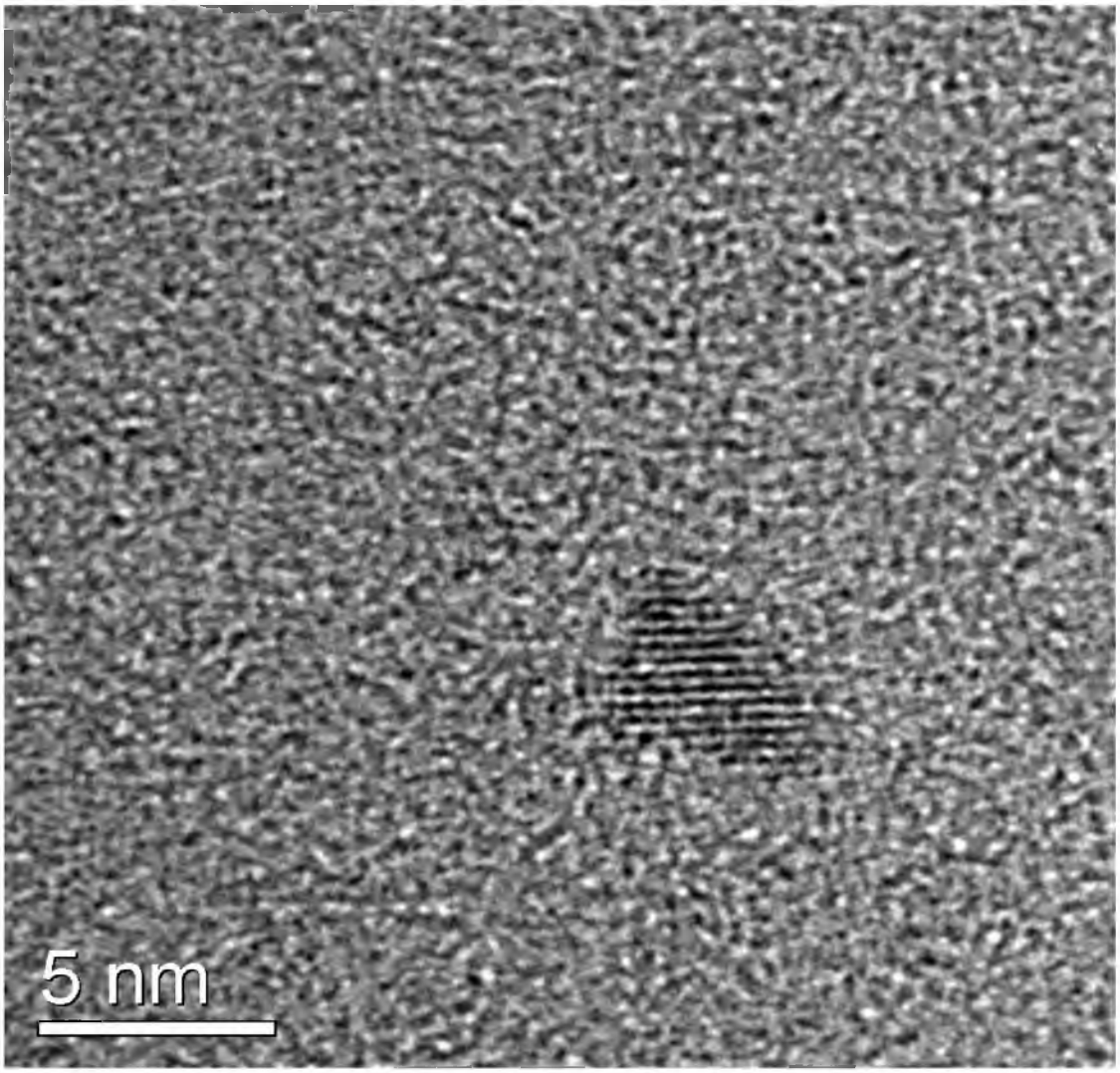

Figure 5.11. TEM micrograph of SDC particulate, fuel-to-nitrate ratio 0.35

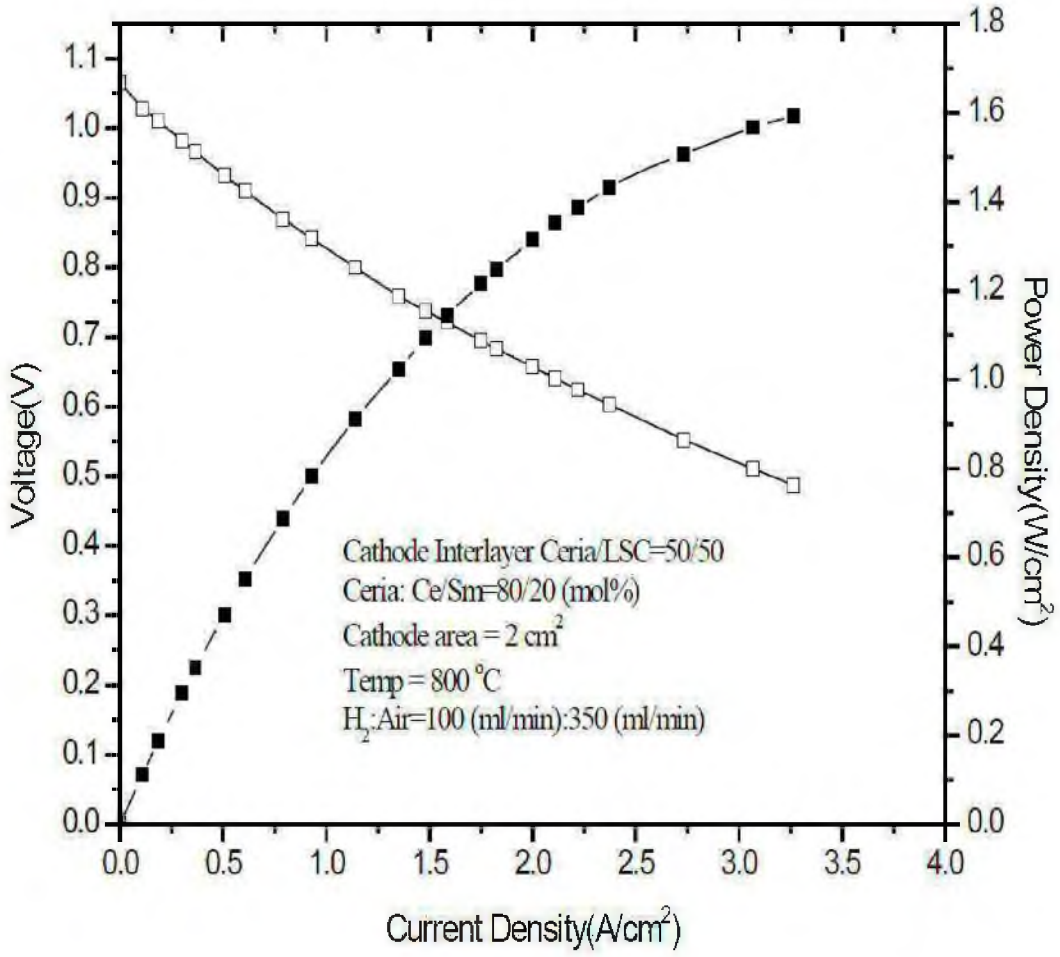

Figure 5.12: Button cell performance.

5.9 Appendix

Stoichiometric (balanced) equation for desired reaction:

$C_6H_{12}O_7 + (0.8\ Ce(NO_3)_3{*}6H_2O + 0.2\ Sm(NO_3)_3{*}6H_2O) + 2\ O_2(g) \rightarrow$
$Sm_{0.2}Ce_{0.8}O_2 + 6\ CO_2\ (g) + 12\ H_2O(g) + 1.5N_2\ (g) \quad \Delta H^o = -487.483$ kcal

To begin, assign values to the reactants by formula, using oxidizing and reducing values to determine the fuel-to-oxidizer (here, fuel-to-nitrate) ratio.

Carbon and hydrogen are considered as reducing elements with the corresponding valences +4 and +1, while oxygen is considered as an oxidizing element with a valence of -2, and nitrogen is assumed to have a valence of zero. Cerium is considered as a reducing element with a valence of +3 or +4 in its nitrate and oxide, respectively. Samarium has a +3 reducing valence.

Here, the fuel DGA (formula $C_6H_{12}O_7$) has the value 22 (carbon 4 x 6 = 24, hydrogen 1 x 12 = 12, oxygen -2 x 7 = -14, 24 + 12 - 14 = 22)

The reactants samarium nitrate and cerium nitrate generate 15 (cerium nitrate: $Ce(NO_3)_3$, Ce 3 x 0.8 = 2.4, $(NO_3)_3$ = -2 x 3 x 3 = -18; samarium nitrate $Sm(NO_3)_3$, Sm 3 x 0.2 = 0.6, $(NO_3)_3$ = -18).

Overall, the metal nitrates contribute 3 from metals (2.4 from Ce and 0.6 from Sm) and -18 from nitrate, so they contribute -15 combined and the ratio (using absolute values) is 22:15 (stoichiometric ratio is 22:15 for this reaction, so use 1.0 fuel-to-nitrate ratio or less when making nanosized powders).

[Water of hydration does not participate, $(NO_3)_3$ from reactants totals one mole (0.8 + 0.2 in balanced equation). Oxygen from atm. is used to oxidize carbon to CO_2.]

CHAPTER 6

SUMMARY AND CONCLUSIONS

The use of porous samples facilitates the measurement of thermodynamically equilibrated properties for use in design of electrochemical devices. The use of porous samples allows better capture of physical and transport properties that may escape casual or even detailed observation of dense, nonequilibrated samples. Porous samples equilibrate orders of magnitude faster than dense samples, which allows detection of material disadvantages that develop slowly (due to slower kinetics of dense samples) within a reasonable period of time. Finally, particle size can be controlled and reduced to nanometer scale during combustion synthesis by minimizing the excess fuel content of the starting mixture.

6.1 Samarium-doped Ceria

Using porous samples, it was shown that the electrolytic domain of SDC at 400° C and above is narrower than previously thought. The experimental work demonstrated that porous samples equilibrated faster than dense ones, were readily correctable using geometric factors to obtain accurate values, and allowed better design of devices rather than using property values gathered under unequilibrated or metastable conditions. The method used is applicable to other materials, although considerations of mechanical strength apply.

6.2 Strontium Iron Molybdenum Oxide (1)

Strontium Iron Molybdenum Oxide is not stable in the presence of liquid water, which is a grave shortcoming for an electrode in a solid oxide fuel cell. The likely presence of liquid water in startup and shutdown conditions, along with demonstrated

inability to regenerate SFMO under typical conditions of solid oxide fuel cell operation, preclude its use as an electrode in SOFC service without significant modifications, yet to be determined. The use of porous samples allowed detection of SFMO instability to liquid water in a short time of experiment, and difficulties in obtaining valid data in humid atmospheres underscored the instability problem.

6.3 Strontium Iron Molybdenum Oxide (2)

It was further found using XRD and EIS that SFMO is unstable even in dry atmospheres; when an electrolyte compound such as SDC is transporting oxygen ions to an SFMO electrode, the hydrogen dissociating on the SFMO surface will combine with the transported oxygen ions and form water as usual, which will not immediately diffuse away. While the produced water sits on the SFMO surface, it will attack and degrade the SFMO in place, resulting in decay, decay products, and eventually mechanical cracking and failure. Porous samples demonstrated this failure mode conclusively, as decay products built up in pores and fissures, eventually cracking the SFMO electrode along with the SDC electrolyte it was bound to as a surface layer.

6.4 Nanosized SDC Particles by Combustion Synthesis

The greater surface area of nanosized particles results in improved catalytic properties, faster transport properties, and smaller grain sizes, improving electrochemical properties as well. It was seen in the experimental work that the ratio of fuel to oxidizer in combustion synthesis is a critical factor in producing nanosized particles. Varying the fuel-to-oxidizer ratio below stoichiometric requirements results in smaller particles,

eventually creating nanosized particles of SDC. These were confirmed with XRD peak broadening, BET surface measurement, and TEM micrographs. It is expected that the method is applicable to any materials created using the combustion synthesis technique, although exact sizes of particles obtainable may vary due to other factors.

6.5 Future Work

There is little further work to recommend for SFMO, unless a way to stabilize it against water attack can be found. Since such a method would almost certainly involve isolating it from any moist or hydrogen-bearing atmosphere, it would no longer be able to function as an SOFC component. Therefore, any future role for SFMO will be found in other applications.

Samarium-doped ceria will require an electron-blocking layer to perform successfully as an SOFC electrolyte. YSZ would be a successful material to use in such a layer. If the electrolytic domain of SDC could be improved further to lower ohmic and polarization losses, the performance of SOFCs based on SDC / YSZ electrolytes could be improved. Co-doping SDC with rhenium, rhodium, and praseodymium did not improve the electrolytic domain of SDC in concentrations up to 15% (unpublished research from this laboratory), and concentrations above about 15% become mechanically weak and brittle when sintered. Other elements might be investigated to determine if this approach might yet succeed.